Characterization and simulation of electron/ion beam damage on soft materials in

FIB-SEM microscopes

By

Weiwei Zhang, M.Eng.

A Thesis

Submitted to the School of Graduate Studies

in Partial Fulfillment of the Requirements

for the Degree of

Master of Applied Science

McMaster University

i

MASTER OF APPLIED SCIENCE (2019) McMaster University

(Material Science and Engineering) Hamilton, Ontario

TITLE: Characterization and simulation of beam damage on soft materials in FIB-SEM system

AUTHOR: Weiwei Zhang, M.Eng. (University of Toronto)

SUPERVISOR: Professor Nabil D. Bassim

Lay abstract

Focused Ion Beam – Scanning Electron Microscopy (FIB-SEM) is a powerful tool for versatile cutting-edge materials characterization and has become more and more popular in recent years. However, the beam damage caused by these microscopes inhibits the further application of this technique, particularly for soft materials. Although researchers have developed some common methods to mitigate the damage, the understanding of underlying physical mechanisms of damage remains elusive. Here, we explored the relationship between the beam parameters and the degree of beam damage with the assistance of advanced characterization techniques. We also build an efficient heat transfer model to simulate the heating event in the system. Together, these results contribute to the fundamental understanding of beam damage mechanisms and pave the way to more state-of-art scientific research for the FIB-SEM system.

Abstract

The versatility and effectiveness of focused ion beam – scanning electron microscopy (FIB-SEM) instrumentation has advanced the field of electron microscopy, with such applications as high precision ultrathin site-specific TEM sample preparation, direct-writing lithography in semiconductor field, and FIB tomography for complex biological structures. However, the beam damage, including the beam induced heating, knock-on damage, and radiolysis damage from electron beam fundamentally alters the chemistry and bonding in sample materials. Although experience-based strategies, such as lowering the beam voltage and current or optimized milling strategies, have been developed to mitigate the damage, the lack of fundamental understanding of the underlying damage mechanisms inhibit the development of FIB-SEM strategies for imaging/milling new material systems. Previous work has shown that the main damage mechanisms for soft materials system are beam heating and electron radiolysis damage. In this research, I study the electron beam damage on the EMbed 812 epoxy resin in a systematic way by studying the relationship of the degree of damage and the common beam parameters, including beam voltage, current, and total irradiated electron dose. All the damaged samples were characterized by scanning transmission X-ray microscopy (STXM) which is a unique and suitable tool for this research. Our results show that the electron damage is a main cause for the chemical alteration in a plasma-FIB lift-out resin sample. Since there is no direct way to assess the beam induced heating problem during the milling process, we developed an effective heat transfer model by COMSOL for predicting the temperature rise during the FIB milling process. In this thesis, I included a detailed study by FIB-SEM, STXM, simulation work of polyvinylidene fluoride (PVDF), poly(methyl methacrylate) (PMMA) and the Embed812 epoxy resin.

Acknowledgement

First of all, I want to express my great gratitude to my supervisor, Professor Nabil Bassim. Though the way of scientific research is full of challenging and unknown difficulties, his patience, guidance, the trust in my ability make me strong enough to overcome the obstacles through my research life as a master student. Although I failed several times at the beginning of this research to find out the right way, he kindly encouraged and discussed with me about the possible solutions rather than blaming me for the naive thoughts and trials. I remember clearly that when all the common available characterization tools, FTIR, XPS, and Raman failed to tell the story at the near end of 2017, he patiently encouraged me not to be so frustrated and walked through all the results and find out the reasons with me together. I also greatly appreciate his trust over me to overcome these problems and we finally made it! His patience, guidance, and trust make me achieve what we got today. Once again, I sincerely appreciate professor Bassim for all his support for my two-research life at McMaster.

Second, thanks must be given to Dr. Lis G.A. Melo and professor Adam Hitchcock. Their assistance on STXM experiments and data analysis is the biggest breakthrough of this work and helped make the work of this research publishable. They nicely helped me to interpret the story behind the spectral analysis change and I learned a lot during the discussion with them.

Third, I want to thank all the group members, like Peng Dong, Longxing Chi, Hesham El-Sherif, Yasamin Sartipi, Christopher Schankula, Khatereh Maleki, Connor Wong, Sam Norris, and Ryan Young for their great support and advice. I really appreciate the time we spend together at Phoenix and curling time. I also want to thank Dr. Jian Wang at CLS, Dr. Shaobo Cheng, Dr. Hui Yuan, Dr. Chris Butcher, and the other technicians at CCEM, for their help and professional suggestion for this research work.

Besides, I also want to thank my great friends and colleagues: Ri Chen, Yi Feng, Hao Lin, Baoqin Deng, Shusheng Li, Hanshuo Liu, Shenglong Liang, Yuanzhe Chen, Guangqing Tai, Taoran Wang, Ghazal Seyed Mousavi, and Mohammad Hossein Ghoncheh etc. It is your companion around me make my life vivid and fun. Thank you all for your encouragement and supporting in life outside of research.

最后我想感激我的父母和不在身边的好友，非常感谢你们一直以来的支持与理解。"慈母手中线，游子身上衣"。虽然远在异国他乡，但是父母给予的来自家的关怀与我常伴，是我坚持前进的导航灯和予我休憩的港湾。非常感谢父母这么些年来的鼓励与理解，谅儿行千里不能与二老常伴，你们身体健康心情开心是我最大的快乐。在此也非常感谢因地理之隔而远离的朋友：张津源，陈鹏，徐畅，伍垚，张凯宁，张择灏，谭佩等，虽然与你们分离，但你们在我受挫之时给予的关心与支持，促使着我努力前行，虽不能随时随地地谈天说地，但也愿你们的人生一路顺利，事业有成。

Table of Contents

List of figures

List of tables

Declaration of achievement

This thesis is written as a 'sandwich' style including one published paper on Micron journal, chapter 4, and one poster presented on 11th FIB-SEM workshop 2018. I declare the following contribution in this thesis:

Weiwei Zhang was the primary author of the published paper, chapter 4, content of poster, chapter 5, and the writing of this thesis.

Dr. Nabil Bassim was the supervisor in all projects related to this thesis. He provided ideas, useful discussion and suggestion, helping on revising on all manuscripts.

Dr. Lis G.A. Melo was the graduated Ph.D. in the department of chemistry. She helps conduct the STXM characterization work in chapter 4 and 5, and help with the data process and analysis.

Dr. Adam Hitchcock was the professor in the department of chemistry and professional in STXM study. He gave useful suggestions of the revision of the manuscripts in chapter 4 and 5.

Marcia West helped prepare all ultramicrotomed sample in this thesis.

The publication and poster included in this thesis are:

- Chapter 4: Zhang, W., Melo, L., Hitchcock, A., and Bassim, N. *Electron beam damage on epoxy resin film studied by scanning transmission X-ray spectromicroscopy, **Micron***, vol 120, May 2019.
- Chapter 5: Zhang, W., Melo, L., Hitchcock, A., and Bassim, N. (2018). *Untangling the electron beam damage from overall specimen damage in the FIB-SEM system*. Poster presented in 11th Annual FIB–SEM Workshop, McMaster University, Hamilton, Canada

Chapter 1 Introduction

This chapter gives a brief introduction of focused ion beam (FIB) technique, its applications in various research fields, and the importance of understanding and mitigating the beam damage in its application. After that, different types of beam damage are further introduced, and the different characterization techniques for evaluating the degree of damage are also discussed. At the end, the outline of the research goal and each chapter of this thesis are presented.

1.1 Development and application of focused ion beam technique

Developed from late 1970's, focused ion beam (FIB) microscopy has attracted more and more attention in the fields of semiconductors, failure analysis, and sample preparation for transmission electron microscopy (TEM).(Ali, Hung, & Yongqi, 2010; N. Bassim, Scott, & Giannuzzi, 2014; N. D. Bassim et al., 2012; Lucille A Giannuzzi, 2004) By focusing energetic ions on the sample surface, the ion-matter interaction can generate many signals as shown in the figure 1, such as secondary electrons, sputtered material, and secondary ions etc. Many analyses can thus be done by analyzing these secondary signals. For example, we can use He-ion based FIB for imaging by collecting the outcoming secondary electrons and ions, with superior results as compared to scanning electron microscopy (SEM) in the case of non-conducting samples due to diminished sensitivity to charging.(N. Bassim et al., 2014; Orloff, 1993) Besides, with the more advanced focusing lens techniques, the ion beam can therefore be further confined and reach the scale of nanometers and used for direct-write nanomachining. FIB is competitive with others lithography techniques, like photon and electron lithography.(Alves et al., 2004; Carbaugh, Wright, Parthiban, & Rahman, 2016; Oshima, Okubo, Oyama, Washio, & Tagawa, 2012) especially in a rapid prototyping, custom nanostructural environment. Compared with the other two, the FIB provides a more efficient and straightforward way through (maskless, resistless) direct-writing, more powerful output, and site-specific milling.(Utke, Hoffmann, & Melngailis, 2008) However, the energetic ions can easily result in unwanted damage on the sample and research finds that it is hard to mill sample at specific position without damaging it by the ion beam. By coupling with scanning electron microscope (SEM), FIB now can extend its applications to versatile research fields and it becomes widely-known as FIB-SEM system.(N. Bassim et al., 2014) As shown in figure 1.2, the

FIB-SEM system configuration usually has two columns with an angle of 54º between them.(Lucille A Giannuzzi, 2004) In most of the case, the vertical column is the SEM while the inclined one is the FIB. Due to the incorporation with SEM, the damage induced by the energetic ions can be reduced dramatically because it is no longer being used to image the sample but rather pattern/mill the sample. Since SEM can help locate the desired sites and image the sample during milling without causing noticeable damage on the sample, FIB-SEM becomes a powerful tool for the ultra-thin site-specific sample preparation of transmission electron microscopy. Besides, the FIB-SEM system also provides a straightforward method for 3D tomography by using the serial sectioning method, which also known as FIB tomography. The basic idea is to image the cross-section face with SEM and then mill away a slice around 50 – 100 nm, then repeat the process until it reaches the desired distance, often with hundreds or thousands of images. After acquisition, the stack of images is processed using software for the 3D reconstruction, including alignment, cropping, segmentation and analysis. Compared with X-ray and TEM tomography, the FIB tomography is considered as a destructive way to reveal the 3D structure, because the sample is gone after the data collection process and the process is not repeatable. However, as shown in the figure 1.3, the FIB tomography is the key element for covering the bridging the length scales between X-ray tomography and transmission electron tomography in voxel dimension from 10 nm to 1µm.(Burnett et al., 2016) Besides, the sample preparation requirement for FIB tomography is much easier compared with the TEM tomography, which needs very thin samples, is very site specific and employs a rotational geometry subject to "missing wedge" artifacts. Therefore, FIB tomography has become more and more popular within the structure study field of corrosion, advanced cement, and even the biological materials etc (Bakhsh et al., 2015; Kizilyaprak, Daraspe, & Humbel, 2014; Titze & Genoud, 2016). Due to the increase attention on the application of FIB-SEM techniques, many related issues have also become more obvious and some of them are inhibiting the further development and applications in the new field.(Bakhsh, 2015; Bakhsh et al., 2015; Zeng, Inkson, Rainforth, & Stewart, 2007) One of the most typical problems of FIB milling is the curtaining, which is an artifact caused by the uneven distribution of the ion beam, different sample hardness distribution, and the preferred orientation of the sample during milling.(Denisyuk et al., 2017; Edwards et al., 2007; Santoro, Neumann, Panaitov, & Offenhausser, 2014; Schwarz, Kempshall, Giannuzzi, & McCartney, 2003) Methods, including lowering the beam power, rocking the stage in order to prevent beam channeling effects during milling, and novel protective

capping layers on top of the material of interest have been developed to mitigate the curtaining effect(Denisyuk et al., 2017; Santoro et al., 2014; Schwarz et al., 2003). However, when it comes to soft materials, like polymers or biological samples, the damage caused by the ion and electron beam become more obvious than the inorganic materials, since soft materials are usually more sensitive to the beam damage because of their lower thermal conductivity and weak bonding of the molecular structure.(Denisyuk et al., 2017; Edwards et al., 2007)
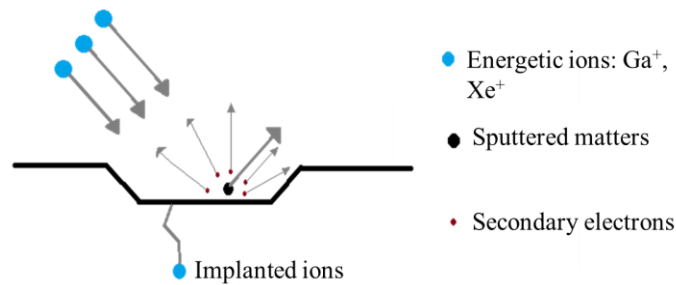
Figure 1.1 Schematic drawing of ion – matter interaction of FIB. Various signals including the backscattered ions, secondary electrons, sputtered materials, and X-ray.
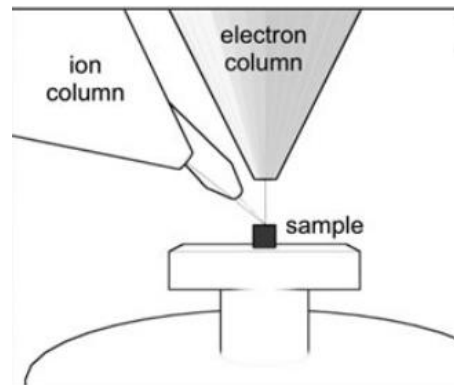
Figure 1.2 Schematic drawing of the FIB-SEM system configuration. (Lucille A Giannuzzi, 2004) The ion column is in a 54° with the electron column.
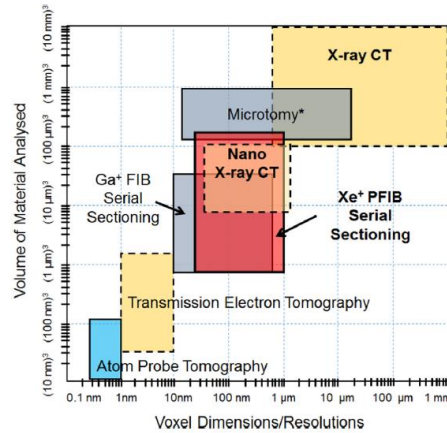
Figure 1.3 3D imaging methods for materials science.(Burnett et al., 2016) The FIB tomography technique fills in the gap between the X-ray tomography and TEM tomography.

1.2 Types of beam damage

Researchers have found that the damages caused by the FIB-SEM system can be mainly categorized into 3 types: ion beam induced heating damage, knock-on damage, and electron induced radiolysis damage.(Bailey, Geurts, Stokes, de Jong, & Barber, 2013; N. D. Bassim et al., 2012; Schmied et al., 2014) In different materials systems, the extent of each damage mechanism is also different. The poor thermal conductivity and weak bonding make soft materials more sensitive to the heating and radiolysis damage issues.

1.2.1 Ion beam induced heating damage

The beam induced heating can be attributed to the phonons generated from the cascade events of the injected energetic ions within the samples.(N. D. Bassim et al., 2012; Kim, Park, Balsara, Liu, & Minor, 2011; Rykaczewski et al., 2016; Schmied et al., 2014) The speed of local temperature rise depends on several instrumental factors, including beam voltage, beam current, and the scanning and milling strategy, coupled with the thermal properties of the sample. The poorer thermal conductivity of soft materials, for example PVDF has a thermal conductivity of 0.25 W/m K and melting point of 167°C(Zhou, Zuo, & Ren, 2012), makes them susceptible to damage by heating. The distribution of the induced phonon can be simulated by the Monte Carlo simulation

software named Stopping and Range of Ions in Matters (SRIM). Researchers have tried to build the heating models to simulate the heating event of the FIB milling process and some of them estimated that the rapid local temperature rise could be high as thousands of degrees Kelvin, which is far beyond the decomposition temperature of all polymer and biological materials, resulting in severe heating damage events at the point of impact and even adjacent to the beam interaction volume.(Brostow, Gorman, & Olea-Mejia, 2007; Ishitani & Kaga, 1995; Rykaczewski et al., 2016; Schmied et al., 2014; Wolff et al., 2018) Additionally, the temperature rise due to the energetic ion beam can also lead to mechanical softening of the of the material, which, for example, results in the poor quality of a final lift-out TEM sample.(N. D. Bassim et al., 2012) To mitigate the beam heating damage, researchers have developed various methods, including the use of cryogenic stages, lowered beam currents and voltage, advanced beam scanning strategies, and designing copolymers with better thermal properties. The cryogenic stages can help reduce the heating by creating a relatively low starting temperature. The lower beam current and voltage is to reduce the actual heat deposited on the sample. The advanced scanning strategies can help the heat to dissipate more efficiently. However, the biggest challenge for the beam heating is the difficulty in assessing the beam damage directly. Typical understanding relies on a computational heat transfer model.

1.2.2 Knock-on damage

For crystalline materials, the cascade collision of the incoming energetic ions can physically dislocated atoms in the sample from their lattice sites and easily destroy the crystallinity, creating a highly-disordered to amorphous layer. This process is also known as amorphization, a common damage observed in FIB prepared crystal samples.(Ali et al., 2010; N. Bassim et al., 2014; Belianinov et al., 2017) Techniques to mitigate this kind of damage include lowering the final milling voltage and current, polishing by broad ion beam, and using different ion sources for the final milling step.(N. D. Bassim et al., 2012) As for soft materials, since most of them are semi-crystalline or totally amorphous, it is difficult to observe the direct damage evidence via high-resolution TEM or via diffraction methods. However, it has been reported that under the bombardment from the energetic ions, the backbones/sidechains and the function groups can be ruptured off from the main chain, which can be detected by secondary ion mass spectrometry (SIMS). (Briggs & Hearn, 1986)

1.2.3 Radiolysis damage

The electronic structure of soft materials can be altered by the ion/electron induced radiolysis damage which are often hard to observe directly during the milling process. Bonds can change, reorder or lose hydrogen under irradiation from charged particles. Although the change in the chemistry and nature of the bonding may not be visible during the imaging/milling process, the change may affect other properties of the materials, like causing the chain scission or cross-linking. This in turn could make the the sample more sensitive or resistive to ion milling thus raising the difficulty to achieve the high-quality sample due to the inhomogeneous sample properties. Bassim et. al. has reported that the radiolysis damage mainly comes from the irradiation of SEM during the sample preparation process and he showed that there is a significant change in the chemical spectrum between the polyacrylamide (PAAm) with and without the irradiation of electron beam.(N. D. Bassim et al., 2012) Other studies also revealed that the radiolysis damage from electron should not be negligible, especially for the soft materials like polymers and biomaterials.(Bailey et al., 2013; R. F. Egerton, Li, & Malac, 2004; Estivill, Audoit, Barnes, Grenier, & Blavette, 2016; Jiang, 2013; J. Wang, Button, West, & Hitchcock, 2009) It has also been reported that the radiolysis damage is correlated with the generation of secondary electrons. Since both ions and electrons are capable of generating secondary electrons, it is reasonable to believe that both beams can cause radiolysis damage in the soft materials.(de A. Melo et al., 2016)

1.3 Characterization methods for beam damage evaluation

In order to mitigate the damage, one should first be able to understand factors contribute to the damage and figure out the relationship among factors and the degree of damage on the sample. To assess the beam induced heating damage, one may need to equip the FIB-SEM with more advanced IR detector to measure the in-situ temperature rise during the milling process. Otherwise, it is hard to distinguish the heating damage from the milling damage based on the appearance of the final morphology of the sample. To assess the beam induced heating damage, researchers usually use the simulation to predict the possible temperature rise due to the injection of energetic ions and try to compare some indirect measurements to benchmark these simulations. Knock-on damage is also difficult to characterize due to the partial-to-full amorphous properties of the soft materials.

Therefore, the only type of damage that we can characterize using readily available techniques is radiolysis damage. To characterize the chemical change in the polymeric materials, four types of characterization techniques are commonly used: Fourier-transformed infrared spectroscopy (FTIR), X-ray photoelectron spectroscopy (XPS), electron energy loss spectroscopy (EELS), and scanning transmission X-ray spectromicroscopy (STXM) with near edge X-ray absorption fine structure (NEXAFS).

1.3.1 Fourier-transformed infrared spectroscopy (FTIR)

FTIR is the most commonly used characterization technique for organic materials. There are usually two types of FTIR techniques based on different geometries, transmission and reflection. In this thesis, Attenuated total reflection (ATR) FTIR was attempted to characterize the electron beam damage, because the reflective FTIR is more suitable for the characterization of damage layer on the sample surface. The basic working principle of this type of FTIR is briefly illustrated in the schematic diagram as shown in the figure 1.4 below. (Sun, Chen, Zhou, & He, 2006)
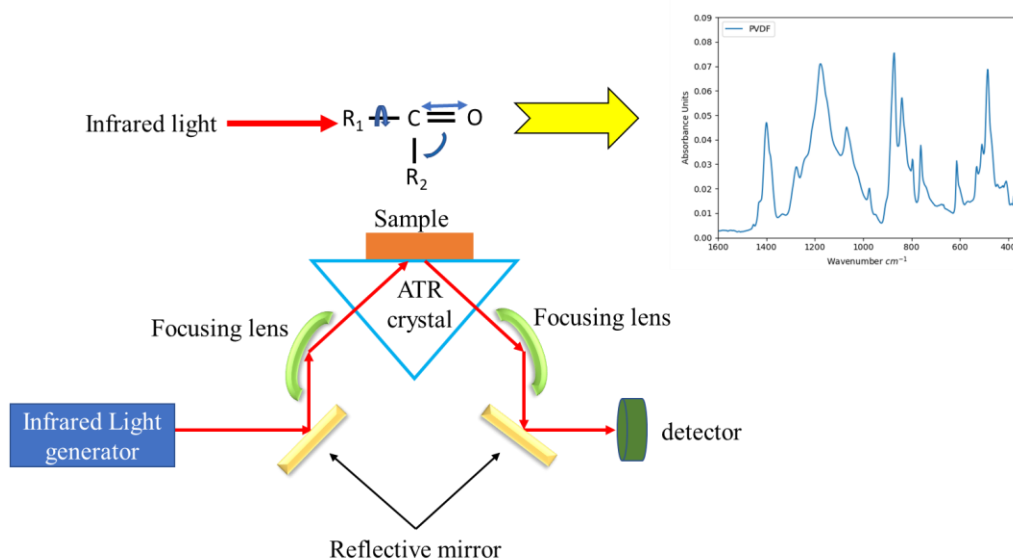
Figure 1.4 Schematic drawing of the instrumental setup and working principle of FTIR. The incoming IR light can interact with the vibration, rotation, and stretching of the organic molecules and be absorbed to form the spectrum.

To see whether the FTIR is the suitable tool for our experiment, we used SEM to irradiate the PVDF and resin sample using automated python-based scripting and characterized the polymers with our FTIR instrument. However, the interaction volume of infrared in the polymer, which is more than 10µm (Nagai, Matsunobe, & Imai, 2005), is larger than the interaction volume of the ion and electron in the polymer, which is around several hundred nanometers estimated by SRIM and CASINO. Besides, the lateral spot size of the ATR-FTIR is about 200µm for our instrument. Therefore, the damage zone is so small compared with the detected zone. Figure 1.5 (a) (b) show the FTIR spectrum comparison between the pristine and electron damaged PVDF and resin samples, respectively. Thus, FTIR is not a suitable tool for the purpose of this thesis to distinguish the chemical change due to the irradiation damage.
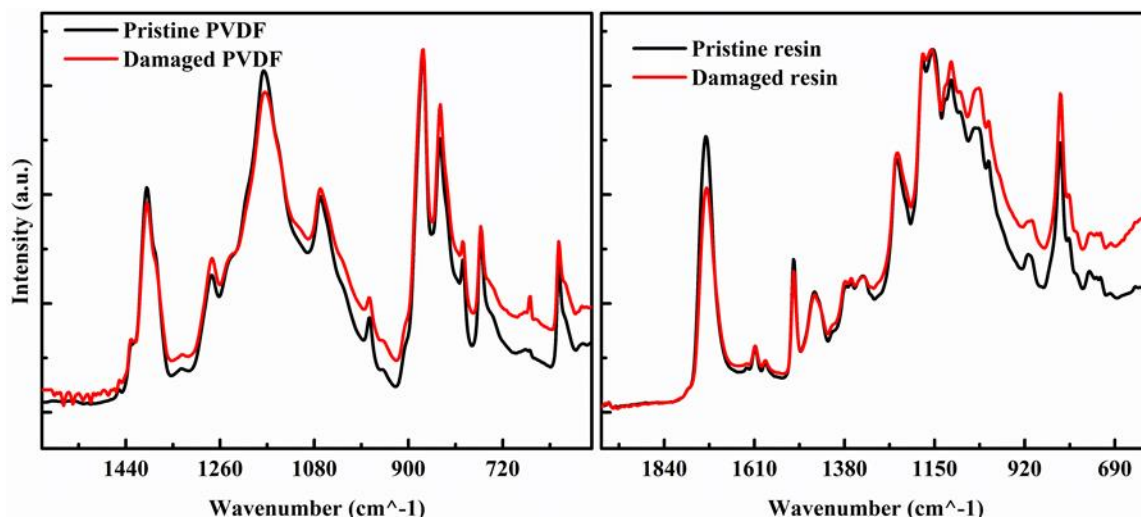
Figure 1.5 FTIR comparison results of pristine and damaged (a) PVDF and (b) resin sample.

1.3.2 X-ray photoelectron spectroscopy (XPS)

XPS is powerful tool for the characterization of surface chemistry. It uses X-rays to excite the photoelectron emission from a sample. By measuring the kinetic energy of the outcoming photoelectron, we can identify the elemental information, composition information, and even the valence state of the sample surface. XPS has been extensively used in many surface chemistry research fields, including novel energy materials, biomaterials, and advanced semi-conductor

materials.(Ektessabi & Sano, 2000; Kochumalayil, Meiser, Soldera, & Possart, 2009; Sato et al., 2003) We also tried to use the XPS to characterize the electron beam damage PVDF and resin sample in the research and the results are shown in figure 1.6 (a) and (b) for PVDF and resin respectively. Carefully inspecting the spectrum results, the damage due to the irradiation of electron beam can be found. The peak shifting and the missing peaks indicates that there are changes in the chemical composition and states of the samples after the irradiation electron beam. However, similar to the FTIR technique, the large spot size of the XPS makes the damage zone difficult to detect, leading to an unreliable quantitative analysis. Besides, few literature studies on the relevant materials makes the interpretation of the spectrum results very difficult and the analysis process requires the researchers to be experienced enough to distinguish whether the peak shift is due to the chemical states change or the generation of the new peaks in that range. Therefore, XPS is a suitable tool for proof-of-concept analysis but not an efficient tool for the further beam damage studies in the research of this thesis.
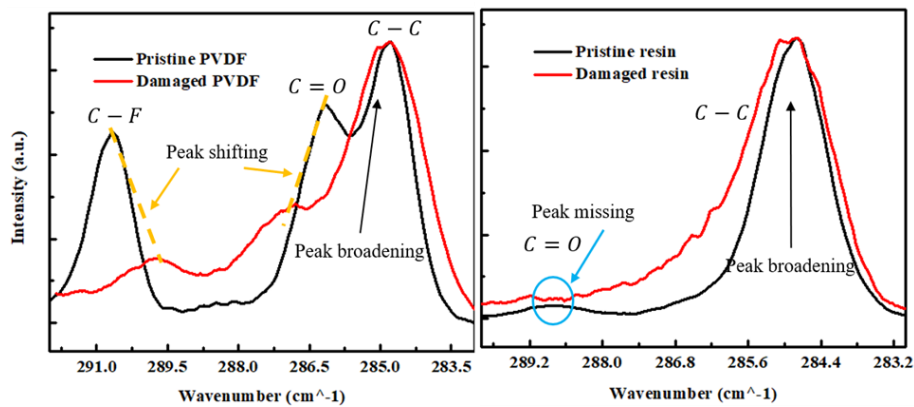
Figure 1.6 XPS comparison results of the pristine and damaged (a) PVDF and (b) epoxy resin. Obvious C-F and C=O peak shifts can be observed in PVDF and missing peak of C=O can be found in resin.

1.3.3 Scanning transmission electron microscopy – electron energy loss spectroscopy (STEM – EELS)

With the fast development of modern electron optics platform and cutting-edge detector, such as cryogenic stages and direct electron detectors, STEM-EELS has become more and more popular in many fields of research, including novel functional nanomaterials and nano-devices, structural biological study, and advanced study on multiferroic materials.(Ray F Egerton, 2011; X. Li, Sun, Shan, Chen, & Wei, 2018) The main working principle for EELS is shown in the figure 1.7 below. When the incoming electrons pass through the sample, the electron/matter interaction can result in elastic and inelastic scattering events, which can lead to the energy loss of the transmitted electrons. By detecting the energy loss, one can get various information about the materials, including but not limited to elemental identification, composition mapping, valance states analysis, and even the band gap measurement.. Researchers have also used EELS to study organic or polymer materials.(Laffont et al., 2004; Varlot, Martin, Gonbeau, & Quet, 1999; Varlot, Martin, & Quet, 2001; Vilar et al., 1987) However, since the beam voltage used for common TEM study is usually 80 ~ 200 keV, the high energy electron beam may cause damage during the characterization process. Besides, to acquire accurate EELS information about the C 1s structure for organic or polymer samples, the acquisition time may be high, which can result in severe damage from sputtering and heating.(R. Egerton, 2012; R. F. Egerton, 2013; R. F. Egerton et al., 2004; R. F. Egerton, McLeod, Wang, & Malac, 2010; R. F. Egerton & Rauf, 1999; R. F. Egerton, Wang, & Crozier, 2006; P. Li & Egerton, 2003) Therefore, STEM-EELS is also not the appropriate characterization tool for our study.
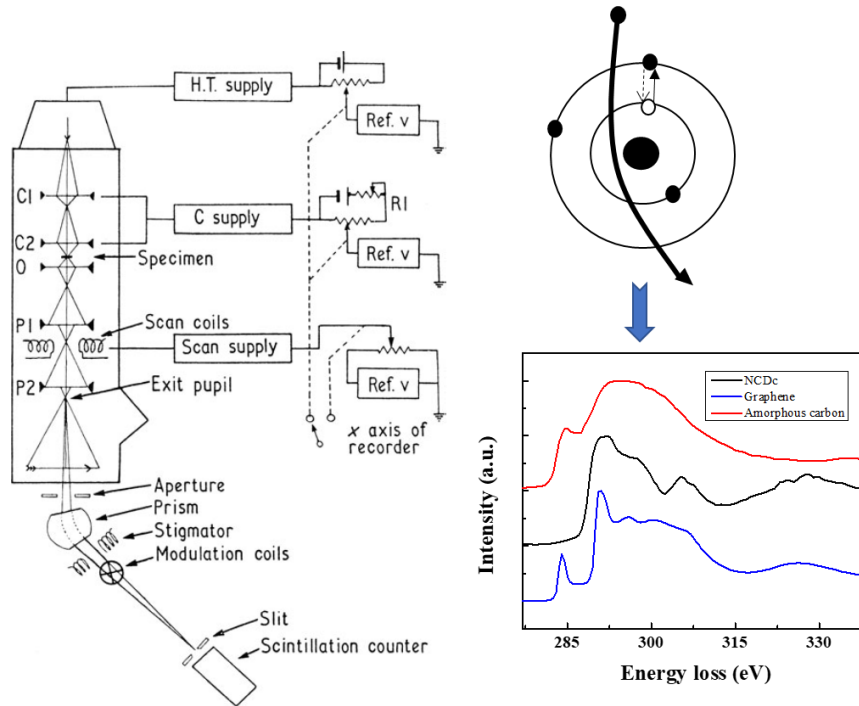
Figure 1.7 Schematic drawing of the instrumental setup and working principle of EELS(Ray F Egerton, 2011) The inelastic interaction between incoming electrons and sample makes the electron loss its energy. The different materials structure can leads to different spectrum, the comparison of the EELS of nanocrystalline diamond, graphite, amorphous carbon as example.

1.3.4 Scanning transmission X-ray spectromicroscopy – near edge X-ray absorption fine spectroscopy (STXM-NEXAFS)

Developing to a third generation design, synchrotron facilities have demonstrated powerful capabilities for materials characterization, including 4D X-ray tomography analysis, in-situ live biological study, high-end chip analysis, and highly-accurate elemental analysis.(Arrua, Hitchcock, Hon, West, & Hilder, 2014; N. D. Bassim et al., 2012; A. P. Hitchcock & Toney, 2014; Melo et al., 2017; Wu et al., 2018) STXM-NEXAFS is one of the powerful techniques developed for the synchrotron facility. By using the 10ID1 beamline at Canadian Light Source (CLS), STXM-NEXAFS has contributed much to research in the energy materials sector. Researchers also try to push the limit of STXM by novel instrument designing, such as the development of cryo-STXM at CLS. Basically, when the X-ray with a specific energy passes through the sample, part of it can be absorbed by the element for the state excitation. By measuring amount of the X-ray absorbed,

certain information about the sample can be obtained. The detail of the working principle and the experimental procedure of STXM and the corresponding data analysis will be discussed in more detail in chapter 2 and 3. As shown in the table 1.1, although EELS has higher spatial resolution and ease of access, the higher energy resolution and lowered beam damage during the characterization process make the use of STXM-NEXAFS more favored in this research. (Jiang, 2013; Jiang & Spence, 2012; Leontowich, Hitchcock, & Egerton, 2016; Jian Wang, Botton, West, & Hitchcock, 2009; J. Wang, C. Morin, et al., 2009)

Table 1.1 Comparison between STXM-NEXAFS and STEM-EELS technique

	STXM	**EELS**
Source	Soft X-ray	Electrons
Energy of source	130 – 2700 eV	80 keV, 200 keV, and 300 keV
Spatial resolution	~15 nm	Several Ångström
Energy resolution	0.1 eV (43 meV at best)	0.5~1 eV (50 meV at best for HB Titan in CCEM)
Damage to the sample	Relatively low	High
Instrument	10ID1 beamline at CLS	Transmission electron microscope
Suitability for polymer study	Good	Relatively poor
Mechanisms	Energy absorption	Energy loss

1.4 Materials selections and related properties

To investigate the detailed mechanisms of FIB damage on the soft materials, we select three kinds of polymers in different application areas for testing, Embed 812 epoxy resin, poly(methyl methacrylate) (PMMA) and polyvinylidene fluoride (PVDF), which are three classic soft materials used in the bio-application, microelectronic lithography and high performance plastics.

1.4.1 Soft materials in biomaterials application (Embed 812)

Embed 812 is an epoxy resin which is a widely-used embedding materials for the research of biology and biomaterials. It is a replacement for EPON 812 from Electron Microscopy Science (EMS) company and has the similar excellent properties like greater contrast, ease of mechanical sectioning and relatively stability under the electron beam.(EMSCompany) The basic components for the Embed 812 kit include Embed 812, Dodecenylsuccinic anhydride (DDSA) as the softener, 2,4,6-Tris(dimethylaminomethyl)phenol (DMP-30) as the accelerator and Methyl-5-norbornene-2,3-dicarboxylic anhydride (NMA) as hardener. With different mixing ratios and curing condition, the properties of the final embedding resin will also be different. In this research project, we mainly focus on the hard resin and we will strictly follow the mixing instruction from the EMS company website. The basic chemical information and physical information for Embed 812 have been show in the table 1.2 and 1.3.

Table 1.2 Basic chemical information of Embed 812 kit (Sigma-Aldrich-Company)
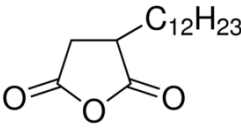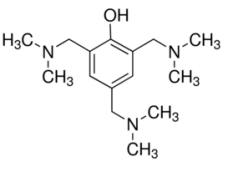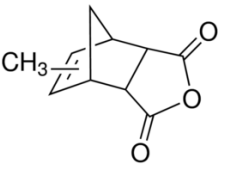
	Chemical structure	Role
Embed 812 epoxy resin	Unknown	Resin
Dodecenylsuccinic anhydride (DDSA)		Softener
2,4,6-Tris(dimethylaminomethyl)phenol (DMP-30)		Accelerator
Methyl-5-norbornene-2,3-dicarboxylic anhydride (NMA)		Hardener
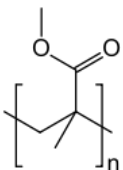
Table 1.3 Basic physical information for Embed 812 (EMSCompany; Sawyer, Grubb, & Meyers, 2008):

Glass transition temperature	Possible thermal conductivity	Boiling point	Flash point	Crystallinity status
Unknown	0.168 W/m.K (0.15–0.25 W/mK) for many epoxy resin	>444K	413K	Single phase all-amorphous thermoset polymer

1.4.2. Soft materials in microelectronics lithography (PMMA)

PMMA, also known as acrylic glass, is a typical glassy thermoplastic material with versatile applications. Its chain-scission properties under the irradiation of moderately accelerated electron beams allows it to be used as a positive tone electron beam resist for the lithographic application. (Carbaugh et al., 2016) Besides, when irradiated under high doses of electrons, it can turn into a negative tone resist. (Duan et al., 2010) Table 1.4 lists the basic information of PMMA we may need for building model and results analysis.
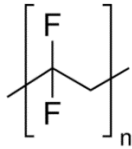
Table 1.4 Basic information for PMMA (Porter & Blum, 2000; Smith & Hashemi, 2006):

Full name	Chemical structure	Melting point	Glass transition temperature	Thermal conductivity	Boiling point	Crystallinity status
Poly(methyl methacrylate)		433K	381K	0.167-0.25 W/m.K	473K	Single phase all-amorphous thermoplastic materials

1.4.3. Soft materials in high performance plastics (PVDF)

PVDF is a widely used high performance fluoropolymer-based plastic in many areas, including the electrical wire protection, pipe fabrication and piezoelectric sensing. The study of FIB damage on PVDF can help its application in small sensor applications at the micro or nano level and help study the interaction of PVDF membrane and the protein in the biomedical application. (Kang & Cao, 2014)

Table 2.4 Basic information of PVDF (EMSCompany):

Full name	Chemical structure	Melting point	Glass transition temperature	Thermal conductivity	Boiling point	Crystallinity status
Poly(1,1-difluoroethylene)		428-438K	211K	0.19 W/m.K	-	Single phase semi-crystalline thermoplastic materials

1.5 Outline of thesis

This thesis aims to study the beam damage mechanisms of FIB-SEM system on soft materials, with the main focusing on studying the electron beam damage on EMbed 812 epoxy resin. The results can be useful for optimization of FIB-SEM microscopy on soft materials, especially FIB-based 3D tomography on epoxy resin embedded biological samples.

Chapter 2 mainly describes the working principle of FIB-SEM system, STXM, and fundamental ideas of finite element simulation on ion beam heating of FIB.

Chapter 3 describes the electron irradiated sample preparation, including preparation of thin film and irradiation strategy by SEM. Details of beam heating simulation will also be provided.

Chapter 4 describes the effect of beam voltage and electron dose on the 100 nm epoxy resin thin film. This work shows that 2 kV electron beam can result in more radiolysis damage than the 1 and 5 kV cases. Besides, the relationship between beam voltage and carbon contamination has also been discussed in this chapter.

Chapter 5 describes the effect of electron dose and dose rate on the 100 nm PVDF thin film sample. It has been found that with more dose and dose rate, the degree of electron damage on PVDF sample is more significant. The STXM results shows that, the loss of fluorine is one of the main indicators of the electron beam damage in the PVDF thin film.

Chapter 6 describes the current work done on the simulation of the ion beam induced heating problem of FIB by using COMSOL finite element software. The work shows the effect of the time step size on the simulation results and the effect of different dwell times on the beam heating results. The discussion will be extended to how the simulation results will help improve the current FIB milling strategy especially for the final lift-out step.

Chapter 7 gives a conclusion of all the work done in this thesis and provides some suggestions forfuture work.

Appendix presents additional information

Chapter 2 Methodology

This chapter describe the configurations and the basic working principles of FIB-SEM system and STXM-NEXAFS. The basic principle of the beam heating simulation is also described in detail and compared with others previous beam heating models of FIB. The details of how these methods are used in this thesis can be found in chapter 3.

2.1 FIB-SEM system configuration and working principle

As mentioned in the 1.1 section, the FIB-SEM system integrates both SEM and FIB into one single machine, with an angle of 54° between the electron column and ion column. Figure 2.1 shows the image of the latest FEI Helios G4 UXe DualBeam Plasma-FIB located at CCEM.
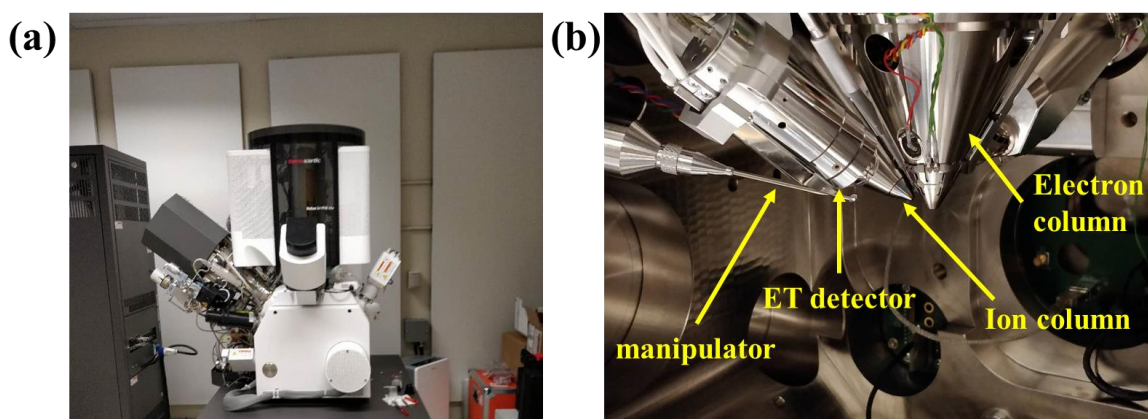
Figure 2.1 Images of FEI Helios G4 UXe DualBeam Plasma-FIB located at CCEM: (a) Overview image of the outlook of the PFIB, (b) The layout of the inner chamber of PFIB

The electron column in the system is like the column in most SEMs, with the electron gun, apertures, condenser lens, scanning coil, and electromagnetic lenses and electrostatic scan coils. Figure 2.2 (a) shows a schematic configuration plot of the electron column for a typical SEM.(Goldstein et al., 2017) The layout of the ion column is similar to the electron column, but the different physical properties of ions makes the configuration more complicated than that of electron column, as shown in figure 2.2 (b).(Orloff, 1993)

Due to the different properties of different ions, people designed different ion sources for the generation of different ion beams. The liquid metal ion source (LIMS) is the most common used method for Ga-based FIB, which made use of the low vapor pressure properties of the Ga metal and the formation of Taylor cone, shown in the schematic drawing in figure 2.2 (c). As to the Xe-based FIB, figure 2.2 (d) gives a very good illustrative drawing on the inductively coupled plasma source, which uses the radio frequency current to generate the Xe ions inductively.

Although both electrons and ions are charged particles and the columns look similar from outside, the different mass/charge properties make the focusing principles different. The low mass/charge ratio of electrons allow them to be focused easily by the magnetic lens, which is what one expects from a normal SEM. On the other hand, ions can be only focused by using electric fields and the conditions for a precise focusing are very rigid. For example, it takes a lot more effort to focus the ion beam than electron beam when the accelerating voltage is changed.(Lucille A Giannuzzi, 2004; Orloff, 1993)

In a typical operation process, the sample is first imaged and focused by the SEM. Then the sample is tilted about 52° to be orthogonal to the ion beam for the imaging and focusing. After ensuring that working distance of the sample is adjusted so that the sample can be imaged by both SEM and FIB images, the sample should arrive at the central tilt axis, also known as the eucentric point. All operations, including milling, FIB deposition, and imaging by FIB, should be conducted at this location for the best result. Figure 2.3 (a) and (b) illustrate of the common FIB-SEM applications for advanced microscopy studies, the high-precision ultrathin TEM sample preparation and FIB tomography respectively. These can be achieved due to the addition of the SEM as an "eye" during the FIB milling procedure.
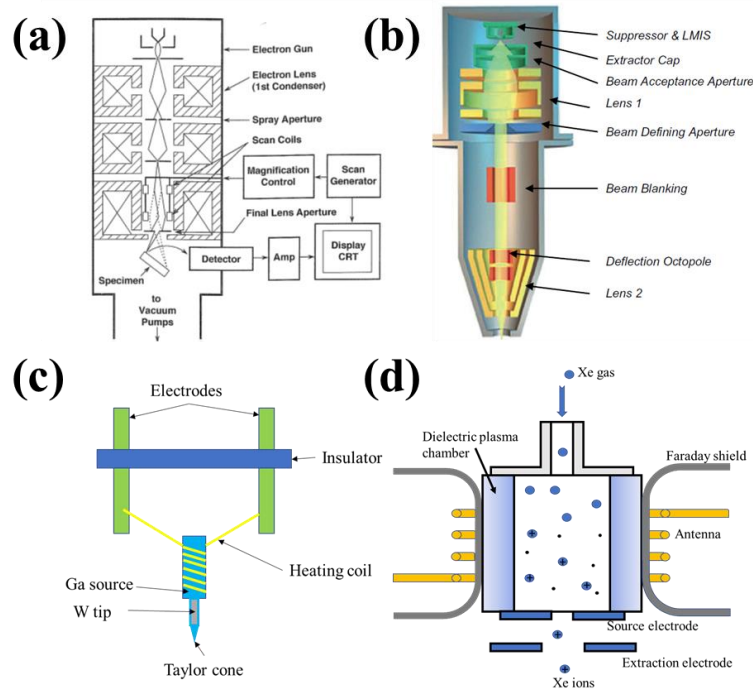
Figure 2.2 (a) Schematic configuration plot of the electron column for a typical SEM (b) Schematic drawing of a common FIB (c) Schematic plot of Ga source ion gun in FIB (d) Schematic drawing of Xe ion gun source.(N. Bassim et al., 2014; Belianinov et al., 2017; Goldstein et al., 2017; Orloff, 1993)
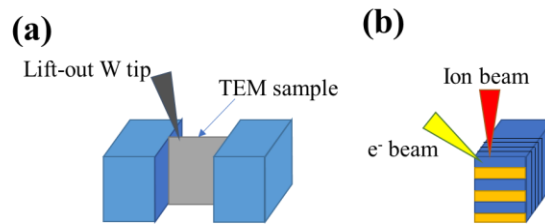
Figure 2.3 show the schematic drawing on how (a) an ultra-thin TEM sample and (b) the 3D tomography can be achieved by the FIB-SEM system. The SEM imaging can make the FIB milling more accurate and controllable.

2.2 CLS beam line system configuration and STXM-NEXAFS working principle

Synchrotron radiation (SR) is the radiation generated from accelerating high energy charge particles either by natural sources, such as cosmic background radiation, or human-made facilities, such as the Canadian Light Source (CLS). SR has a broad range of applications in various studies, including tomography, imaging, and chemical composition analysis etc (Willmott, 2011). The third generation synchrotron design can generate the electromagnetic (synchrotron) radiation by changing the direction of the accelerating electrons at highly relativistic velocities via bending magnets.(Willmott, 2011) As shown in figure 2.4 (a), various types of X-rays are produced by the Canadian Light Source (CLS) and used for different characterization purposes, forming characterization stations known as beamlines. The beamline we used in this thesis is 10ID1 soft X-ray beamline, shown as soft X-ray microscopy (SM) in figure 2.4 (a) and is used, mainly for STXM and photoemission electron microscopy (PEEM) characterization. Figure 2.4 (b) is the image of the beamline extended from the CLS synchrotron ring. The X-rays pass through the extended tube and are used to analyze the sample in a separate room from the source.

The instrumental layout and the basic working principle of STXM-NEXAFS has been illustrated in figure 2.5. After passing through the Fresnel zone plate, the central stop will block the zero order of the monochromatic X-ray and the order sorting aperture (OSA) will only let the first order light to be focused on the sample. The detector will detect the intensity of the transmitted X-ray. We then can calculate the optical density (OD) by using the Lambert – Beer's Law: $OD = \ln(\frac{I_0}{I_t})$, where I_0 is the incident X-ray intensity and I_t is the transmitted light intensity. When an X-ray passes through the sample, it can interact with the sample by exciting some inner shell ground state electrons to excited states and the photons with certain energies are absorbed, which thus forms the absorption spectrum as the result. Figure 2.6 shows the schematic drawing of the formation of F 1s STXM spectrum of the pristine PVDF sample used in this thesis. The incoming X-ray photon can excite one F 1s electron to $\sigma^*_{C-F} \perp$ or $\sigma^*_{C-F} \parallel$ levels which are the lowest unoccupied molecular orbital (LUMO) and LUMO + 1 of the PVDF. Thus one can see there are two absorption peaks in the spectrum around 690 eV position and these are the characteristic peaks for the PVDF

polymer. If an alteration of these peaks is found in another sample after electron or ion beam irradiation, one may speculate that there should be some chemical change in that sample. Usually, people use the "stack" method to characterize the sample, which acquires incremental STXM images within a certain energy range of interest, such as 680 eV – 720 eV for F 1s spectrum, with each image taken at a designated energy interval. Each stack is a set of images taken under certain photon energies. One can then use this multidimensional dataset either to extract spectral maps of the sample, or as energy-filtered images. Usually, we prepare our sample thin enough to prevent the Carbon signal saturation issues and the best thickness for our sample is around 100 nm, considering both the requirement of STXM and the availability of the sample preparation technique we have.
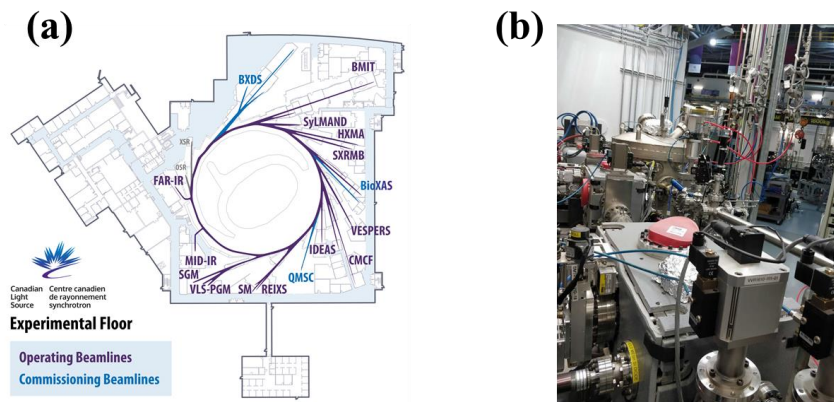
Figure 2.4 (a) The beamline distribution map of the Canadian Light Source (CLS) (b) The image of 10ID1 beamline at CLS.
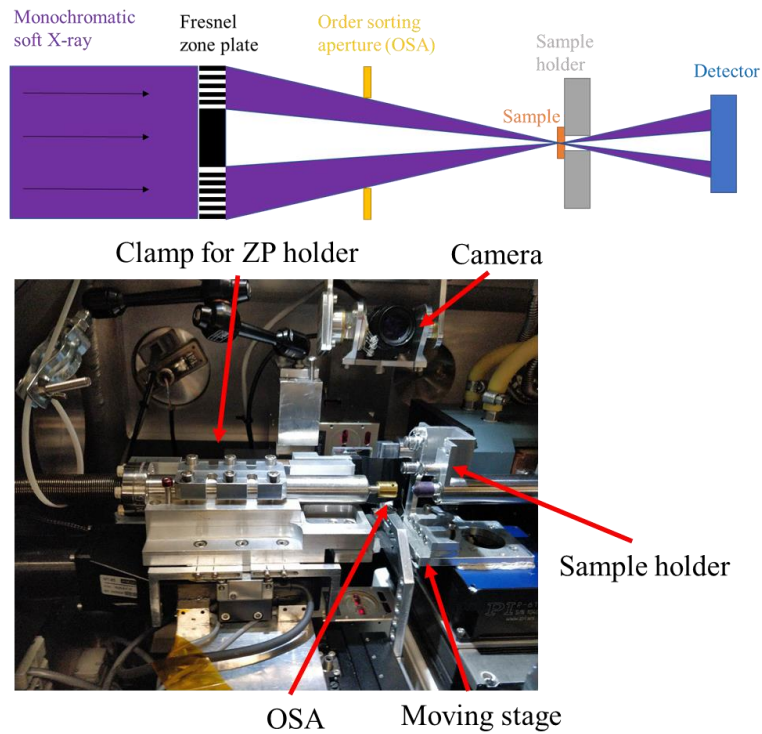
Figure 2.5 shows the schematic drawing and the image of the STXM instrumental configuration.
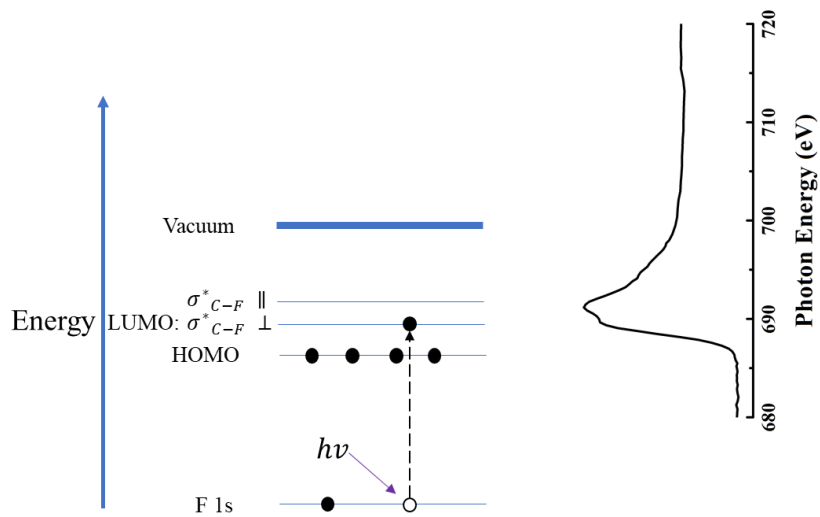
Figure 2.6 shows the schematic drawing of the STXM-NEXAFS working principle. The NEXAFS spectrum of pristine PVDF thin film is shown on the right.

2.3 Principle for ion beam induced heat transfer simulation

Because not all of the energy of an incident ion can be used for the sputtering, backscattering, and the generation of secondary ions/electrons, the rest of the energy is deposited into the sample, which causes nuclear vibrations (or phonons) and generates heat. Due to the strong stopping power for ions injected into sample, the ion-matter interaction is usually confined to a small region near to the sample surface. With heat confined in a small region, it can cause a rapid localized temperature rise. In 1995, Ishitani et. al. proposed a simple model to predict the temperature rise associated with FIB, following a formalism from laser beam heating. He assumed the FIB-induced heat region to be hemisphere-like with double the beam size of FIB.(Ishitani & Kaga, 1995) He predicted a less than 100 K temperature rise for Si and GaAs under the 30 keV FIB and a much higher temperature for SiO_2 sample due to the lower thermal conductivity and diffusivity of heat.(Ishitani & Kaga, 1995) However, since the interaction volume of the ion is much smaller than the laser, the model is inappropriate to consider the hemisphere-shape heat region. Later in 2014, Schmied et al. took the ion-matter interaction into consideration by combining the phonon distribution calculated by SRIM and the thermal spike model, and developed a new approach to predict the temperature rise of the FIB.(Schmied et al., 2014; Vineyard, 1976) The SRIM simulation is an open source software package that gives a relatively good prediction of the ion trajectory into the matter by considering both the nuclear and electronic stopping powers during the ion/matter interaction process. SRIM will be discussed in detail in the later chapters when simulated ions are "implanted" into target materials with Monte Carlo-based algorithms. (Ziegler, Ziegler, & Biersack, 2010)

By contrast with the heating associated with phonon generation, an alternative method for treating the heat rise in a sample is the thermal spike model. The thermal spike model considers the heat deposited by the energetic particle as instantaneously imparting a local temperature rise and follows the classic heat transfer law in the continuum matter, and gives a prediction of the potential temperature rise.(Szenes et al., 2000; Vineyard, 1976) This model predicts a surprisingly high temperature rise, above 6000 K, for PMMA under 30 kV 500 pA Ga-based FIB, which is far beyond the decomposition temperature for most materials.(Schmied et al., 2014) Although the ion-matter interaction volume was carefully considered by adopting the SRIM model, the model developed by Schmied is less convincing due to several reasons. First of all, the model does not

consider the phase change of the polymer during the heating process. With the increasing temperature, the change of the phase in the polymer can have the changing thermal properties, for example, the heat capacity of PMMA will increase with the temperature. Second, Schmied mistakenly adopted the thermal spike model in his model by assuming the phonon distribution calculated from SRIM to have a fixed absolute value. This mistake can be easily identified by the unreasonably high temperature rise derived from his simulation. The 6000 K temperature rise can definitely lead to the visible explosion during the milling process, but there is no report on this phenomenon. Third, the phonon distribution generated by SRIM is only a probability distribution, and the value of the phonon energy won't change with more simulated ions. Therefore, the temperature obtained from Schmied's model is not real, and cannot predict how the temperature change with the dwell time of the ion beam. Recently Wolff et. al. published a model of evolved heat due to FIB by comparing the methods of the Fourier's law of heat transfer, the finite element simulation, and numerical modeling.(Wolff et al., 2018) Using a finite element software package, COMSOL, the heating event can be visualized in a more vivid way. However, it may take a long time to simulate a line milling in the real world and the author did not consider the distribution of the ion beam, which may in fact reduce the heating effect due to the spreading of the ion beam.

Therefore, we develop a more efficient FIB heat transfer model to predict the temperature rise during the milling process. The idea of this model was developed based on the previous models including Schmied's and Wolff's models. Like Schmied's model, we use the phonon distribution generated from SRIM to be the shape of the heating source in the model. Unlike Schmied, we treated the phonon distribution to be a probability distribution of the heat, dividing the value of each point in the map by the integration value over the whole map. Besides, we treat the ion injection as a continuum process instead of sequential isolated events for speeding up the simulation process. The heat flux input into the sample is then the heat flux of the ion beam times the probability distribution derived from the phonon distribution. By treating the heat source like this, we can also move the heat source during the process to simulate the real milling process with moving of the ion beam during raster milling. To take the phase change of the polymer during the heating process into account, the heat capacity of the polymer was not fixed and replaced with its temperature-heat capacity curve. The moving of the ion beam (heat source) is described by a step function, which we can later use to study the effect of different dwell times and beam overlap on

the temperature rise by adjusting the step function. Table 2.x summarize the comparison of our model with others previous models. The results of our calculations and simulations will be presented in Chapter 6.

Table 2.1 Comparison between different model for the beam induced heat transfer simulation(Ishitani & Kaga, 1995; Schmied et al., 2014; Wolff et al., 2018)

	Ishitani's model	Schmied's model	Wolff's model	Our model
Description of heat source shape	Hemisphere	SRIM simulated phonon distribution with beam spreading	SRIM simulated phonon distribution without beam spreading	SRIM simulated phonon distribution with beam spreading
Heat source model	Laser-like	Thermal spike model	Ion's stopping power	Continuum heating with probability distribution
Accuracy	Low	Low	Very high	TBD
Speed of simulation	Very fast	Fast	Very slow	Fair
Capable of the prediction of real milling case	No	No	No	TBD
Consideration of phase change	No	No	No	Yes

Phonon distribution generated by SRIM

Curve fitting for power input

Heat capacity changes with temperature

Step function for beam moving mimicking
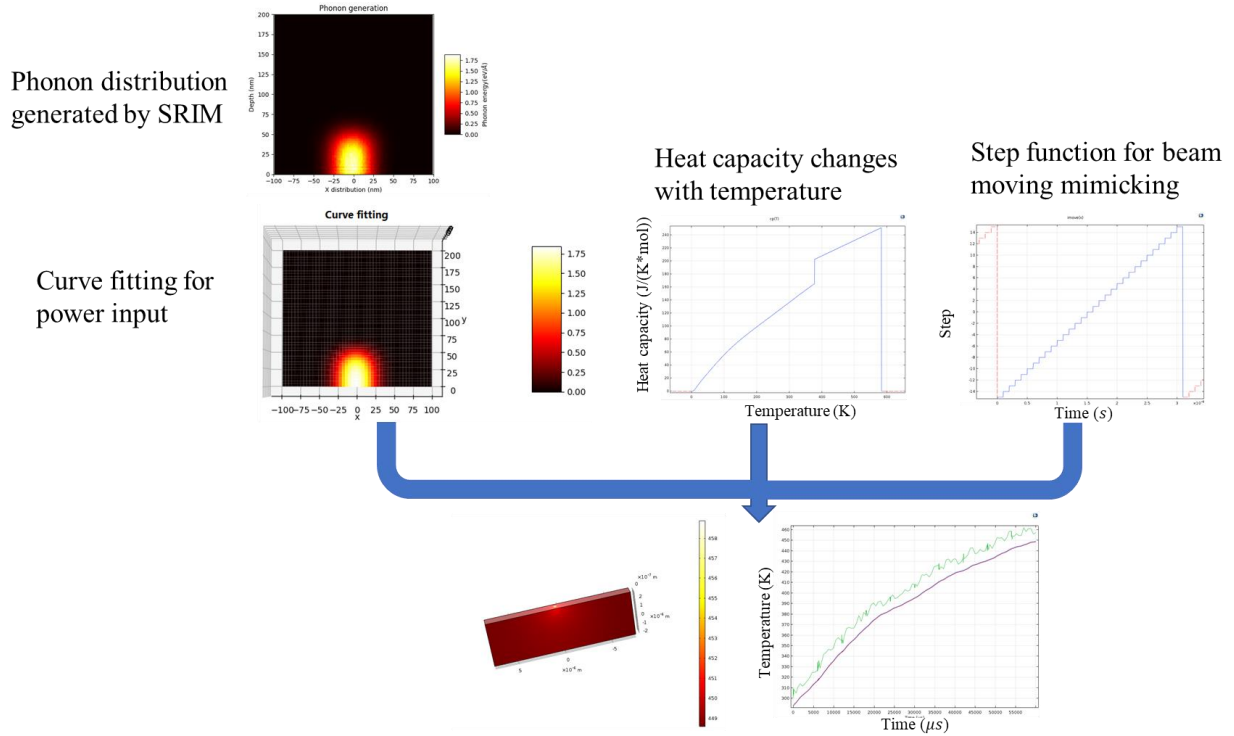
Figure 2.7 shows the schematic drawing of the simulation process. With the combination of SRIM, a dynamic milling step, and changing heat capacity, the model can be more realistic.

Chapter 3 Experimental procedure

This chapter describes sample preparation steps, including the synthesis of the EMbed 812 epoxy resin and ultramicrotomy prepared polymer thin film. The electron irradiation dosing arrays by SEM are also described in detail. The STXM acquisition and data processing procedures are also discussed in this chapter. Details of FIB heat transfer simulation by COMSOL are also provided in this chapter, including how the ion injection is customized, curve fitting methods, and the preliminary results.

3.1 Preparation of polymer thin films and automated pattern electron irradiation by SEM

3.1.1 Bulk polymer sample preparation

Two main polymer materials are mainly investigated in this thesis, EMbed 812 epoxy resin and polyvinylidene fluoride (PVDF). The bulk samples of PVDF were purchased from Sigma-Aldrich company. The purchased PVDF samples are pellet-shaped, with the molecular weight from 70000 to 110000. The EMbed 812 epoxy resin was synthesized according to the protocol provided by Electron Microscopy Science (EMS) company. In each batch of the resin sample, we mixed 20 mL EMbed812, 9 mL Dodecenylsuccinic anhydride (DDSA), 12 mL N-methylolacrylamide (NMA), and 0.72 mL 2,4,6-Tris (dimethylaminomethyl) phenol (DMP-30) with the stirring machine to fully mix the chemical solutions. The part of the mixture then was injected into the mold and transferred to the oven with temperature fixed at 60°C curing for 24 hours. The rest of the uncured resin was stored in the sealed syringe in the fridge for use in the next round of experiment.

3.1.2 Thin film polymer sample prepared by ultramicrotomy

For the STXM characterization, the samples are required to be around 100 nm to avoid saturation of carbon signal. A FIB lift-out method, which approximates the steps required to do TEM sample preparation, will bring both damage from electron beam and ion beam, and poses difficulties in distinguishing the tangled relationship between ions and electrons. Spin coating is also a popular method for various thin film preparation. The high viscosity and the poisonous hazard of the

uncured resin mixture make it hard to control the film quality in a safe way. Therefore, the best option for the thin film preparation left is through the ultramicrotomy. Figure 3.1 shows the schematic drawing of the ultramicrotomy. The sample mounted on the holder is sliced into thin film by the diamond knife and floated on the liquid in the container of the ultramicrotome. The sliced thin films were then floated into TEM grids for later electron irradiation and STXM characterization. Different types of TEM grids can have some influence on the final morphologies of the film laid on the grids. As shown in figure 3.2 (a) and (b), with the use of bare TEM grid, both resin PVDF films wrinkled severely while freestanding. The wrinkling is a challenge for an accurate STXM analysis. Most data analysis assumes the film has a uniform thickness, the wrinkling of the film can cause change of the path length of the transmitted X-ray, leading to the change in the absorption and thus the height of the peak in the spectrum. This can be confusing since it is hard to tell whether the change of the peak height is from the film wrinkling or the beam induced mass-loss damage. Therefore, it is crucial to prepare the polymer film in a flat and uniform manner. One way to do that is using the formvar carbon-coated TEM grid. Besides, about 5 nm gold was also sputter-coated on the TEM grid as well to mitigate the charging problem but not influence the X-ray absorption too much. Figure 3.2 (c) and (d) show the resin and PVDF films laid on the Au and formvar coated TEM grids in a very flat manner, respectively.
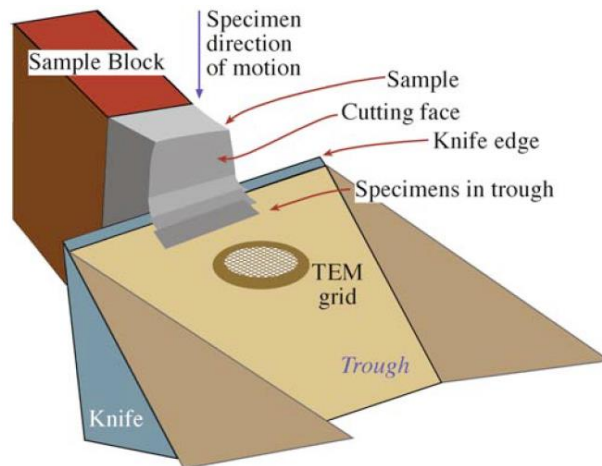
Figure 3.1 schematic drawing of the working principle of ultramicrotomy for thin film sample preparation.(Williams & Carter, 1996)
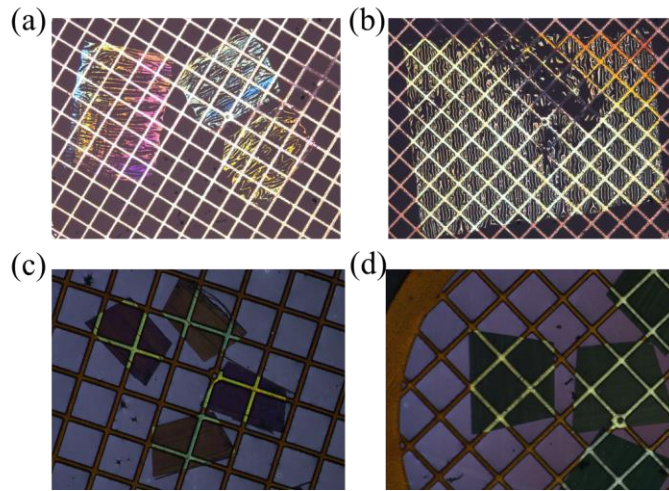
Figure 3.2 Polymer films on different TEM grids. (a) PVDF on bare copper TEM grid. (b) Resin thin film on the bare Cu TEM grid. (c) PVDF and (d) resin thin films on the Au and formvar coated TEM grid. The wrinkling is more severe for the films on the bare grids than the Au and formvar coated grids.

3.1.3 9-pad pattern electron irradiation by SEM

Optical microscopy was used to exam the film quality and identify the desired locations prior to the irradiation by SEM. It is better to identify the locations by OM instead of SEM to minimize the unnecessary electron dose. The desired locations are often the places with the polymer film covering more than half of the square region on the grids, leaving one corner.

An FEI Magellan 400 SEM was used to pattern dose arrays of electron irradiation in this research, as shown in figure 3.3. Compared with other available SEMs in the Canadian Centre for Electron Microscopy (CCEM), the Magellan is the most modern and capable of high-resolution imaging. The major advantage of Magellan is that we can let the pattern irradiation process to be programmably controlled by computer. As shown in the schematic drawing in figure 3.4, starting from the corner of the square, the beam was manually focused to minimize the beam spreading for a better dose control. Then, the desired parameters were input in sequence and let the computer to run the irradiation pattern automatically, with a combination of beam currents, doses and stage motions. If any beam parameters were changed, the beam was moved back to the origin place, the corner of the square and refocused manually before the next run. Otherwise, the change of the

beam parameters can not only cause the beam defocusing, leading to severe beam spreading, but also shift the actual beam position, resulting in a messsy irradiation pattern. After the pattern irradiation, the samples were extracted from the SEM without any further imaging on the pattern area and were prepared for STXM characterization.
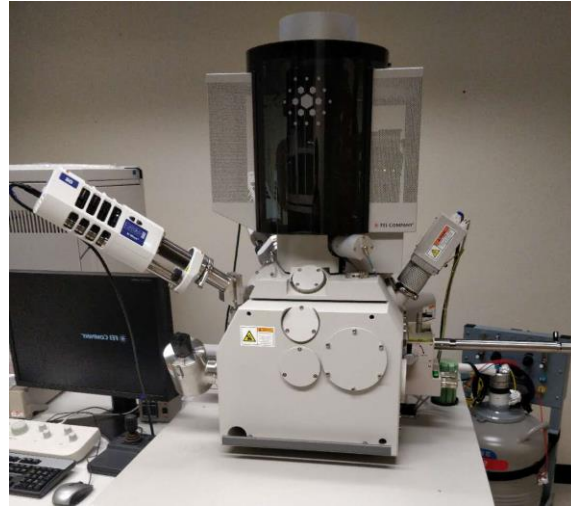
Figure 3.3 FEI Magellan 400 SEM at CCEM used for the 9-pad pattern irradiation experiment.
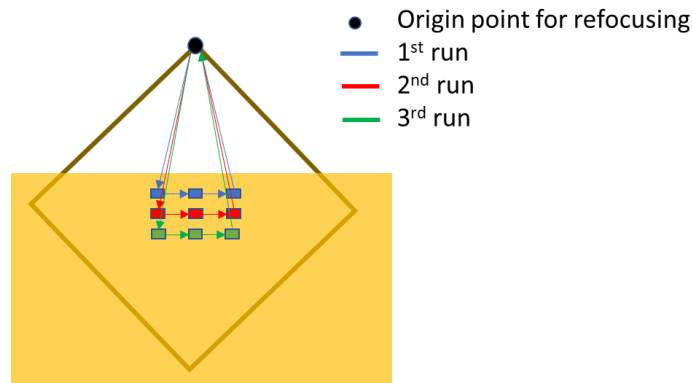
Figure 3.4 Schematic diagram of auto-run pattern irradiation process. After each run, the electron beam will move back to the origin point for parameters changes and refocusing.

3.2 Characterization by STXM

3.2.1 Optical microscope examination and sample mounting

Optical microscopy was used to identify whether the damage patterns were successfully created or not. Usually, if the irradiation process is successful, there should be noticeable pattern under OM due to carbon contamination, reduced thickness, and other beam damage making the reflective/transmitted light intensity different than the rest part of film. This is also why the flat film is the most desirable configuration for this study. After ensuring that the damage patterns were created on the film, the samples were mounted on the special holder for STXM by carefully taping the TEM grid onto the holder. Figure 3.5 shows how the samples are mounted on the Al special holder for STXM characterization.

Figure 3.5 Samples on the special holder for STXM characterization. The TEM grids are on the holes for the experiments.

3.2.2 Beamline operation procedure

All the STXM characterization was done with the help from Dr. L. G. A. Melo or Dr. A. Hitchcock by using the ambient STXM at Canadian Light Source (CLS) 10ID1 beamline. Images and stacks at C 1s and F 1s edges were acquired for the analysis of PVDF thin films. Images and stacks at C 1s and O 1s edges were acquired for the characterization of EMbed 812 epoxy resin thin film. Before the characterization, calibrations of energy scales of C 1s, O 1s, and F 1s were done using

C 1s(C = O) → $\pi^*_{C=O}$ transition of PMMA at 288.54 eV, O 1s(C = O) → $\pi^*_{C=O}$ transition of CO_2 at 535.4 eV, and F 1s → a_{1g} transition of SF_6 at 688.3 eV respectively.

For the beam damaged PVDF samples, the C 1s is acquired from the energy range 278 – 320 eV with 1 ms dwelling time and 200 nm pixel size. The energy range for F 1s is 690 – 720 eV. For the beam damaged resin sample, the energy range is 278 – 315 eV for C 1s scanning, and 524 – 560 eV for O 1s, with 2 ms dwell time and 250 nm pixel size.

3.2.3 Data processing

After the data acquisition from STXM at CLS, all the data was processed by the aXis 2000 software package developed based on IDL platform (Adam P. Hitchcock, 2019). The basic data processing includes selecting the proper area on the stack image data as the input of I_0 to calculate optical density. The reason why we did the 9-pad pattern irradiation near the edge of the film is to allow us to have the area for (which is the fully transmitted beam) I_0 near the characterized part of the sample as shown in the figure 3.6 and make the analysis more quantifiable. The red square region is used for I_0. The I_0 could reduce the influence of the formvar film background influence on the spectrum we got.

The other thing which is relatively important is to make sure the uniformity of the thin film sample for a good quantitative analysis result. One common way is to use the atomic force microscopy (AFM) method to physically detect the roughness of the sample. However, the AFM tip can easily damage our sample without extremely careful operation and thus ruin the sample ready for STXM characterization. As mentioned before, the absorption of the X-ray also depends on the sample thickness, so we can indirectly assess the film uniformity via the STXM image. To do this, we put the masks on the I_0 area and 9-pad pattern area and get an optical density histogram of the rest area which is the undamaged thin film as shown in figure 3.7. If the standard deviation of the histogram is smaller than 10% of the mean value, the full width at half maximum (FWHM) of the histogram, of the optical density, we can say that the film is uniformly flat and the follow-up quantitative analysis is reliable. If the chemical formula of the sample is known, one can even estimate the film thickness via the equation $OD = \mu(E)\rho t$, where $\mu(E)$ is the mass absorption coefficient at X-ray energy E, correlated with the sample's chemical formula, ρ is the density, and t is the thickness.

By using this, we estimated that the first PVDF sample to be around 200~300 nm, which is very thick for this analysis. For the resin, though it looks like a better condition than PVDF film, we cannot estimate its thickness due to the unknown chemical formula of the epoxy resin. After ensuring the sample is in a good quality, we then can analyze the spectra of the 9 irradiated pads and compare with each other to dig out the relationship between the electron beam parameters and the degree of induced damage for the purpose of this thesis.
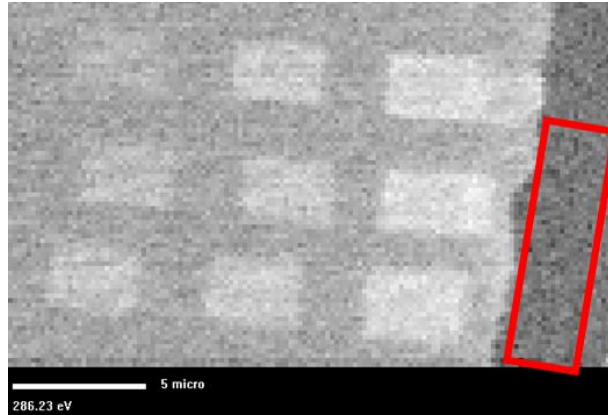
Figure 3.6 The STXM image of the 9 irradiated pads areas. The area highlighted by the red rectangle is used for the I_0
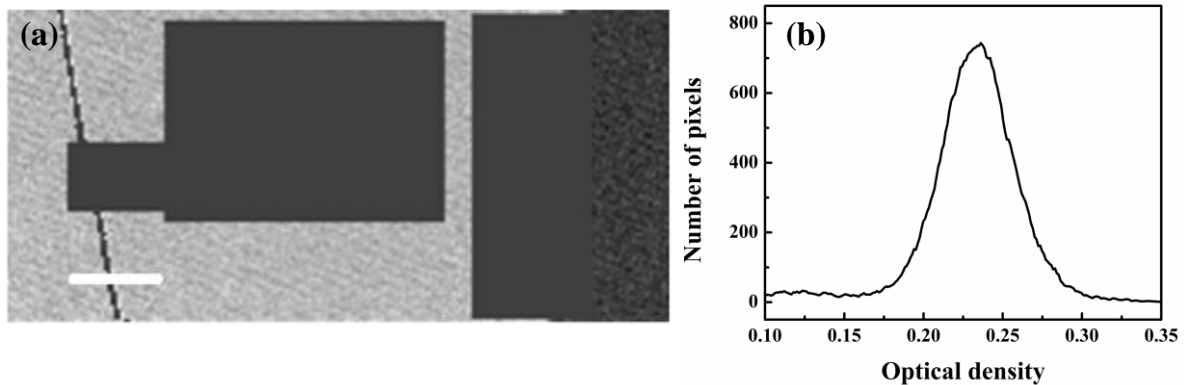
Figure 3.7 Method for assess the film uniformity via STXM image. (a) The image of the undamaged part of the film with thee irradiated area and the I_0 area covered by the gray mask. (b) The optical density histogram distribution of the undamaged part. If the standard deviation is less than the 10% of the mean value, we can expect that the uniformity of the film is good.

3.3 Details of ion beam induced heat transfer simulation

3.3.1 SRIM simulation of the ion trajectory events and phonon distribution

The Stopping and Range of Ions in Matter (SRIM) is a popular Monte Carlo simulation software package for calculating the trajectory events of ions into different materials(Ziegler et al., 2010). The simulation considers the effects of both nuclear and electronic stopping powers during the ion trajectory and the simulation results have been widely recognized as accurate enough in different fields of research, including semiconductor, high-energy physics, and FIB milling etc. Although there are also many evolving molecular dynamic (MD)-based simulations about ion trajectory events due to FIB, we chose to utilize SRIM due to a more efficient and more adaptive framework for polymer study. To simulate the trajectory events of 10^5 ions into a system, SRIM may need about 2 hours to finish the most complicated case in the software, while the MD based software usually needs several tens of times long than the SRIM. Since the scale of this research aims at micron scale, the difference in the results might be negligible. Besides, MD usually requires the system in the simulation to be well-known, like a crystallized system, for an accurate result. Therefore, MC-based SRIM can do a better job in predicting the ion trajectory events in the amorphous system than MD based simulation and in a reasonable timeframe.

In the default setting for SRIM simulations, the input ion beam is assumed to be single-point entry injection with no aberration and no beam spread as shown in Figure 3.10 (a). However, in the real case, the ion beam can only be focused to less than 10 nm due to the strong Coulomb repulsion force among ions. Besides, the ion beam aberration is also a problem for fine milling purpose. To achieve a more realistic simulation of the ion trajectory, we take the beam spreading of the ion beam into consideration by customizing the beam input data by the SRIM Supporting Software Module. I assumed the beam spreading to be Gaussian distribution like with the beam radius of 20 nm, the full width at half maximum (FWHM) of 40 nm for the Gaussian distribution, and 2 eV for energy spread. Then the simulated trajectory path of our customized ion beam is shown in the figure 3.9 (b). By selecting the phonon distribution in the software, we can generate the phonon distribution from SRIM. Since the phonon distribution also depends on the trajectory shape of the ion beam, customized beam can be also found in the phonon distribution, as shown in figure (c). Therefore, incorporating proper distribution of the ion beam can be very important for the accurate heat transfer simulation.
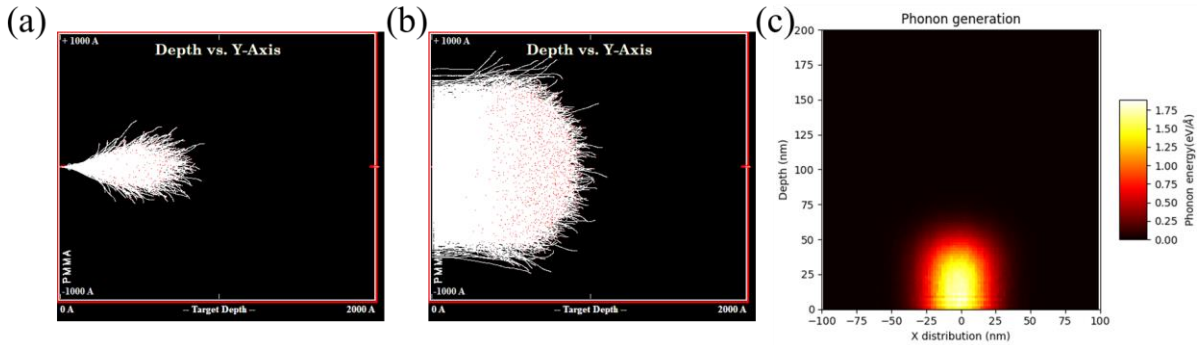
Figure 3.9 (a) SRIM simulation with default injective ion beam input. (b) SRIM simulation with customized injective ion beam input. (c) Phonon generation got from the simulation by using customized beam input.

3.3.2 Curve fitting for heat flux and optimized parameters setting

As mentioned in the previous section, the phonon distribution generated by SRIM is not the real one. Therefore, I convert it into the probability distribution through normalizing it by dividing each point with the integration value of the whole map. Then since the distribution map is a 2D dot map, a high-order Gaussian distribution function was used to fit the generated map. Using a Python Gaussian curve fitting package, we are capable to get a good curve fitting. The fitting of the phonon distrubtion results are shown in figure 3.10 (a), with the residual of the fitting shown in figure 3.10 (b). Since SRIM generated phonon distribution is 2D, we convert it into 3D by replacing x with $\sqrt{x^2 + y^2}$. The final probability function for the heat flux can be obtained via using a curve fitting script in Python.

To make our simulation more applicable to a real FIB column, the heat capacity used is not fixed but changes with the temperature. Figure 3.11 (a) shows the heat capacity as the function of time for PMMA from the website. The use of changing of heat capacity can also compensate the influence of the phase change during the heating process. Besides, as we treat the heat source not like a fixed input as others models, we can make the simulated heat source move like what it should do in the actual FIB milling process. A step function was developed to mimic the milling process, with considering of dwell time of each point and continuous connection between consequential

points. The step function is shown in the figure 3.12 (b). One can also change the dwell time to

studying the effect of dwell time on the beam heating process.
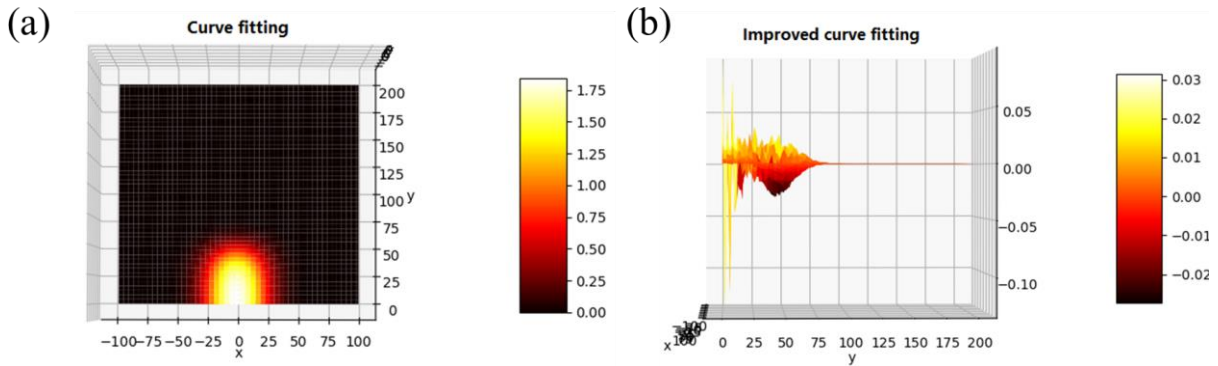
Figure 3.10 (a) Curve fitting of the phonon distribution for the customized power input. (b) The fitting residual distribution.
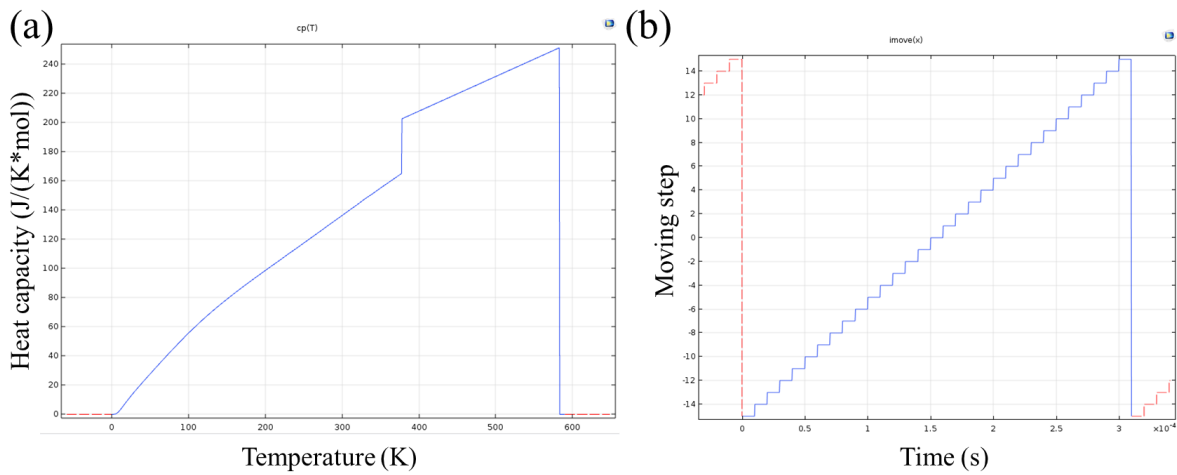
Figure 3.11 (a) Step function mimicking the real raster milling beam path. (b) Heat capacity as the function of temperature for PMMA.

3.3.3 Heat transfer simulation by COMSOL

The main body of the heat transfer simulation is achieved by using the finite element simulation software COMSOL. COMSOL is a commonly-used commercial Multiphysics simulation application for the research in the fields of novel energy materials study, acoustic study of automotive design, heat transfer in various applications etc. To achieve an efficient simulation, the shape of the sample for the simulation is designed to be $15\mu m \times 8\mu m \times 0.8\mu m$, which is small enough for calculation purposes but also a reasonable size of the FIB lift-out sample in the final milling step without the consideration of the Pt/C deposited layer. Besides, a TEM lift-out sample geometry is chosen also because heating damage can be more severe in the thin sample and is often most significant in the final milling step rather than the initial step. The simulated time for the whole process is 60000µs, with various time step size. The simulations were mainly run on a computer with 2.20GHz Intel(R) Xeon(R) E5-2698 v4 CPU, 128 GB RAM, and 3 GB Nvidia GeForce GTX 1060 graphic cards. The estimated for a run of 60000 µs with 5 µs step size is about 1.5 hours. A preliminary simulated result is shown in figure 3.12. The size of the simulated result is about 26 GB per file and increases with the ratio of total-time/step-size. The results of the heat transfer simulation will be discussed in detail in chapter 6.
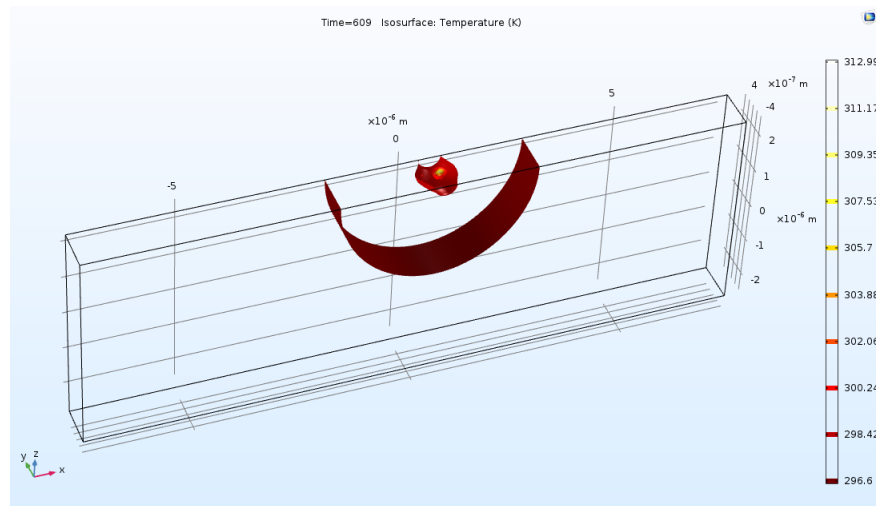
Figure 3.12 Temperature contour for beam heating on PMMA simulation over 600 seconds.

Chapter 4 Effect of beam voltage and electron dose on the electron damage on EMbed 812 epoxy resin thin film

*This chapter reports the effect of different beam voltage and electron dose on the electron damage on the 100 nm EMbed 812 epoxy resin thin film. We found that the 2 kV electron beam voltage can result in more radiolysis damage. The carbon contamination can be treated as the dynamic result of the electron desorption and carbon deposition process during the electron irradiation and is found to be most severe under 2 kV in this study. The results of this chapter have been published in **Micron** journal. doi: 10.1016/j.micron.2019.02.003*

Electron beam damage of epoxy resin films studied by scanning transmission X-ray spectromicroscopy

Weiwei Zhang[a], Lis Melo[b], Adam P. Hitchcock[b], and Nabil Bassim[a,*]

a. Department of Materials Science and Engineering, McMaster University, Hamilton, ON, Canada

b. Department of Chemistry & Chemical Biology, McMaster University, Hamilton, ON, Canada

* Corresponding author. Tel. +1 (905)-525-9140 ext. 24102

Email address: bassimn@mcmaster.ca

Abstract:

Focused ion beam coupled with scanning electron microscopy (FIB-SEM) is a popular technique for advanced electron microscopy with applications such as, high-precision site-specific lamella sample preparation for transmission electron microscopy (TEM) and slice-and-view FIB 3-dimensional tomography. Damage caused by the electron imaging component of FIB-SEM may be compounded with damage from the ions during the ion milling process. There are known strategies for mitigating damage from ions and electrons (cryo-SEM, dose-control, voltage control), but the electron damage on common embedding resins for EM has not been explored in detail beyond their resistance to shape-change. The relationship between beam parameters and damage mechanisms remains unclear. Since we are relying on the physical, chemical and thermal stability of embedded samples during ion-beam milling, it is important to distinguish electron beam damage from ion beam damage. Scanning transmission X-ray microscopy (STXM) has been used for analyzing the electron beam radiation damage on polymer films by characterizing the chemical bonding changes. In this paper, we mainly focus on the effect of beam voltage and electron dose on the damage to epoxy resin thin films. Irradiated areas on polymer thin films were characterized by near edge X-ray absorption fine structure (NEXAFS) in STXM. We found that, even under low current and voltage, the electron beam can still cause noticeable chemical changes within the polymer film. The degree of electron beam damage depends not only on the beam energy, but also on the amount of inelastic scattering occurring within the material, as determined by the sample thickness.

Keywords: electron beam damage, scanning transmission X-ray microscopy, carbon deposition, epoxy resin film

4.1 Introduction

Coupled with scanning electron microscopy (SEM), focused ion beam (FIB) microscopy is used extensively for high precision site-specific lamella sample preparation for transmission electron microscopy (TEM), 2D piezoelectric materials preparation, nano-milling, and 3D FIB tomography (N. Bassim et al., 2014; Burnett et al., 2016; L. A. Giannuzzi & Stevie, 1999; X. Li, Sun, Shan, et

al., 2018; X. Li, Sun, Wei, Shan, & Chen, 2018). However, for soft materials, the higher sensitivity to the ion/electron irradiation and lower thermal conductivity (R. F. Egerton et al., 2004; R. F. Egerton et al., 2006) poses challenges. To achieve high-quality FIB prepared samples and milling process for 3D tomography, a further understanding of the damage mechanisms involved in the FIB-SEM system needs to be explored. Previous research found that the chemical damage in soft materials is mainly caused by the irradiation of electron beam (N. D. Bassim et al., 2012). Compared with the curtaining artifacts and heating damage, the chemical changes induced by the electron irradiation during the SEM component of FIB/SEM use is usually neglected when considering the milling process, but its effect may not be negligible (N. D. Bassim et al., 2012).

Researchers have studied electron beam (e-beam) damage in perovskite materials, nanomaterials, and polymers and have had some success in understanding the damage features in these materials and the underlying mechanisms (Lehnert, Lehtinen, Algara-Siller, & Kaiser, 2017; Rothmann et al., 2018; J. Wang, G. A. Button, et al., 2009; Xu, Shi, Zhang, Wong, & Li, 2011). Due to the wide variability of soft materials, few solid conclusions have been drawn to explain the damage mechanisms prescriptively enough for practical applications in the FIB-SEM.

The material chosen for this study was EMbed 812 epoxy resin, a popular polymer for embedding biological samples for TEM study and FIB-SEM 3D tomography (Tapia et al., 2012). Bubbling and other chemical degradation, which can come from the electron beam damage (Koval, Borzenko, & Dubonos, 2003; Scott, 2011), often limits the high-quality sample preparation or milling of biomaterials. Little research has been carried out on the chemical changes due to the electron beam irradiation of epoxy resin embedding polymers (Longieras, Sebban, Palmas, Rivaton, & Gardette, 2007).

In this paper, we studied the effects of beam voltage and dose on low-energy electron induced damage to 100 nm thick epoxy resin thin films. The damaged areas were created in a 3×3 scanning pattern on the resin thin film by a scanning electron microscope. The irradiated areas were later characterized with near-edge X-ray absorption fine structure (NEXAFS) in a scanning transmission X-ray microscope (STXM) (Hitchcock, 2012) at 10ID1 beamline at the Canadian Light Source (CLS). We found that, even at low beam current, the electron beam can still cause chemical alteration and carbon contamination on the resin thin film. We also found that, at the same electron dose, the degree of electron beam damage depends on the amount of inelastic

scattering occurring within the material, which is determined in part by the thickness of thin film polymer samples. In this situation the beam voltage necessary for FIB-SEM applications such as TEM sample preparation and serial sectioning becomes an important parameter. Carbon contamination, as a dynamic result of the mass loss and deposition process, was observed to be most severe in the case of 2 kV imaging condition in this study.

4.2 Materials and methods

4.2.1 Preparation of polymer films:

The EMbed812 epoxy resin (Electron Microscopy Science) was synthesized following the manufacturer protocol: 20 mL EMbed812, 9 mL Dodecenylsuccinic anhydride (DDSA), 12 mL N-methylolacrylamide (NMA), and 0.72 mL 2,4,6-Tris (dimethylaminomethyl) phenol (DMP-30) was mixed and cured at $60\,°C$ for 24 hours. The cured resin was then sectioned to about 100 nm films by a Leica ultramicrotome (model Leica Ultracut UCT). The sectioned resin film was then placed on a 200 mesh Cu grid which had been coated previously with 30 nm formvar carbon and 5nm sputter-coated gold. The formvar supports the resin thin film and provides film-grid adhesion, while the gold layer is used to minimize charging during SEM exposure.

4.2.2 Electron irradiation patterning:

The electron beam patterning irradiation was done using a ThermoFischer-FEI Magellan 400 SEM. Before the irradiation patterning, the microscope chamber was cleaned by a plasma cleaner for 20 minutes resulting in a vacuum of $5\times10^{-4}Pa$. The beam current was fixed to be 50pA through the whole study to minimize both carbon contamination and charging. The voltage of the electron beam was varied from 1 kV to 5 kV to cover commonly-used parameters for imaging soft materials (David C. Joy & Joy, 1995; D. C. Joy & Joy, 1998). Each exposed area was approximately $3\mu m\times2\mu m$. As mentioned by Egerton, the common critical dose for organic materials in TEM application is 0.01 C/cm^2, (R. F. Egerton, Lazar, & Libera, 2012). In this experiment, we did not install a Faraday cup for measuring the exact beam current, so the exposure (which is proportional to dose for thin samples) was calculated using

$$Exposure = \frac{Beam\ current \times Exposure\ time}{Scanning\ area} \qquad \text{(Eqn. 1)}$$

Since the beam current and the scanning area are fixed, exposure time is monitored to get the desired electron dose in this experiment. A 3×3 scanning pattern was used and the dose parameters are shown in table 4.1. Python scripts were used to control the exposure time and create the pattern automatically to reduce the effect of unwanted electron irradiation due to manual operation. For clarification, the term 'dose' commonly used in electron-microscopy studies usually refers to the electron exposure (units of C/cm^2), rather than radiation dose (absorbed energy per mass, in units of $J/kg = Gray$) commonly used in other radiation damage studies (Du & Jacobsen, 2018; R. F. Egerton et al., 2004). For thin samples this is a reasonable approximation since the energy deposited by inelastic scattering is only a small portion of the total e-beam energy (Jiang & Spence, 2012). In this study, the irradiation process was strictly controlled by the computer program with fixed beam current and scanning area. The computer-controlled exposure time was varied to achieve the desired doses.

4.2.3 Materials characterization

The irradiated resin film was characterized by using near-edge fine-structure absorption spectroscopy (NEXAFS) measured in the ambient scanning transmission X-ray microscope (STXM) at the 10ID-1 beamline at the Canadian Light Source (CLS). A defocused beam size of 250 nm and a step size of 250 nm were used to avoid any X-ray damage. Imaging at 288.3 eV, an energy very sensitive to radiation damage, after STXM acquisition did not show any damage (see supplementary information **Fig. S-4.1**). The optical density (OD) at each photon energy was calculated from the transmitted intensity, I, and the incident intensity, I_0, using the Lambert-Beer law: $OD = -\ln\left(\frac{I}{I_0}\right)$ (Stöhr, 2013). Peaks in the absorption spectra are related to excitation of inner-shell electrons to unoccupied molecular orbitals. C 1s and O 1s image sequences (also called stacks) (Jacobsen, Wirick, Flynn, & Zimba, 2000) were acquired.

4.2.4 Monte Carlo Simulation

The electron trajectory was simulated using a Monte Carlo simulation package, named monte CArlo SImulation of electroN trajectory in sOlids (CASINO v2.5.0) (Drouin, 2011).

Since the chemical formula of the EMbed 812 resin is unknown and proprietary, we chose 100 nm PMMA thin films as the simulated material model due to the similarity of the STXM spectra

Figure 4.1 (a) Reflection mode optical image of the 100 nm resin thin film on the TEM grid. A magnified image of the 9-pad irradiated areas outlined by the white box is inset in the upper-right corner. (b) C 1s spectra of undamaged and damaged (pad 4) resin, taken from a 93 energy stack measured by STXM using a defocused spot to minimize X-ray damage. (c) Color coded composite of the undamaged (green) and damaged (red) component maps obtained by fitting the C 1s stack to the spectra in Fig. 1b.   (d) O 1s spectra of undamaged and damaged (pad 4) resin, taken from a 54 energy stacks measured by STXM using a defocused spot. (e) Color coded composite of the undamaged (green) and damaged (red) component maps obtained by fitting the O 1s stack to the spectra in Fig. 4.1d. The scale bars in Fig 4.1c, 1e are 5 μm.

of Embed812 and PMMA. 1, 2 and 5 kV beam voltage cases were simulated, with the beam size of 10 nm set as default. The remaining parameters were set to default values.

4.3 Results

An optical image of the electron beam 9-pad irradiated pattern is shown in **Figure 4.1a**. An image sequence, consisting of images at 93 photon energies from 278 to 320 eV was measured, aligned and converted to optical density. **Figure 4.1b** are C 1s spectra extracted from the undamaged area between the pads and from the most heavily damaged pad (pad #4). The aligned, optical density image sequence was fit to the C 1s spectra (Fig. 1b) to generate component maps of the undamaged and damaged resin. **Figure 4.1c** is a color-coded composite with the undamaged map in green and the damaged map in red. **Figure 4.1d** presents the O 1s spectra extracted from the undamaged region and from the most heavily damaged pad (pad #4). **Figure 4.1e** is a color-coded composite with the undamaged map in green and the damaged map in red. The color composites show that the largest extent of damage occurred for a beam energy of 2 kV and the longest exposure time used (200 s). This indicates a relationship between the extent of damage and the physical appearance of the irradiated areas under the optical microscope and STXM. Based on the spectra in **Fig.4.1 (b) (d)**, one can also see that the chemical bonding changes dramatically between the undamaged part and the severely irradiated part of the resin film. From the pixel intensity histogram of the non-irradiated area (supplementary information **Figure S-4.1**), the resin film appears to be uniform. Given that the sample is uniform, it appears that the 2 kV electron beam generates more damage to the resin film than the 1 and 5 kV electron beams, for the same exposure time.

The C 1s NEXAFS spectra of the resin film areas damaged by the 1, 2, and 5 kV electron beam are shown in **Figure 4.2**. The STXM spectrum of the non-irradiated area is also plotted. There are three main features of the non-damaged resin spectrum: the C $1s(C-H) \rightarrow 1\pi^*_{C=C}$ transition at 285.3 eV, the C $1s(C=O) \rightarrow 1\pi^*_{C=O}$ transition at 288.4 eV, and a broad continuum peak centered around 293.2 eV due to C $1s(C-H) \rightarrow 1\pi^*_{C-C}$ transitions (Urquhart & Ade, 2002).

Table 4.1 Beam parameters used for the scanning pattern

Voltage	Dose & Exposure Time		
	0.1 C/cm^2 (200 secs)	0.01 C/cm^2 (20 secs)	0.001 C/cm^2 (2 secs)
5 kV	Area 1	Area 2	Area 3
2 kV	Area 4	Area 5	Area 6
1 kV	Area 7	Area 8	Area 9
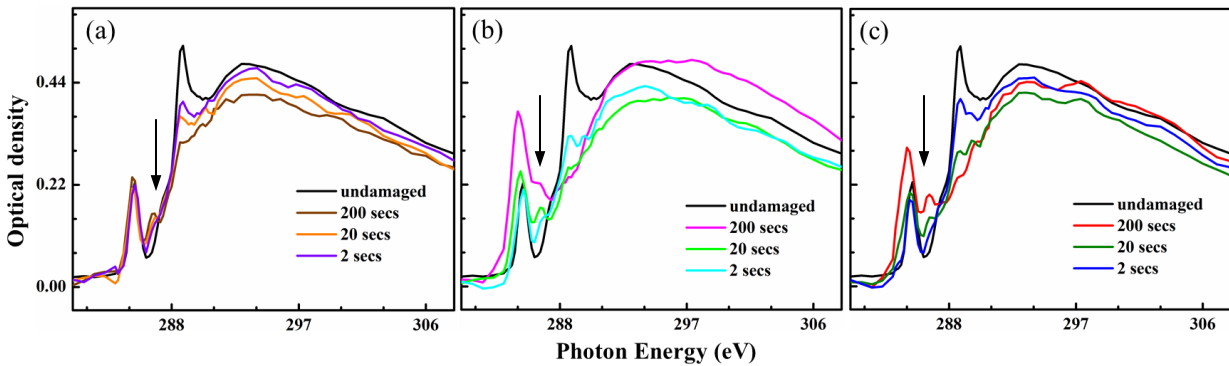
Figure 4.2. Comparison of the C 1s spectra of the resin thin film irradiated areas by an electron beam at 2, 20 and 200 secs using a beam voltage of (a) 1 kV, (b) 2 kV, and (c) 5 kV. The STXM spectrum of undamaged sample is plotted as black line in each graph as the reference. The arrow in each figure shows the position of the newly created C 1s → σ*$_{C-O}$ damage peak at 286.6 eV.

4.3.1 Chemical analysis of full C 1s spectra

With longer exposure time a new peak arises at 286.6 eV which is related to the formation of $C-O$ bonds (see Fig. 4.2). The intensity of this peak increases with longer exposure times and thus is due to electron irradiation damage to the resin thin film. Similarly, the intensity of the 288.4 eV peak (most likely a C 1s $\rightarrow \pi^*_{O-C=O}$ transition) decreases with increasing exposure time in all

cases. The height and shape of the broad peak at 293 eV changes with the exposure time as well as with the electron beam voltage. The peak height decreases with the exposure time when the applied beam voltage is 1 kV, which is similar as the trend of the 288.4 eV peak. In the case of 2 kV beam voltage, a 20 second exposure time led to the lowest intensity of the 293 eV peak while the 200 second irradiation resulted in the highest peak. The shape of the 293.2 eV also becomes broader after 20 seconds electron beam irradiation as shown in **Fig 4.2 (b)**. For 5 kV electron beam irradiation, the 293 eV peak is the weakest for 20 s exposure. The height of the 293.2 eV peaks in the spectra of the 2 and 200 second irradiated pads are similar but have different peak widths. The increase of the 285.3 eV peak and the broadening of the 293 eV peak may be signatures of deposited amorphous carbon (Leontowich & Hitchcock, 2012). Based on the changes of the peak height and shape of the 9 irradiated areas, the area with 2 kV electron beam irradiation for 20 seconds is identified as the area with the most severe carbon contamination caused by the electron beam deposition.

4.3.2 Effect of beam voltage and exposure time on the radiation damage
To study the chemical changes mainly from the radiation, we select the areas with minimal carbon contamination for comparison, region 3,6,9 for studying the influence of beam voltage and region 7, 8, 9 for studying the effect of exposure time. **Figure 4.3(a, b)** shows the C 1s spectra of selected irradiated, for the purpose of studying the effect of beam voltage and exposure time on the damage induced by the radiation. **Fig 4.3(a)** shows the spectra of the irradiated areas under 1 kV beam voltage irradiation with varied exposure time, where the carbon contamination is minimal. The extent of radiation damage increases with the exposure time as indicated by the increase in the intensity of the 286.6 eV peak and the diminishing of the 288.4 eV peak. The decreasing of 288.4 eV peak with exposure time indicates that the electron beam damage breaks $C = O$ bonds. Similar observations were found in previous STXM studies of photon irradiated PMMA films (Leontowich et al., 2012; J. Wang, C. Morin, et al., 2009). Similarly, in **Fig 4.3(b)**, the 2 kV electron beam resulted in the most severe radiation damage to the 100 nm resin thin film. The carbon contamination was minimized with 2 seconds exposure time.

Figure 4.3(c, d) show the corresponding O 1s spectra for the same areas selected in **Fig 4.3 (a, b)**. The sharp peak at 532 eV in the spectrum of the non-irradiated area is due to O 1s $\rightarrow \pi^{*}_{C=O}$ transitions. With longer exposure time, the 532 eV peak decreases and shifts to lower energy,

which are the features for radiation damage to the O 1s spectrum in this study. The decrease in intensity of the 538.5 eV peak indicates that the resin film lost oxygen with longer exposure time. For 2 second irradiation, the 2 kV electron beam resulted in the most significant peak shift and peak drop, indicating the most severe damage, consistent with the result of **Fig 4.3 (b)**.
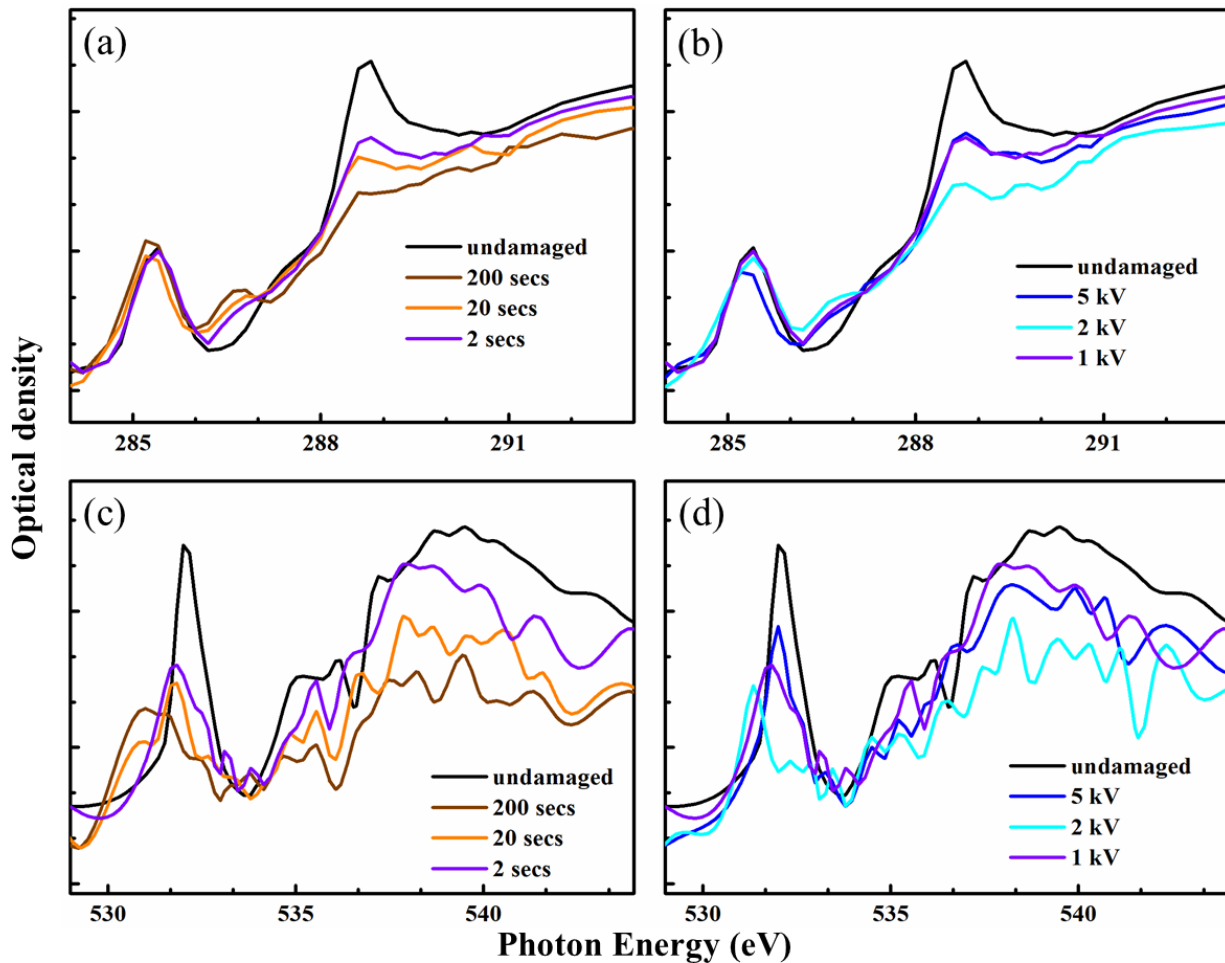
Figure 4.3. C 1s and O 1s spectra of radiation damaged resin thin film. (a) C 1s spectra for 1 kV electron beam irradiation for 2 seconds, 20 seconds and 200 seconds. (b) C 1s spectra for 2 second irradiation with voltages of 5 kV, 2 kV and 1 kV. (c) O 1s spectra for 1 kV electron beam irradiation for 2 seconds, 20 seconds and 200 seconds exposure. (d) O 1s spectra for 2 second irradiation with voltages of 5 kV, 2 kV and 1 kV.

4.3.3 Monte Carlo Simulation by CASINO

Due to the unknown chemical composition of this commercial polymer, we selected PMMA as the material to simulate the electron trajectory and the distribution of inelastic electron scattering. The simulated electron trajectory results for the 1, 2 and 5 kV beam voltages are shown in **Figure 4.4**. For a 100 nm polymer thin film, the depth of the interaction volume for a 1 kV electron beam is about 40 nm, and the inelastic scattering region is confined to a relatively shallow volume of the thin film. The depth of the interaction volume for a 2 kV electron beam is around 100 nm, similar to the thin film thickness, and the inelastic scattering is distributed widely across all of the thin film. The 5 kV electron beam requires a larger interaction volume than provided by the resin film so that most electrons pass through the sample and the probability of inelastic scattering within the film is much lower. The simulation graphically illustrates why the 2 keV beam energy exhibits the highest extent of radiation damage.
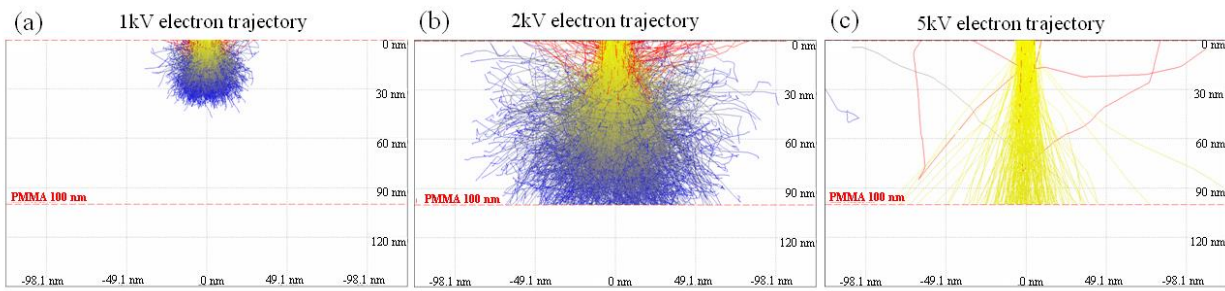
Figure 4.4. CASINO Monte Carlo simulation of electron trajectory in 100 nm PMMA thin film with beam voltages of (a) 1 kV, (b) 2 kV, and (c) 5 kV. The red lines refer to the simulated tracks of backscattered electrons that exit the sample. The yellow to blue transition indicates the electron energy decreasing from the incident energy to lowest allowed energy, 0.0001 keV, in each simulated track.

4.4 Discussion

There are two main types of electron beam damage categorized by different electron-matter interactions: elastic scattering due to electron-nucleus interaction (knock-on) and inelastic

scattering due to electron-electron interaction (radiolysis) (R. F. Egerton et al., 2004). Soft materials, like organic specimens and biomaterials, are very sensitive to inelastic scattering of the electrons and are often degraded by the radiolysis damage (R. F. Egerton et al., 2004; R. F. Egerton et al., 2006). Beam heating may also be a problem for thin films. For example, a polymer thin film may encounter a few hundred degrees temperature rise if it is under stationary electron beam irradiation (R. F. Egerton et al., 2004). However, the heating effect can be negligible under small beam current conditions for most beam diameters in a scanning mode due to the small dwell time (R. F. Egerton et al., 2004). Therefore, the electron beam damage mechanisms discussed in the following are limited to e-beam induced mass loss, structural damage and mass loss (radiolysis), and e-beam induced deposition (i.e. carbon contamination).

Before we did the irradiation patterning process, we confirmed that the damage observed by STXM came from the intentional electron beam exposure rather than a mixture of intentional patterned damage and background irradiation caused by the navigation process for locating the desired area. To do this we used STXM to measure the spectra of a pristine resin thin film which never went into the SEM chamber. The STXM spectra of the pristine resin film and the spectra of regions with no intentional irradiation on the damaged film are essentially the same (see Supporting Information, **Figure S-4.2**). The spectral shapes are identical; there is only a small change of the absolute OD which is due to a slightly different thickness of the two films. Therefore, we can say that chemical change induced by navigation imaging and residence in the SEM chamber is negligible.

4.4.1 Carbon contamination
Carbon contamination due to electron beam induced carbon deposition is a common problem in SEMs and may be the result of competition of induced mass loss and gain processes(R. F. Egerton et al., 2004). As we discussed in section 4.3.1 for the case of 1 kV beam irradiation, the C 1s continuum peak height decreases with longer exposure time mainly due to the mass loss. The effect of carbon contamination is minimal. When the beam voltages were 2 and 5 kV, with longer exposure time the amount of carbon first decreases due to mass loss, which we attribute to the electron beam-induced mass loss and radiolysis, and then increases due to beam-induced carbon deposition. The spectral signal of cracked carbon is growth of the C 1s $\rightarrow \pi^{*}_{C=C}$ peak at 285 eV. This is very significant, especially in the 2 kV electron beam irradiated pads. At relatively low voltages, the deposition rate may grow faster than the mass loss rate with increasing voltage. When

a 2 kV beam voltage is used the deposition process dominates, resulting in more deposited amorphous carbon. Under 5 kV electron beam irradiation, the mass loss process catches up with the deposition process, so the relative carbon content of the 5 kV irradiated areas appear to be similar with each other. The change of relative carbon content with different exposure time calculated from the STXM spectrum image can be found in the Supporting information **Figure S-4.3(a)** which confirms that the 2 kV e-beam did lead more severe mass loss as well as deposition process. One may also notice that a new peak at 286.6 eV appears in the spectra of all damaged areas (Fig. 4.2), which is a feature of radiolysis damage to the resin film.

4.4.2 Beam voltage and exposure time effect and Monte Carlo simulation

Based on the previous section, we know that higher beam voltage and longer exposure time can lead to a significant deposition and mass loss process. To characterize the chemical change from radiolysis, we used 1 kV and 2 s exposure time as the baseline for minimum carbon contamination. Under 1 kV beam irradiation, more damage will be introduced with longer exposure time, appearing as a lowered carbon content, as shown in the Supporting Information. The chemical bonding environment also changes with increased exposure time and appears as a drop of the 288.4 eV peak and a rise of the 286.6 eV peak. However, the amount of inelastic scattering events, which is the main cause of the chemical structure change, does not necessarily have a linear relationship with the beam voltage, due to the strong change in range with beam voltage in the range studied. In fact, in the case of a 100 nm resin film, 2 kV beam voltage leads to more radiolysis damage than 5 kV. This can be explained with the assistance of the results of the beam energy dependence of the electron trajectories in a 100 nm PMMA thin film which was simulated by the CASINO Monte Carlo simulation package. From the simulated results, at 2 kV beam voltage, the interaction volume is very similar to the thin film thickness, with a distribution of inelastic scattering very uniformly spread across the whole width of the film. In contrast, many of the 5 kV electrons pass completely through the thin film without inelastic scattering so that the total number of inelastic scattering events is much smaller than at 2 kV. For the 1 kV case, the interaction volume is quite small compared to the whole resin thin film thickness, confining the damage zone only to the top surface of the film and resulting in less damage. **Figure S-4.3(b)** gives a more direct view on the changes in the amount of C=O bonds as a function of exposure time and beam voltage. The extent of chemical change induced by the electron beam irradiation depends on how efficiently the

inelastic scattering is distributed across the thin film. The whole spectral comparisons results can be found in the supporting information (**Figure S4.4 & S4.5**).

For FIB-SEM serial sectioning tomography with a plasma FIB, the single slice thickness is usually around 100 nm, similar to the film thickness in this study. For gallium FIB, the slice thickness can be as low as 5 nm (Holzer & Cantoni, 2012). To minimize the radiation damage from the electron beam, a low beam voltage is preferable. However, a low beam voltage can lead to poor-quality compositional analysis due to the low yield of backscattering electrons. Since the cut face in serial sectioning is a flat block face and secondary electrons (SE) are sensitive to topography, the SE image would not provide as much information as the image formed by the backscattered electrons. A balance between signal yield and radiation damage needs to be explored. Despite carbon contamination and radiation damage, the extent of the radiolysis damage of a 2kV beam is closely matched to the typical slice thickness, of 100 nm, and thus the electron beam damage from the imaging will be milled away in preparing the next slice, leaving little damage for further imaging. The 5 kV beam did not cause much damage to the thin film in this study due to a greater penetration than the film thickness, but that means subsequent layers will be partially damaged from SEM imaging of the previous 2-3 slices. Essentially, we are depositing damage deeper into the sample. The accumulated damage may finally lead to more severe damage in soft materials. Therefore, a beam voltage of 2 kV may be a good choice for imaging during FIB/SEM slice-and-view 3D tomography, despite causing the highest radiation damage.

4.5 Summary

Irradiation damage by low voltage electron beams to EMbed 812 epoxy resin in a scanning electron microscope was studied using scanning transmission X-ray microscopy. We found that the carbon contamination is the dynamic result of electron induced carbon deposition and mass loss process and depends on the beam voltages and exposure time. In our study, a 2 kV electron beam energy led to the most severe carbon contamination of the resin thin film sample due to (i) close match of electron range and sample thickness, (ii) a more significant deposition process than mass loss process, and (iii) more radiolysis damage than a 1 keV or 5 keV beam energy. The decrease of the 288.3 eV peak height and increase of the 286 eV peak height can be attributed to $C = O$ bond breaking. Radiolysis damage of resin thin films depends not only on dose but also whether the

inelastic scattering is confined within the sample. We found that, for a 100 nm polymer film, radiolysis damage caused by the 2 kV electron beam is more severe than that from 1 kV or 5 kV. To achieve a balance between imaging quality and extent of electron beam damage, 2 kV is a good choice for SEM imaging in FIB/SEM 3D tomography applications to soft matter samples, when the slice thickness is ~100 nm.

Acknowledgements:

Supplementary information

Electron beam damage on epoxy resin film studied by scanning transmission X-ray spectromicroscopy

Weiwei Zhang[a], Lis Melo[b], Adam P. Hitchcock[b], and Nabil Bassim[a,*]

a. Department of Materials Science and Engineering, McMaster University, Hamilton, ON, Canada

b. Department of Chemistry & Chemical Biology, McMaster University, Hamilton, ON, Canada

Figure S4.1 (a) The STXM image of the resin film taken using a photon energy of 288.3 eV. The grey masks covering the unwanted region. Scale bar is 5 μm. (b) Histogram of optical density distribution to measure the uniformity of the thin film. The mean value of the optical density is 0.23. The standard deviation of the distribution is 0.02 (10%) which is small enough to justify that the film is uniform.
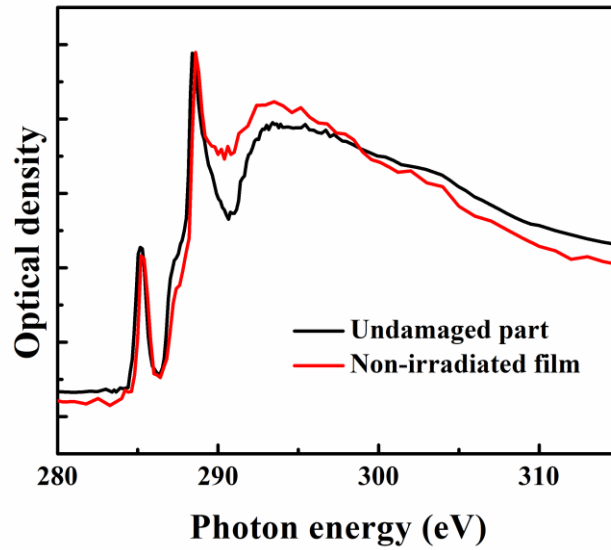
Figure S4.2 Comparison of rescaled C 1s STXM spectrum of pristine resin thin film (red curve) and the undamaged part of the resin film with irradiation pattern (black curve). The scaling factor is 1.75 for the spectra of non-irradiated film. No obvious difference between the spectra indicates that there is almost no effect of the background electron irradiation on the chemical alteration of the resin film.
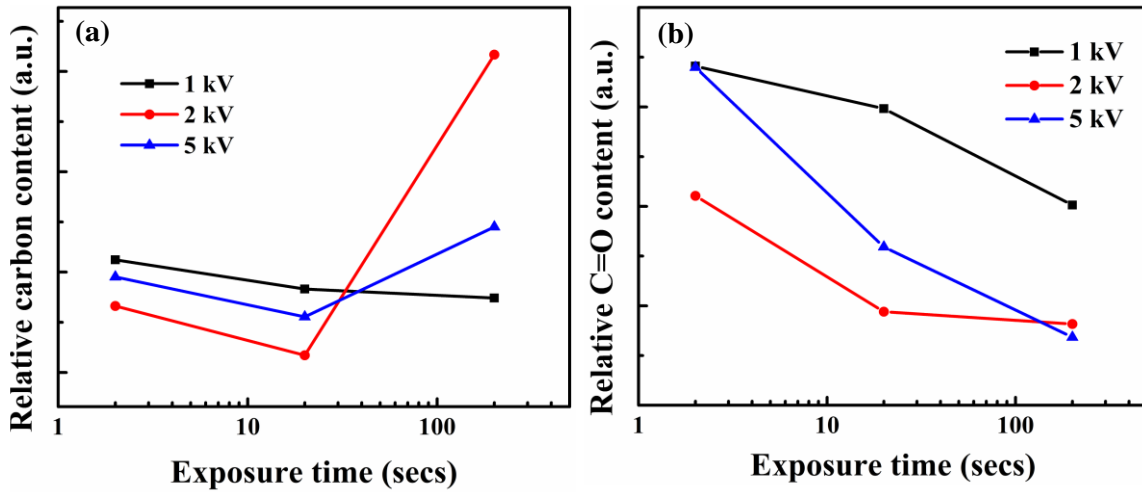
Figure S4.3 The change of (a) relative carbon content, measured by the integration of the whole spectrum after background subtraction (b) relative C=O content, measured by the integration of the range from 288 – 290 eV of the spectrum after background subtraction with different exposure time under different beam voltages.
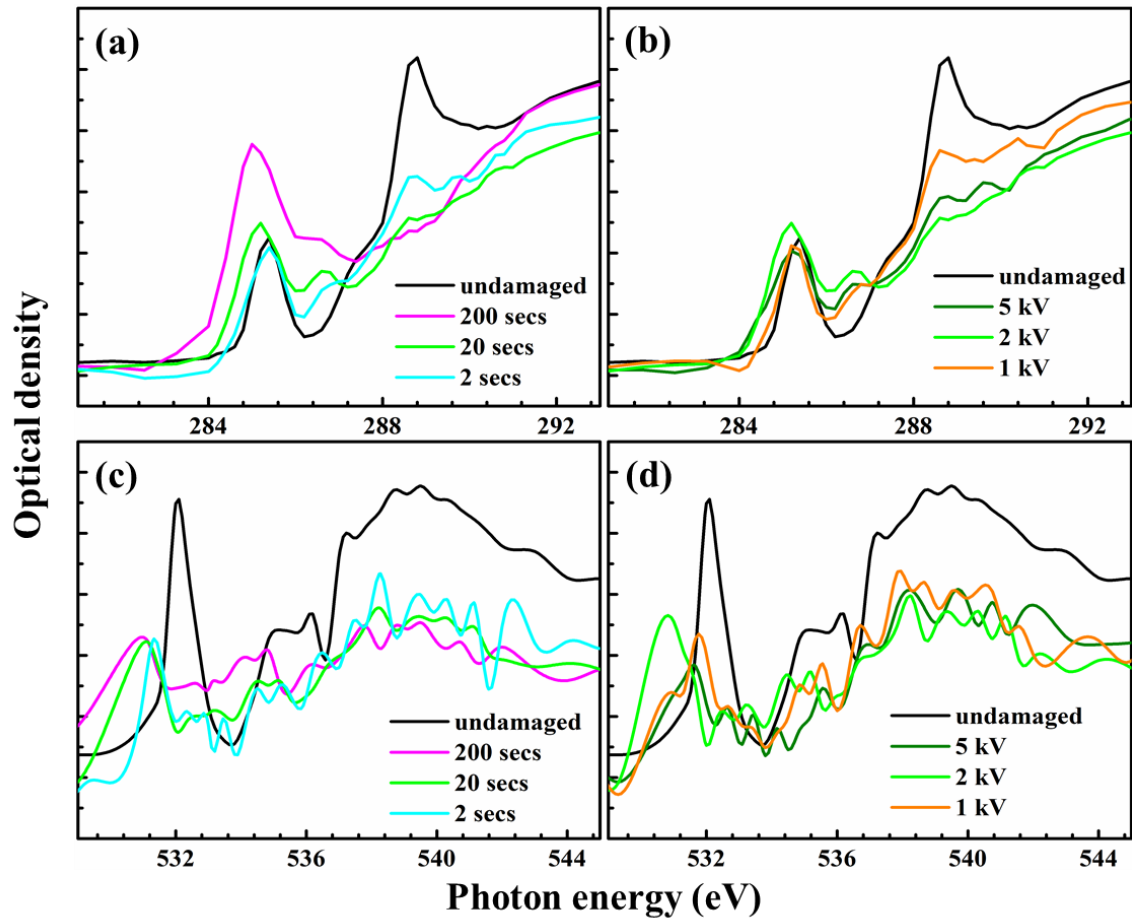
Figure S4.4 C 1s and O 1s spectra of radiation damaged resin thin film. (a) C 1s spectra for 2 kV electron beam irradiation for 2 seconds, 20 seconds and 200 seconds. (b) C 1s spectra for 20 second irradiation with voltages of 5 kV, 2 kV and 1 kV. (c) O 1s spectra for 2 kV electron beam irradiation for 2 seconds, 20 seconds and 200 seconds exposure. (d) O 1s spectra for 20 second irradiation with voltages of 1 kV, 2 kV and 5 kV.
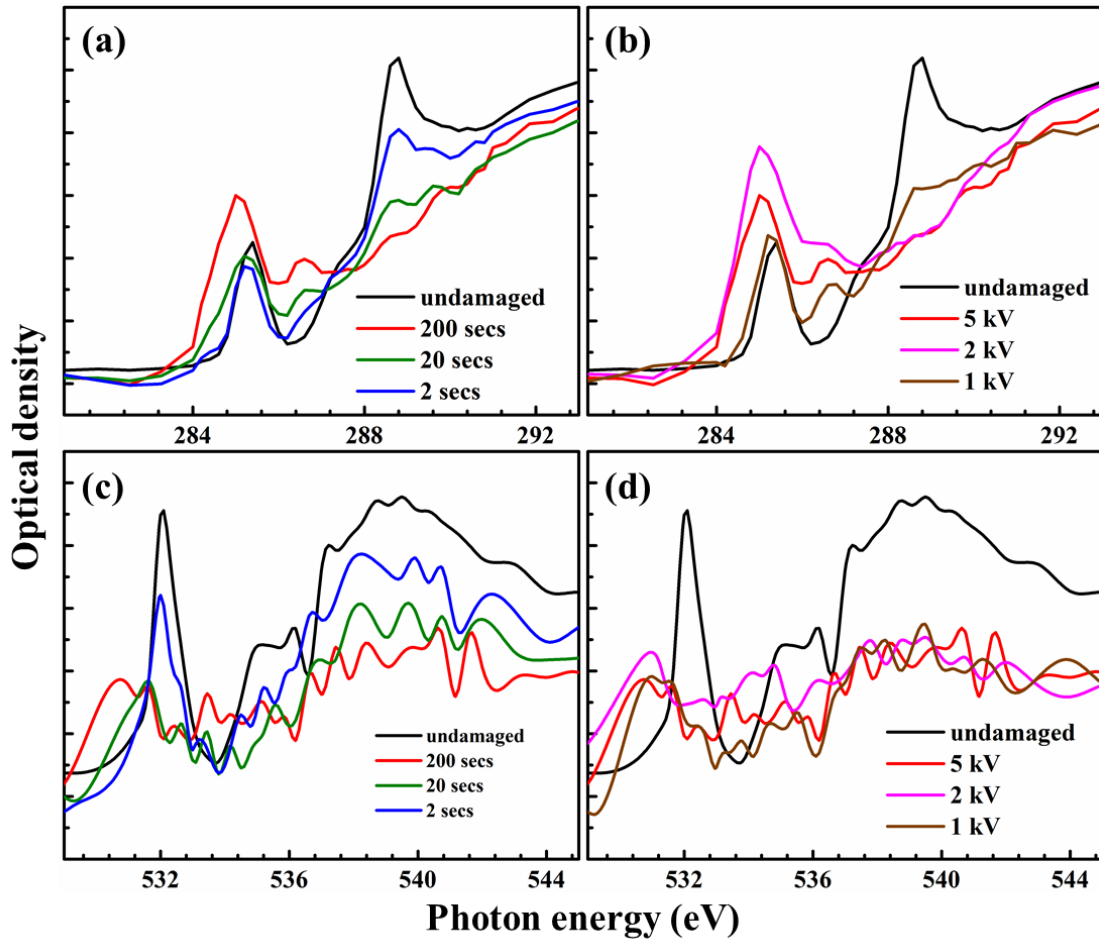
Figure S4.5 C 1s and O 1s spectra of radiation damaged resin thin film. (a) C 1s spectra for 2 kV electron beam irradiation for 2 seconds, 20 seconds and 200 seconds. (b) C 1s spectra for 20 second irradiation with voltages of 5 kV, 2 kV and 1 kV. (c) O 1s spectra for 2 kV electron beam irradiation for 2 seconds, 20 seconds and 200 seconds exposure. (d) O 1s spectra for 20 second irradiation with voltages of 1 kV, 2 kV and 5 kV.
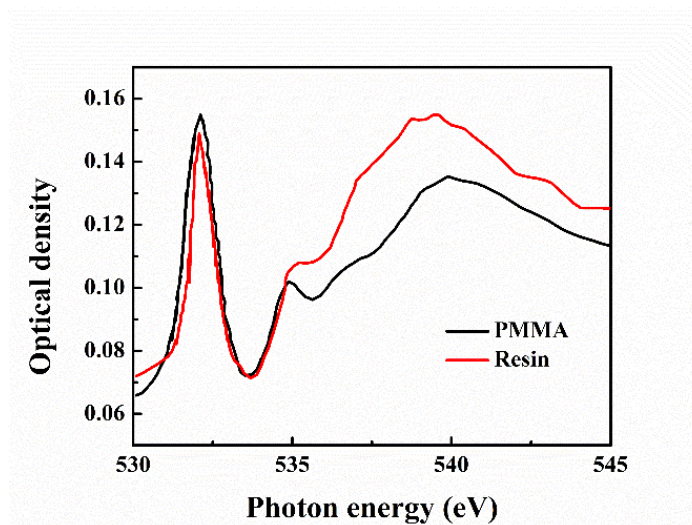
Figure S4.6 O 1s STXM spectra of PMMA (black) and resin thin film (red). The similar peaks at 532.1 eV, 535 eV, and σ^* bond condition indicate the similarity in the oxygen chemical environments of these two types of polymer.

Chapter 5 Effect of electron dose and dose rate on electron beam in polyvinylidene fluoride thin film

This chapter describes the effect of electron dose and dose rate on electron beam damage to a 250 nm polyvinylidene fluoride (PVDF) thin film. STXM analysis showed that increased carbon content and loss of fluorine are the main features of the electron damage on PVDF thin film. High electron dose at low dose rate results in more electron damage in the PVDF thin film. An earlier study of dose and dose rate dependence of electron beam damage, which gave ambiguous results, is presented in appendix I. Here more reliable results were achieved by improving the polymer film quality, using more appropriate beam parameters and pattern irradiation strategy which avoided unwanted background irradiation.

5.1 Introduction

As shown in chapter 4, beam damage depends on both the irradiated electron dose and the interaction volume distribution within the sample. Due to the unknown chemical formula of the epoxy resin, it was not possible to quantify the damage from changes in the STXM spectra. To further study the effect of other beam parameters on the electron beam damage and have a better understanding of the damage mechanism, polyvinylidene fluoride (PVDF) thin film was chosen. PVDF is a polymer with chemical formula of $[CH_2 - CF_2]_n$. The objective of this chapter is to explore effect of dose and dose rate on the electron damage on the beam-sensitive materials. In this study, 250 nm PVDF thin films were prepared by ultramicrotomy. The films were then irradiated by a 2 kV electron beam, creating a 9-pad pattern with different dose and dose rate settings. The irradiated sample was characterized by C 1s and F 1s spectroscopy measured using the STXM at CLS beamline 10ID-1. Creation and increases of signals at 285 eV (C 1s $\rightarrow \pi^*_{C=C}$) and 287 eV (C 1s $\rightarrow \pi^*_{C=O}$) and fluorine loss are the major consequences of electron beam damage to PVDF. Early work of this study can be found in appendix I, which did not provide the convincing conclusion about the dose and dose rate effect due to various reasons. This study shows that: there is strong dose dependence, which is similar at each beam current, and that, for the same

nominal dose, the exposure carried out at the **<u>lowest</u>** beam current (~dose rate) is the **<u>largest</u>**. Possible explanations for this unexpected result are presented.

5.2 Experimental setup

PVDF thin films were prepared by sectioning to 250 nm using a Leica ultramicrotome (model Leica Ultracut UCT). The sectioned films were laid on a TEM grid coated with 30 nm formvar carbon and 5nm sputter-coated gold film. The formvar supports the PVDF thin film and provides film-grid adhesion and the gold film can dissipate the accumulated charge during the SEM irradiation process. The formvar coated PVDF film was much flatter than the free standing film used in the Feb 2017 study (see appendix I). The 9-pad irradiation was carried out by python-script controlled Magellan SEM, which greatly reduced the background irradiation during the navigation process which was a major problem in the earlier study. The SEM chamber was cleaned by plasma to minimize carbon contamination. Based on the results of chapter 4, the beam voltage was fixed to 2 kV to provide greater penetration into the film than at the 1 keV voltage used in Feb 2017, and at the same time, confine the interaction volume inside the thin film sample. Each pad size is about 3μm × 2μm created with a fixed magnification of 10^5 times. The dose can be calculated by the equation $dose = \frac{Beam\ current \times Exposure\ time}{Scanning\ area}$. Since the scanned area is the same for all pads, we can calculate the exposure (which is proportional to dose) for different beam currents. Details of the beam current (dose rate) and dose design settings are shown in the table 5.1. Damage analysis was determined from the C 1s and F 1s spectra of each pad, which were acquired by Professor Hitchcock using the STXM s at beamline 10ID-1 at CLS.

Table 5.1 Beam parameters of 9-pad electron scanning area under 2 kV electron beam.

Beam current	Dose and exposure time		
	0.1 C/cm^2	0.01 C/cm^2	0.001 C/cm^2
400 pA	Area 7 (25 s)	Area 8 (2.5 s)	Area 9 (0.25 s)
200 pA	Area 4 (50 s)	Area 5 (5 s)	Area 6 (0.5 s)
50 pA	Area 1 (200 s)	Area 2 (20 s)	Area 3 (2 s)

5.3 Results and discussion

Figure 5.1 (a) shows the optical image of the irradiated pattern on PVDF thin film, annotated with the beam parameters and dose design. Figure 5.1 (b) is the damage map of the 9-pad region obtained by fitting the C 1s stack to the spectra of the off-pad (undamaged region) and pad#1 (most damaged region). Directly judging from figure 5.1, it is seen that pad#1 suffers the most severe damage. With increasing dose, the extent of damage will increase as what we expected from the study of electron beam damage to Embed resin (Ch. 4) and other such studies. The fringes in the optical image of the patterned 9 pads may be due to interference of the light rather than the electron beam damage.

(a)

(b)
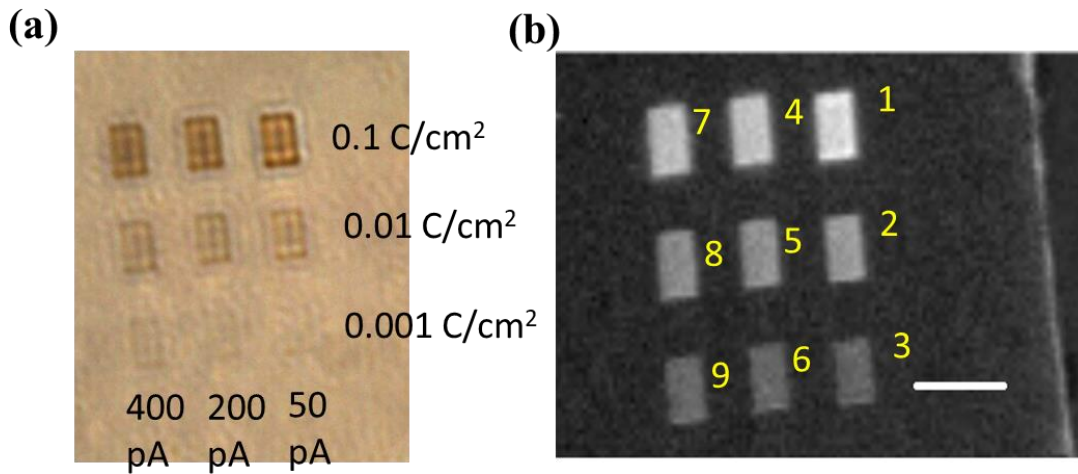
Figure 5.1 (a) Image of the 9 irradiated pads on PVDF thin film with the dose and dose rate (beam current) indicated. (b) Damage map of the 9 pads on the PVDF thin film by fitting the C 1s stack to the off-pad (undamaged region) and pad #1 (severely damaged region) spectra.

If the chemical formula and density are known then the absorption spectra measured by STXM can be used to determine the sample thickness via the formula $OD = \mu(x)\rho t$, where $\mu(x)$ is the absorption coefficient, ρ is the density, and t is the thickness of the sample. The chemical formula $(C_2H_2F_2)$ and density (1.78 g/cm^3) were used to generate the elemental response function for 1 nm thickness of the PVDF. By dividing the spectrum of the undamaged area by this elemental response per nm, the thickness of the sample was estimated to be 245±5 nm. Dividing the spectrum of the undamaged region by 250 yields the C 1s and F 1s optical density per nm (OD1) spectra presented as black curves in Fig. 5.2. The elemental response function is plotted, without any change in vertical scale as green curves in Fig. 5.2. Despite some deviation at the high energy range of the F 1s spectrum the overall match demonstrates that the thickness is indeed 250 nm.
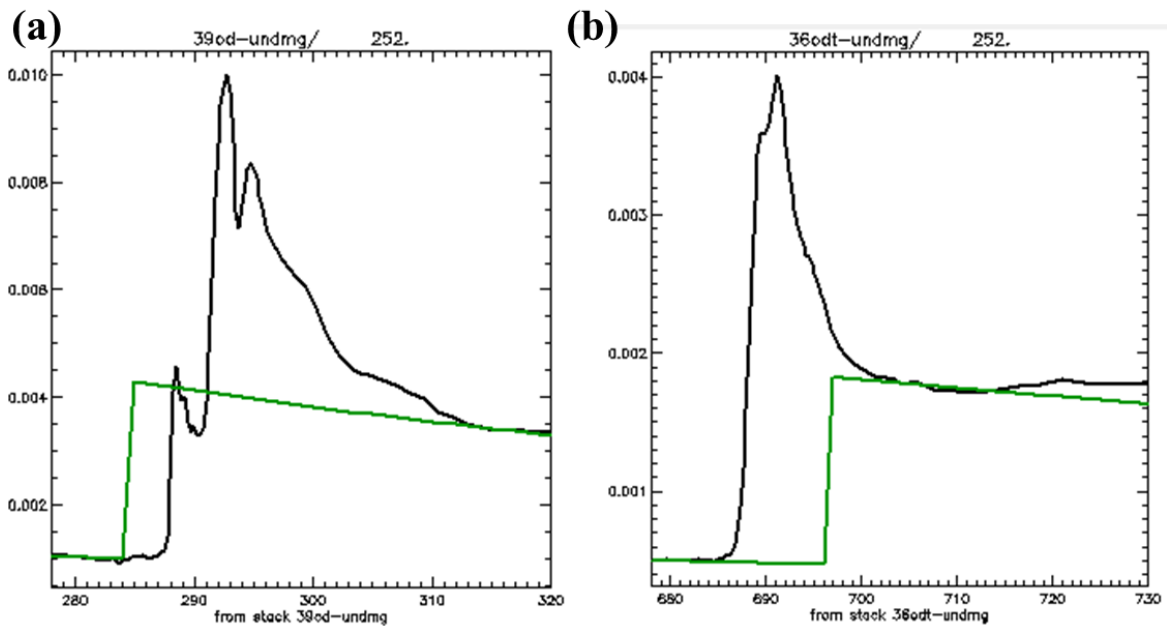
Figure 5.2 Absolute optical density per nm (OD1) spectra of PVDF. (a) C 1s. (b) F 1s. The black curve is the OD1 spectrum while the green curve is the elemental response per nm function.

As to the effect of the dose and dose rate on electron beam damage on the PVDF film, maps of the undamaged and damaged signal were generated from both C 1s and F 1s stacks by fitting each stack to the spectra of undamaged PVDF and severely damaged PVDF (pad#1). Figure 5.3 (a) and (b) shows the C 1s and F 1s stack mapping results, respectively, with blue representing the damaged region, green for the undamaged region, and red for the residual from the fitting, which was essentially featureless in each case. The mapping results are very similar to each other, indicating that the dose and dose rate dependence of electron beam damage is reflected similarly in the C 1s and F 1s spectra.
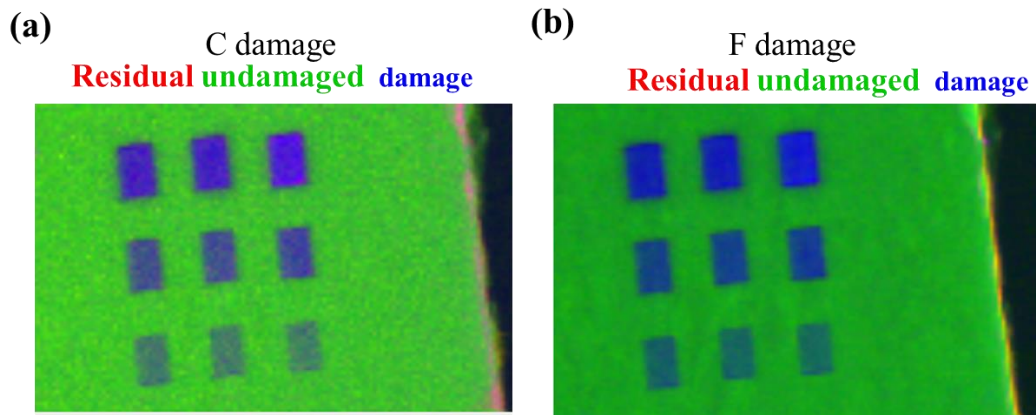
Figure 5.3 Color coded (rescaled) composites of component maps of undamaged PVDF (green), damaged PVDF (blue) and the fit residual (red) derived by singular value decomposition fitting the (a) C 1s and (b) F 1s stacks.

To study the dose and dose rate dependence of electron beam damage to PVDF, the average signal at each damaged region is averaged. These results are tabulated in Table 5.2 and plotted in Figure 5.4. The error bars are generated from the standard deviation by taking the full width at half maximum (FWHM) of the intensity histogram of each pad. With higher dose, the damage tends to increase linearly with log(dose), which matches the expectation of an exponential relationship between the dose and damage. The slopes for different dose rates (beam current) are similar which suggests the critical dose for electron beam damage to PVDF is not dependent on dose rate (beam current).

Table 5.2 Average signal at each pad in the C 1s and F 1s damage maps.

C 1s

Pad #	Current (pA)	Time (s)	exposure C/cm2	log(exp)	Avg dmg	Std dev
1	50	200.0	0.100	-1.000	1.03	0.06
2	50	20.0	0.010	-2.000	0.62	0.06
3	50	2.0	0.001	-3.000	0.31	0.05
4	200	50.0	0.100	-1.000	0.86	0.05
5	200	5.0	0.010	-2.000	0.58	0.04
6	200	0.5	0.001	-3.000	0.31	0.05
7	400	25.0	0.100	-1.000	0.82	0.07
8	400	2.5	0.010	-2.000	0.54	0.06
9	400	2.0	0.001	-3.000	0.31	0.06

F 1s

Pad #	Current (pA)	Time (s)	exposure C/cm2	log(exp)	Avg dmg	Std dev
1	50	200	0.100	-1.000	1.01	0.07
2	50	20	0.010	-2.000	0.70	0.03
3	50	2	0.001	-3.000	0.35	0.03
4	200	50	0.100	-1.000	0.89	0.04
5	200	5	0.010	-2.000	0.64	0.03
6	200	0.5	0.001	-3.000	0.37	0.03
7	400	25	0.100	-1.000	0.84	0.04
8	400	2.5	0.010	-2.000	0.59	0.04
9	400	0.25	0.001	-3.000	0.40	0.06

With higher beam current, the measured damage is less. This effect is statistically significant at the 2 higher doses, whereas the extent of damage is independent of beam current within statistical uncertainty at the 0.001 C/cm^2 exposure. If there is no significant relationship between the dose rate and the extent of damage, the lines should lay on top of each other. From the results, it is found that a beam current of 50 pA leads to more severe irradiation damage to a PVDF film than the two higher beam currents measured.
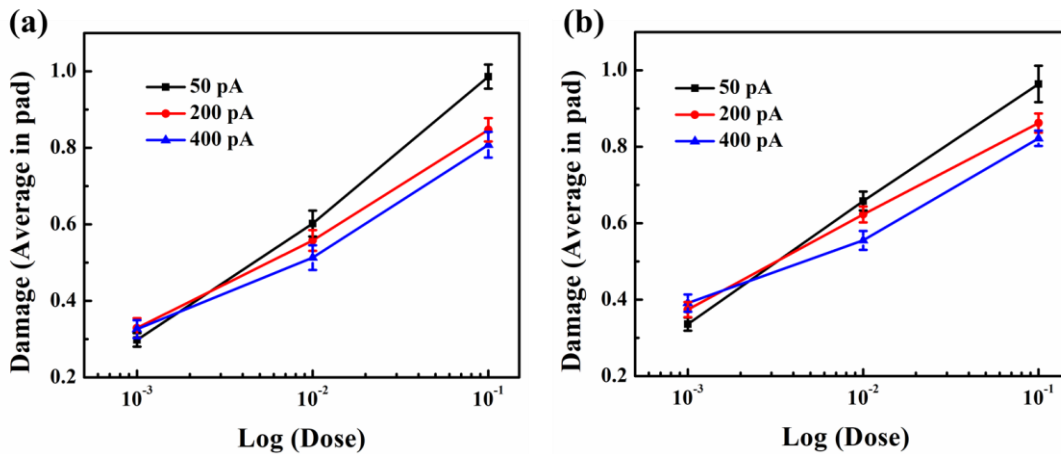
Figure 5.4 Plot of log (dose) – damage relationship based on the damage maps by the fitting from (a) C 1s and (b) F 1s stacks.

This unexpected result could be explained in a number of ways. It is possible that the **total exposure time** is more important than the dose rate with respect to accumulated damage. Figure 5.5 plots the damage To be more specific, under same dose situation, if 100 electrons are injected into the sample at one time, it can certainly cause more damage than the case of 10 electrons, which is the dose effect demonstrated by the large increase in damage with exposure that is observed. However, the extent of damage may be less than 10 times 10 electrons injection. When more electrons are injected at a given time, they may be spread out over a larger area, effectively delivering a dose lower than that computed. However, all 9 pads are very similar in size, which in inconsistent with that explanation.
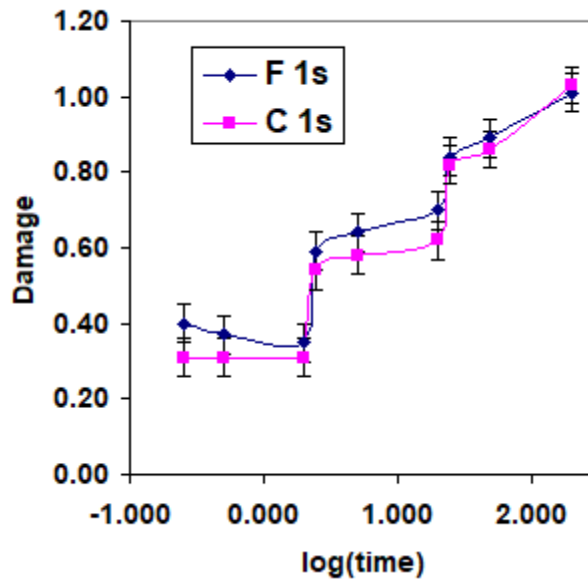
Figure 5.5 Plot of Damage as a function of exposure time for all dose rates
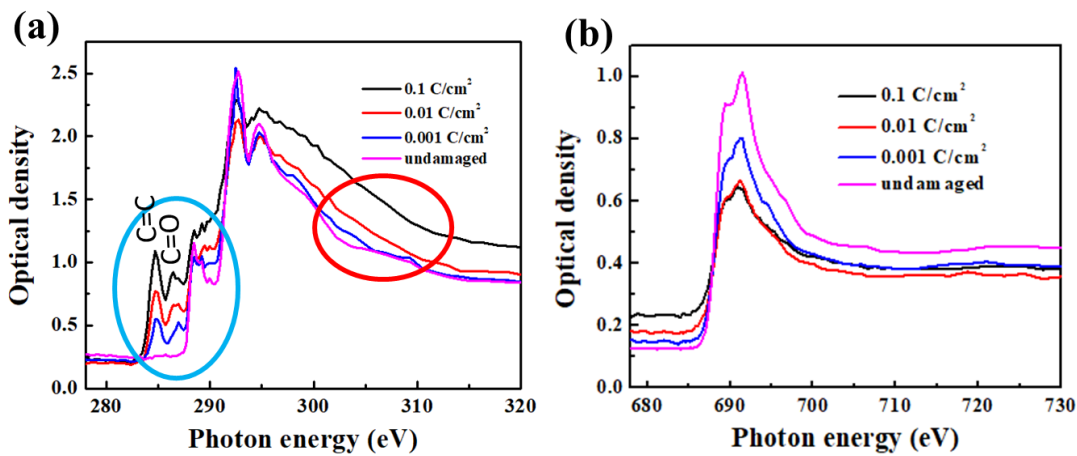
Figure 5.6 (a) C 1s spectra of pads #1,2,3 and undamaged PVDF. The blue circle highlights the main spectral changes caused by electron damage. The red circle indicates carbon contamination. (b) F 1s spectra of pads #1,2,3 and undamaged PVDF.

Since the 50 pA dose rate results in the most damage, the spectra of pads #1, #2 and #3 were chosen to study the electron damage mechanism in the PVDF thin film. The C 1s and F 1s spectra of these pads are plotted in figure 5.6 (a) and (b), in comparison to the spectra of undamaged PVDF.

The signals at 285 eV (C 1s → $\pi^*_{C=C}$) and 287 eV (C 1s → $\pi^*_{C=O}$) increase significantly with increasing dose. In addition, the carbon continuum signal increases, which may be attributed to carbon contamination as found for irradiation of the EMBED resin (chapter 4). Checking the F 1s spectrum, it can be found that with higher electron dose, the F 1s spectrum decreases, with the largest decrease occurring at the lowest dose (0.001 C/cm^2). In addition, the definition of the double peaks at 689.5 and 691.1 eV decreases indicating changes in the chemical structure of PVDF. Based on the information from these spectra the generation of C=C and C=O bonds, and the loss of F are the dominant features. A possible mechanism for the beam damage might be as follows:

$$[CF_2 - CH_2]_n + h\nu(e) \rightarrow [CF_2 = CH_2]_n + nHF$$

or $[CF_2 - CH_2]_n + H_2O + h\nu(e) \rightarrow [CO - CH_2]_n + 2nHF$
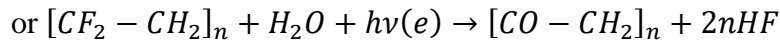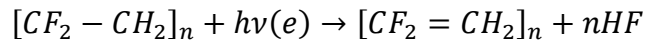
Whether HF is the final product needs to be investigated further.

5.4 Conclusion

In this study, the dose dependence of electron beam damage to PVDF was demonstrated. Surprisingly, the inverse of the expected dose rate effect was observed – larger extent of damage was observed with lower dose rates. The explanation of this observation has not yet been explained satisfactorily. It seems that exposure time rather than dose rate may play a role. The mechanism of the chemical change of the electron beam damage on the PVDF film has been explored through the spectral changes.

Chapter 6 Beam heating simulation by COMSOL

This chapter summarizes the current work and results on the beam induced heating simulation by COMSOL via the improved model. The results contain the study on the effect of time step size and dwell time on the beam induced temperature rise on a PMMA lift-out sample. All the simulations were done on the mimicking PMMA lift-out sample, with $60000\mu s$ total time. The results show that the time step size within the dwell time can give a good simulation result. By using $5\mu s$ time step size, the results show that even the total milling time is the same, the beam with less dwell time may not lead to a significantly smaller temperature rise in the sample. The results of this work can be useful for real FIB milling application for mitigating the beam induced heating problem. This simulation work can be further improved by incorporating the sputtering process in the future.

6.1 Introduction

As discussed in the previous chapters, the biggest challenge for studying beam induced heating is the difficulty in directly detecting the local temperature rise. Therefore, many researchers try to study the local temperature rise by using simulation. Although some conclusions have been drawn through the previous exploration on beam heating simulation, like using the well-designed scanning routes from Schmied's model. However, there are many problems related with the current existing heating model, such as fixed materials properties, slow simulation process, and unable to predict the milling process in real time. The model developed in this thesis tries to combine different factors together to compensate for problems encountered in previous studies.

6.2 Results and discussion

Figure 6.1 (a) – (d) show the comparison of simulation results with different time step sizes, ranging from 1 μs to 10 μs respectively. The minimum, maximum, and average temperature in the final stage within the sample are summarized in the table 6.2. As we can see, the overall shape of all four temperature rising curves are very similar to each other, which indicates that the effect of the time step size on the overall temperature might be very small. The final stage temperature

in the table also did not show much difference among. The temperature variance may be caused by the different stop time for the simulation. Since as long as the time step size is smaller than the designed dwell time, the simulation results are reliable, which allow us a faster simulation process by using a relatively large step size.

Figure 6.1 Effect of time step size on the results of COMSOL simulation of beam heating temperature evolution curve. The green, red and blue curves represent the evolution of the maximum, minimum and average temperatures respectively. Since the minimum temperature and the average temperatures are close, two lines seems to merge into a purple line. Simulation with time step size of (a) $1\ \mu s$, (b) $5\ \mu s$, (c) $8\ \mu s$, and (d) $10\ \mu s$.

Table 6.1 Summary of the lowest, maximum, and average temperature of different simulations with different step size

	Lowest temperature	Maximum temperature	Average temperature
1 μs step size	451	464	451
5 μs step size	448	456	449
8 μs step size	451	464	451
10 μs step size	448.	457	449

Very often, people use the multiple fast scanning with short dwell time to avoid the beam damage, thinking that the fast scanning may allow the heat to dissipate faster than the long-time dwelling. In our simulation, the dwell time of the ion beam can be changed easily by adjusting the parameters in the moving step function. 4 sets of different dwell time were studied, and the corresponding results are shown in figure 6.2. The minimum, maximum, and average temperature are presented in the table 6.2. As one can observe, the temperature evolution curves are also almost the same, meaning that changing the dwell time also did not change too much about the temperature of the sample as long as the total milling time is the same. The final stage simulated temperature in the table 6.2 also suggests that the dwell time has little influence on the sample average temperature at the final stage. Although the effect of dwell time has little influence on the average temperature rising, it may contribute to the difference in the maximum temperature rise as one can see in the table 6.2. With longer dwelling time, simulation shows a higher maximum temperature rise at position of the ion beam, but the difference is not that significant compared with the overall temperature rising. Although, the temperature rise from this simulation does not tell a very dramatic story like other models, the final temperature of the sample has already passed the glass transition temperature of PMMA, which indicates the softening of the polymer sample should be significant. Therefore, for a real case FIB milling of lift-out sample, the dwell time has little effect on the overall temperature rising, but people should be more careful by considering its effect on both the sputtering efficiency and materials softening due to the temperature rise.
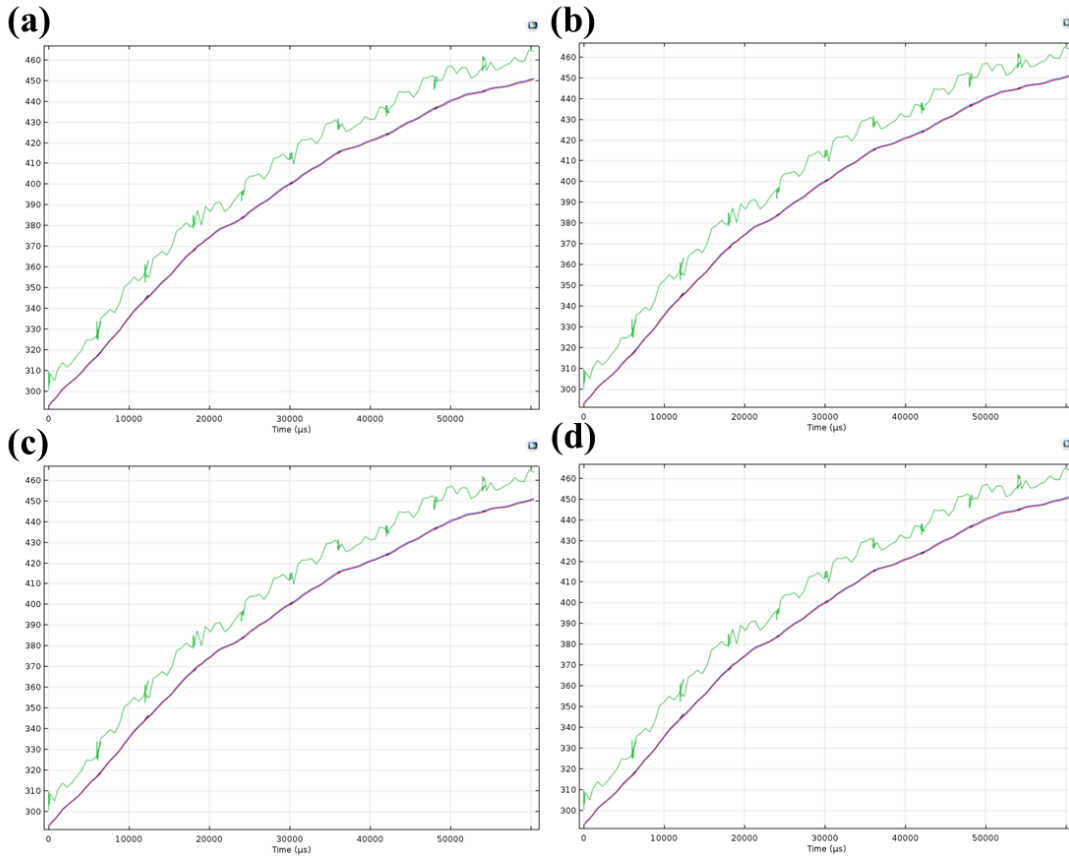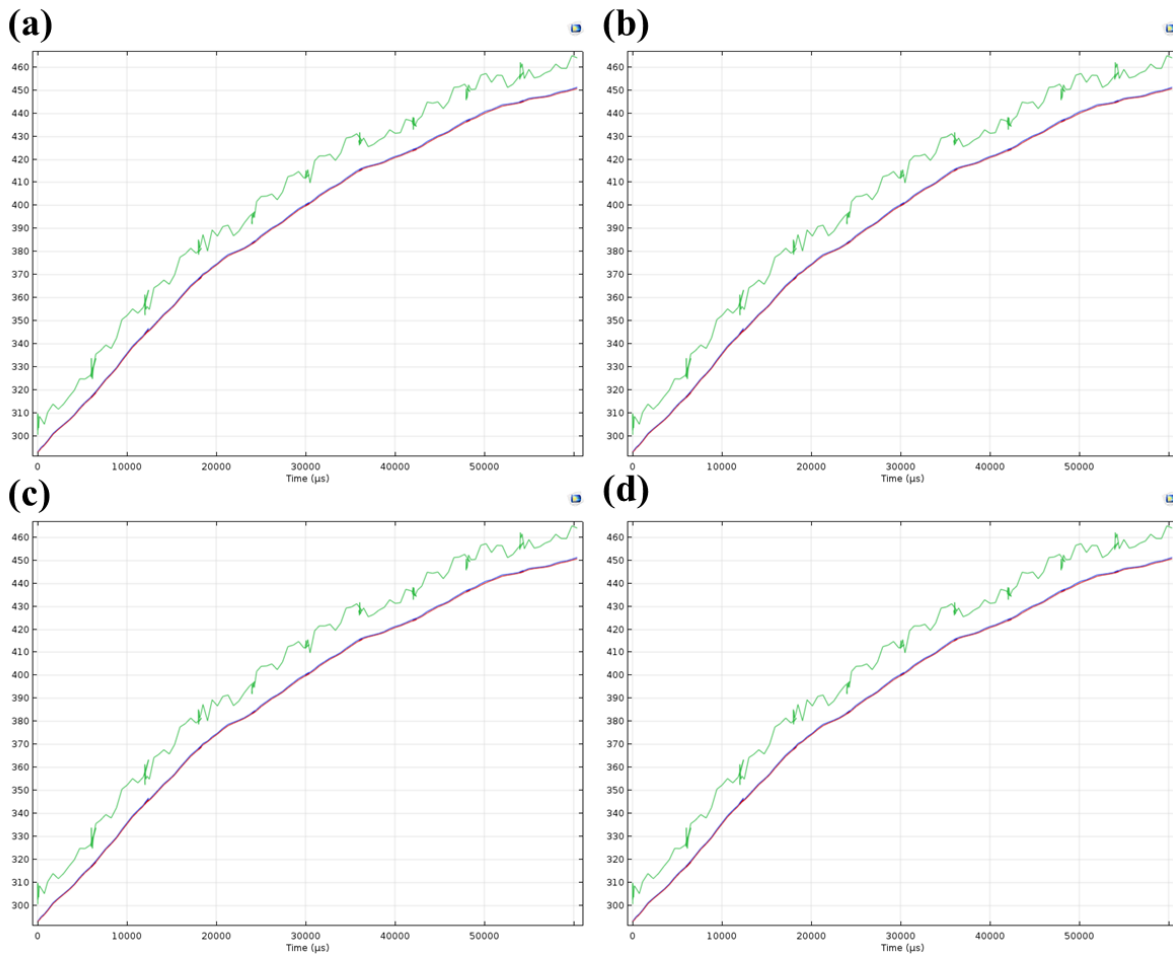
Figure 6.2 Effect of dwell time on the results of COMSOL simulation of beam heating temperature evolution curve. The green, red and blue curves represent the evolution of the maximum, minimum and average temperatures respectively. Since the minimum temperature and the average temperatures are close, two lines seems to merge into a purple line. Simulation with dwell time of (a) $5\ \mu s$, (b) $10\ \mu s$, (c) $20\ \mu s$, and (d) $50\ \mu s$.

Table 6.2 Summary of the lowest, maximum, and average temperature of different simulations with different dwell time

	Lowest temperature	Maximum temperature	Average temperature
5 μs dwell time	444.13	453.33	444.47
10 μs dwell time	448.31	455.96	448.73
20 μs dwell time	448.56	458.62	449.06
50 μs dwell time	448.31	465.87	448.93

The overall temperature rising predicted by this model is in a reasonable manner, not like thousands degree temperature rising predicted by other models.

The most possible event of the FIB milling process is ion sputtering. The current model does not have take this into consideration because there is no such obvious treatment in the COMSOL software. Since this model does not incorporate the sputtering effect in the FIB milling process, which is also the reason why we set the total milling time so small to minimize the effect of ion sputtering on our predicted temperature results, the model cannot predict very long time milling due to more significant the sputtering process in that case. Besides, the materials softening problem is not considered in this simulation due to the simplification purpose, so this model can be further improved in the future by incorporating the sputtering process and the materials softening issues into consideration.

6.3 Conclusion

The improved beam heating simulation can return the more reasonable temperature rising prediction than the previous model, with relatively mild temperature rise up to around 460K for 60000 μs milling process. The time step size with the dwelling time has little influence on the final simulated results, which allows us a more flexible choice of time step size for a faster simulation. Based on the simulation results, fast scanning route with less dwell time does not affect the temperature rising much but only on the local maximum temperature. Sputtering effect and materials softening phenomenon should be considered into the model in an indirect way for the future study and development of this beam heating model.

Chapter 7 Conclusion and future work

In this thesis, we explore the electron/ion beam damage in FIB-SEM system on soft materials by using STXM characterization and improved heat transfer simulation. Via the use of soft X-ray scanning transmission microscopy (STXM), we successfully characterized the electron beam damage on PVDF and EMbed 812 epoxy resin thin films. We study the relationship between the degree of beam damage and the beam parameters. It is found that there is a positive relationship between the degree of electron dose and dose rate with the degree of beam induced damage on the soft materials. As to the beam voltages, one need to consider the actual interaction volume of the electron beam and the thickness, since the damage mainly comes from the inelastic scattering and formation of secondary electrons. By combining the SRIM simulation and actual thermal properties, we built an improved model for assessing the ion beam induced heating problem for the lift-out samples. The output temperature of this model is more reasonable and the simulation process is much faster than the previous report heat transfer model.

The research work of this project can be further extended to carry out more STXM experiments to build a systematical study on the relationship between the beam parameters and electron beam damage on different soft materials. The beam induced heat transfer model can also be further improved by considering the sputtering process and materials softening situation during the milling simulation process.

Reference

Ali, M. Y., Hung, W., & Yongqi, F. (2010). A review of focused ion beam sputtering. *International Journal of Precision Engineering and Manufacturing, 11*(1), 157-170. doi:10.1007/s12541-010-0019-y

Alves, A., Hearne, S. M., Reichart, P., Siegele, R., Jamieson, D. N., & Johnston, P. N. (2004, Dec 13-15). *Ion beam lithography with single ions.* Paper presented at the Conference on Micro- and Nanotechnology - Materials , Processes, Packaging, and Systems II, Sydney, AUSTRALIA.

Arrua, R. D., Hitchcock, A. P., Hon, W. B., West, M., & Hilder, E. F. (2014). Characterization of Polymer Monoliths Containing Embedded Nanoparticles by Scanning Transmission X-ray Microscopy (STXM). *Analytical Chemistry, 86*(6), 2876-2881. doi:10.1021/ac403166u

Bailey, R. J., Geurts, R., Stokes, D. J., de Jong, F., & Barber, A. H. (2013). Evaluating focused ion beam induced damage in soft materials. *Micron, 50*, 51-56. doi:10.1016/j.micron.2013.04.005

Bakhsh, T. A. (2015, Feb 09-11). *Microscopic imaging of resin-bonded dentin using Cryo-FIB/TEM system.* Paper presented at the Conference on Imaging, Manipulation, and Analysis of Biomolecules, Cells, and Tissues XIII, San Francisco, CA.

Bakhsh, T. A., Sadr, A., Mandurah, M. M., Shimada, Y., Zakaria, O., & Tagami, J. (2015). In situ characterization of resin-dentin interfaces using conventional vs. cryofocused ion-beam milling. *Dental Materials, 31*(7), 833-844. doi:10.1016/j.dental.2015.04.010

Bassim, N., Scott, K., & Giannuzzi, L. A. (2014). Recent advances in focused ion beam technology and applications. *MRS Bulletin, 39*(04), 317-325. doi:10.1557/mrs.2014.52

Bassim, N. D., De Gregorio, B. T., Kilcoyne, A. L. D., Scott, K., Chou, T., Wirick, S., . . . Stroud, R. M. (2012). Minimizing damage during FIB sample preparation of soft materials. *Journal of Microscopy, 245*(3), 288-301. doi:10.1111/j.1365-2818.2011.03570.x

Belianinov, A., Burch, M. J., Kim, S., Tan, S. D., Hlawacek, G., & Ovchinnikova, O. S. (2017). Noble gas ion beams in materials science for future applications and devices. *MRS Bulletin, 42*(9), 660-666. doi:10.1557/mrs.2017.185

Briggs, D., & Hearn, M. (1986). Interaction of ion beams with polymers, with particular reference to SIMS. *Vacuum, 36*(11-12), 1005-1010.

Brostow, W., Gorman, B. P., & Olea-Mejia, O. (2007). Focused ion beam milling and scanning electron microscopy characterization of polymer plus metal hybrids. *Materials Letters, 61*(6), 1333-1336. doi:10.1016/j.matlet.2006.07.026

Burnett, T. L., Kelley, R., Winiarski, B., Contreras, L., Daly, M., Gholinia, A., . . . Withers, P. J. (2016). Large volume serial section tomography by Xe Plasma FIB dual beam microscopy. *Ultramicroscopy, 161*, 119-129. doi:10.1016/j.ultramic.2015.11.001

Carbaugh, D. J., Wright, J. T., Parthiban, R., & Rahman, F. (2016). Photolithography with polymethyl methacrylate (PMMA). *Semiconductor Science and Technology, 31*(2), 025010. doi:10.1088/0268-1242/31/2/025010

de A. Melo, L. G., Hitchcock, A. P., Berejnov, V., Susac, D., Stumper, J., & Botton, G. A. (2016). Evaluating focused ion beam and ultramicrotome sample preparation for analytical microscopies of the cathode layer of a polymer electrolyte membrane fuel cell. *Journal of Power Sources, 312*, 23-35. doi:10.1016/j.jpowsour.2016.02.019

Denisyuk, A., Hrncir, T., Obona, J. V., Sharang, Petrenec, M., & Michalicka, J. (2017). Mitigating Curtaining Artifacts During Ga FIB TEM Lamella Preparation of a 14 nm FinFET Device. *Microscopy and Microanalysis, 23*(3), 484-490. doi:10.1017/s1431927617000241

Drouin, A. R. C. D. (2011). CASINO v2.5.0. Retrieved from http://www.gel.usherbrooke.ca/casino/index.html

Du, M., & Jacobsen, C. (2018). Relative merits and limiting factors for x-ray and electron microscopy of thick, hydrated organic materials. *Ultramicroscopy, 184*, 293-309. doi:10.1016/j.ultramic.2017.10.003

Duan, H., Winston, D., Yang, J. K., Cord, B. M., Manfrinato, V. R., & Berggren, K. K. (2010). Sub-10-nm half-pitch electron-beam lithography by using poly (methyl methacrylate) as a negative resist. *Journal of Vacuum Science & Technology B, Nanotechnology and Microelectronics: Materials, Processing, Measurement, and Phenomena, 28*(6), C6C58-C56C62.

Edwards, H. K., Coe, S. C., Fay, M. W., Scotchford, C. A., Grant, D. M., & Brown, P. D. (2007, Sep 03-07). *Site-speciric, cross-sectional imaging of biomaterials and the cell/biomaterial interface using focused ion beam/scanning electron microscopy.* Paper presented at the Electron Microscopy and Analysis Group Conference, Glasgow Caledonian Univ, Glasgow, SCOTLAND.

Egerton, R. (2012). The importance of dose-limited resolution.

Egerton, R. F. (2011). *Electron energy-loss spectroscopy in the electron microscope*: Springer Science & Business Media.

Egerton, R. F. (2013). Control of radiation damage in the TEM. *Ultramicroscopy, 127*, 100-108. doi:10.1016/j.ultramic.2012.07.006

Egerton, R. F., Lazar, S., & Libera, M. (2012). Delocalized radiation damage in polymers. *Micron, 43*(1), 2-7. doi:10.1016/j.micron.2011.05.007

Egerton, R. F., Li, P., & Malac, M. (2004). Radiation damage in the TEM and SEM. *Micron, 35*(6), 399-409. doi:10.1016/j.micron.2004.02.003

Egerton, R. F., McLeod, R., Wang, F., & Malac, M. (2010). Basic questions related to electron-induced sputtering in the TEM. *Ultramicroscopy, 110*(8), 991-997. doi:10.1016/j.ultramic.2009.11.003

Egerton, R. F., & Rauf, I. (1999). Dose-rate dependence of electron-induced mass loss from organic specimens. *Ultramicroscopy, 80*(4), 247-254. doi:10.1016/s0304-3991(99)00114-x

Egerton, R. F., Wang, F., & Crozier, P. A. (2006). Beam-induced damage to thin specimens in an intense electron probe. *Microscopy and Microanalysis, 12*(1), 65-71. doi:10.1017/s1431927606060065

Ektessabi, A. M., & Sano, T. (2000). Sputtering and thermal effect during ion microbeam patterning of polymeric films. *Review of Scientific Instruments, 71*(2), 1012-1015. doi:10.1063/1.1150375

EMSCompany. EMbed 812 Kit technical data sheet. Retrieved from https://www.emsdiasum.com/microscopy/technical/datasheet/14120.aspx

EMSCompany. Poly(vinylidene fluoride) dataset. Retrieved from http://www.sigmaaldrich.com/catalog/product/aldrich/427152?lang=en&region=CA

Estivill, R., Audoit, G., Barnes, J. P., Grenier, A., & Blavette, D. (2016). Preparation and Analysis of Atom Probe Tips by Xenon Focused Ion Beam Milling. *Microscopy and Microanalysis, 22*(3), 576-582. doi:10.1017/s1431927616000581

Giannuzzi, L. A. (2004). *Introduction to focused ion beams: instrumentation, theory, techniques and practice*: Springer Science & Business Media.

Giannuzzi, L. A., & Stevie, F. A. (1999). A review of focused ion beam milling techniques for TEM specimen preparation. *Micron, 30*(3), 197-204. doi:10.1016/s0968-4328(99)00005-0

Goldstein, J. I., Newbury, D. E., Michael, J. R., Ritchie, N. W., Scott, J. H. J., & Joy, D. C. (2017). *Scanning electron microscopy and X-ray microanalysis*: Springer.

Hitchcock, A. P. (2019). aXis 2000 - Analysis of X-ray Images and Spectra (Version 16 Feb 2019

). Retrieved from http://unicorn.mcmaster.ca/aXis2000.html

Hitchcock, A. P., & Toney, M. F. (2014). Spectromicroscopy and coherent diffraction imaging: focus on energy materials applications. *Journal of Synchrotron Radiation, 21*, 1019-1030. doi:10.1107/s1600577514013046

Holzer, L., & Cantoni, M. (2012). Review of FIB-tomography. *Nanofabrication Using Focused Ion and Electron Beams: Principles and Applications, 559201222*, 410-435.

Ishitani, T., & Kaga, H. (1995). CALCULATION OF LOCAL TEMPERATURE RISE IN FOCUSED-ION-BEAM SAMPLE PREPARATION. *Journal of Electron Microscopy, 44*(5), 331-336.

Jacobsen, C., Wirick, S., Flynn, G., & Zimba, C. (2000). Soft X-ray spectroscopy from image sequences with sub-100 nm spatial resolution. *Journal of Microscopy-Oxford, 197*, 173-184.

Jiang, N. (2013). Damage mechanisms in electron microscopy of insulating materials. *Journal of Physics D-Applied Physics, 46*(30), 10. doi:10.1088/0022-3727/46/30/305502

Jiang, N., & Spence, J. C. H. (2012). On the dose-rate threshold of beam damage in TEM. *Ultramicroscopy, 113*, 77-82. doi:10.1016/j.ultramic.2011.11.016

Joy, D. C., & Joy, C. S. (1995). Dynamic Charging in the Low Voltage SEM. *Microscopy and Microanalysis, 1*(3), 109-112. doi:10.1017/S1431927695111095

Joy, D. C., & Joy, C. S. (1998). Study of the dependence of E2 energies on sample chemistry. *Microscopy and Microanalysis, 4*(5), 475-480. doi:10.1017/s1431927698980448

Kang, G.-d., & Cao, Y.-m. (2014). Application and modification of poly (vinylidene fluoride)(PVDF) membranes–a review. *Journal of Membrane Science, 463*, 145-165.

Kim, S., Park, M. J., Balsara, N. P., Liu, G., & Minor, A. M. (2011). Minimization of focused ion beam damage in nanostructured polymer thin films. *Ultramicroscopy, 111*(3), 191-199. doi:10.1016/j.ultramic.2010.11.027

Kizilyaprak, C., Daraspe, J., & Humbel, B. M. (2014). Focused ion beam scanning electron microscopy in biology. *Journal of Microscopy, 254*(3), 109-114. doi:10.1111/jmi.12127

Kochumalayil, J. J., Meiser, A., Soldera, F., & Possart, W. (2009). Focused ion beam irradiation - morphological and chemical evolution in PMMA. *Surface and Interface Analysis, 41*(5), 412-420. doi:10.1002/sia.3042

Koval, Y., Borzenko, T., & Dubonos, S. (2003). Use of polymethylmethacrylate for pattern transfer by ion beam etching: Improvement of etching homogeneity and patterning quality. *Journal of Vacuum Science & Technology B, 21*(5), 2217-2219. doi:10.1116/1.1612934

Laffont, L., Monthioux, M., Serin, V., Mathur, R., Guimon, C., & Guimon, M. (2004). An EELS study of the structural and chemical transformation of PAN polymer to solid carbon. *Carbon, 42*(12-13), 2485-2494.

Lehnert, T., Lehtinen, O., Algara-Siller, G., & Kaiser, U. (2017). Electron radiation damage mechanisms in 2D MoSe2. *Applied Physics Letters, 110*(3), 4. doi:10.1063/1.4973809

Leontowich, A. F. G., & Hitchcock, A. P. (2012). Secondary electron deposition mechanism of carbon contamination. *Journal of Vacuum Science & Technology B, 30*(3). doi:10.1116/1.3698602

Leontowich, A. F. G., Hitchcock, A. P., & Egerton, R. F. (2016). Radiation damage yields across the carbon 1s excitation edge. *Journal of Electron Spectroscopy and Related Phenomena, 206*, 58-64. doi:10.1016/j.elspec.2015.11.010

Leontowich, A. F. G., Hitchcock, A. P., Tyliszczak, T., Weigand, M., Wang, J., & Karunakaran, C. (2012). Accurate dosimetry in scanning transmission X-ray microscopes via the cross-linking threshold dose of poly(methyl methacrylate). *Journal of Synchrotron Radiation, 19*, 976-987. doi:10.1107/s0909049512034486

Li, P., & Egerton, R. F. (2003). Electron irradiation damage to aromatic compounds. *Microscopy and Microanalysis, 9*(S02), 986-987. doi:10.1017/S1431927603444930

Li, X., Sun, M., Shan, C., Chen, Q., & Wei, X. (2018). Mechanical properties of 2D materials studied by in situ microscopy techniques. *Advanced Materials Interfaces, 5*(5), 1701246.

Li, X., Sun, M., Wei, X., Shan, C., & Chen, Q. (2018). 1D Piezoelectric Material Based Nanogenerators: Methods, Materials and Property Optimization. *Nanomaterials, 8*(4), 188.

Longieras, N., Sebban, M., Palmas, P., Rivaton, A., & Gardette, J. L. (2007). Degradation of epoxy resins under high energy electron beam irradiation: Radio-oxidation. *Polymer Degradation and Stability, 92*(12), 2190-2197. doi:10.1016/j.polymdegradstab.2007.01.035

Melo, L. G., Hitchcock, A. P., Jankovic, J., Stumper, J., Susac, D., & Berejnov, V. (2017). Quantitative mapping of ionomer in catalyst layers by electron and x-ray spectromicroscopy. *ECS Transactions, 80*(8), 275-282.

Nagai, N., Matsunobe, T., & Imai, T. (2005). Infrared analysis of depth profiles in UV-photochemical degradation of polymers. *Polymer Degradation and Stability, 88*(2), 224-233.

Orloff, J. (1993). HIGH-RESOLUTION FOCUSED ION-BEAMS. *Review of Scientific Instruments, 64*(5), 1105-1130. doi:10.1063/1.1144104

Oshima, A., Okubo, S., Oyama, T. G., Washio, M., & Tagawa, S. (2012). Nano- and micro-fabrications of polystyrene having atactic and syndiotactic structures using focused ion beams lithography. *Radiation Physics and Chemistry, 81*(5), 584-588. doi:10.1016/j.radphyschem.2011.12.039

Porter, C. E., & Blum, F. D. (2000). Thermal characterization of PMMA thin films using modulated differential scanning calorimetry. *Macromolecules, 33*(19), 7016-7020.

Rothmann, M. U., Li, W., Zhu, Y., Liu, A., Ku, Z. L., Bach, U., . . . Cheng, Y. B. (2018). Structural and Chemical Changes to CH3NH3PbI3 Induced by Electron and Gallium Ion Beams. *Advanced Materials, 30*(25), 7. doi:10.1002/adma.201800629

Rykaczewski, K., Mieritz, D. G., Liu, M., Ma, Y., Iezzi, E. B., Sun, X., . . . Wang, R. Y. (2016). Far-reaching geometrical artefacts due to thermal decomposition of polymeric coatings around focused ion beam milled pigment particles. *Journal of Microscopy, 262*(3), 316-325. doi:10.1111/jmi.12367

Santoro, F., Neumann, E., Panaitov, G., & Offenhausser, A. (2014). FIB section of cell-electrode interface: An approach for reducing curtaining effects. *Microelectronic Engineering, 124*, 17-21. doi:10.1016/j.mee.2014.04.021

Sato, Y., Yamaguchi, D., Katoh, T., Ikeda, S., Aoki, Y., Oshima, A., . . . Washio, M. (2003). Surface modification of polytetrafluoroethylene by synchrotron radiation. *Nuclear Instruments & Methods in Physics Research Section B-Beam Interactions with Materials and Atoms, 208*, 231-235. doi:10.1016/s0168-583x(03)01108-x

Sawyer, L., Grubb, D. T., & Meyers, G. F. (2008). *Polymer microscopy*: Springer Science & Business Media.

Schmied, R., Froch, J. E., Orthacker, A., Hobisch, J., Trimmel, G., & Plank, H. (2014). A combined approach to predict spatial temperature evolution and its consequences during FIB processing of soft matter. *Phys Chem Chem Phys, 16*(13), 6153-6158. doi:10.1039/c3cp55308f

Schwarz, S. M., Kempshall, B. W., Giannuzzi, L. A., & McCartney, M. R. (2003). Avoiding the Curtaining Effect: Backside Milling by FIB INLO. *Microscopy and Microanalysis, 9*(S02), 116-117. doi:10.1017/S1431927603441044

Scott, K. (2011). 3D elemental and structural analysis of biological specimens using electrons and ions. *Journal of Microscopy, 242*(1), 86-93. doi:10.1111/j.1365-2818.2010.03444.x

Sigma-Aldrich-Company. Epoxy embedding medium. Retrieved from https://www.sigmaaldrich.com

Smith, W. F., & Hashemi, J. (2006). *Foundations of materials science and engineering*: Mcgraw-Hill Publishing.

Stöhr, J. (2013). *NEXAFS spectroscopy* (Vol. 25): Springer Science & Business Media.

Sun, W., Chen, Y. W., Zhou, L., & He, X. H. (2006). Preparing polymer brushes on poly(vinylidene fluoride) films by free radical polymerization. *Journal of Applied Polymer Science, 101*(2), 857-862. doi:10.1002/app.23476

Szenes, G., Havancsak, K., Skuratov, V., Hanak, P., Zsoldos, L., & Ungar, T. (2000). Application of the thermal spike model to latent tracks induced in polymers. *Nuclear Instruments & Methods in*

Physics Research Section B-Beam Interactions with Materials and Atoms, 166, 933-937. doi:10.1016/s0168-583x(99)00733-8

Tapia, J. C., Kasthuri, N., Hayworth, K. J., Schalek, R., Lichtman, J. W., Smith, S. J., & Buchanan, J. (2012). High-contrast en bloc staining of neuronal tissue for field emission scanning electron microscopy. *Nature Protocols, 7*(2), 193-206. doi:10.1038/nprot.2011.439

Titze, B., & Genoud, C. (2016). Volume scanning electron microscopy for imaging biological ultrastructure. *Biology of the Cell, 108*(11), 307-323. doi:10.1111/boc.201600024

Urquhart, S. G., & Ade, H. (2002). Trends in the carbonyl core (C 1s, O 1s) -> pi*c=o transition in the near-edge X-ray absorption fine structure spectra of organic molecules. *Journal of Physical Chemistry B, 106*(34), 8531-8538. doi:10.1021/jp0255379

Utke, I., Hoffmann, P., & Melngailis, J. (2008). Gas-assisted focused electron beam and ion beam processing and fabrication. *Journal of Vacuum Science & Technology B, 26*(4), 1197-1276. doi:10.1116/1.2955728

Varlot, K., Martin, J., Gonbeau, D., & Quet, C. (1999). Chemical bonding analysis of electron-sensitive polymers by EELS. *Polymer, 40*(20), 5691-5697.

Varlot, K., Martin, J., & Quet, C. (2001). EELS analysis of PMMA at high spatial resolution. *Micron, 32*(4), 371-378.

Vilar, M. R., Schott, M., Pireaux, J., Grégoire, C., Thiry, P., Caudano, R., . . . Da Silva, J. L. (1987). Study of polymer film surfaces by EELS using selectively deuterated polystyrene. *Surface Science, 189*, 927-934.

Vineyard, G. H. (1976). THERMAL SPIKES AND ACTIVATED PROCESSES. *Radiation Effects and Defects in Solids, 29*(4), 245-248. doi:10.1080/00337577608233050

Wang, J., Botton, G. A., West, M. M., & Hitchcock, A. P. (2009). Quantitative evaluation of radiation damage to polyethylene terephthalate by soft X-rays and high-energy electrons. *The Journal of Physical Chemistry B, 113*(7), 1869-1876.

Wang, J., Button, G. A., West, M. M., & Hitchcock, A. P. (2009). Quantitative Evaluation of Radiation Damage to Polyethylene Terephthalate by Soft X-rays and High-energy Electrons. *Journal of Physical Chemistry B, 113*(7), 1869-1876. doi:10.1021/jp808289e

Wang, J., Morin, C., Li, L., Hitchcock, A. P., Scholl, A., & Doran, A. (2009). Radiation damage in soft X-ray microscopy. *Journal of Electron Spectroscopy and Related Phenomena, 170*(1-3), 25-36. doi:10.1016/j.elspec.2008.01.002

Williams, D. B., & Carter, C. B. (1996). The transmission electron microscope. In *Transmission electron microscopy* (pp. 3-17): Springer.

Willmott, P. (2011). *An introduction to synchrotron radiation: techniques and applications*: John Wiley & Sons.

Wolff, A., Klingner, N., Thompson, W., Zhou, Y., Lin, J., Peng, Y. Y., . . . Xiao, Y. (2018). Modelling of focused ion beam induced increases in sample temperature: a case study of heat damage in biological samples. *Journal of Microscopy, 272*(1), 47-59. doi:10.1111/jmi.12731

Wu, J., Zhu, X., Shapiro, D. A., Lee, J. R., Van Buuren, T., Biener, M. M., . . . Hitchcock, A. P. (2018). Four-Dimensional Imaging of ZnO-Coated Alumina Aerogels by Scanning Transmission X-ray Microscopy and Ptychographic Tomography. *The Journal of Physical Chemistry C, 122*(44), 25374-25385.

Xu, Y. M., Shi, L. A., Zhang, X. T., Wong, K. W., & Li, Q. (2011). The electron beam irradiation damage on nanomaterials synthesized by hydrothermal and thermal evaporation methods-An example of ZnS nanostructures. *Micron, 42*(3), 290-298. doi:10.1016/j.micron.2010.09.009

Zeng, P., Inkson, B. J., Rainforth, W. M., & Stewart, T. (2007, Sep 03-07). *3D Surface Reconstruction and FIB Microscopy of Worn Alumina Hip Prostheses.* Paper presented at the Electron Microscopy and Analysis Group Conference, Glasgow Caledonian Univ, Glasgow, SCOTLAND.

Zhou, W., Zuo, J., & Ren, W. (2012). Thermal conductivity and dielectric properties of Al/PVDF composites. *Composites Part A: Applied Science and Manufacturing, 43*(4), 658-664.

Ziegler, J. F., Ziegler, M. D., & Biersack, J. P. (2010). SRIM - The stopping and range of ions in matter (2010). *Nuclear Instruments & Methods in Physics Research Section B-Beam Interactions with Materials and Atoms, 268*(11-12), 1818-1823. doi:10.1016/j.nimb.2010.02.091

Appendix I Early work on the effect of electron dose and dose rate on electron beam in polyvinylidene fluoride thin film

This appendix chapter describes our first trial on studying the effect of electron dose and dose rate on the electron beam damage in the 250 nm PVDF thin film by STXM. The results of this experiment demonstrated that the STXM is a powerful tool for beam damage study. Due to the thick sample, unintended irradiation of the navigation process, and low beam voltage chosen, the analysis of this set of data cannot provide a convincing conclusion about the effect of electron dose and dose rate. Part of the content of this chapter has been presented as a poster at the 11th Annual FIB SEM workshop at McMaster University, May 2018

Introduction

Chapter 4 presented the effect of beam voltage and electron dose on the damage in the resin film. It shows that with more electron dose, the induced radiolysis is more severe. However, since the exact chemical formula is unknown for the EMbed 812 epoxy resin, we cannot accurately point out the exact chemical change during the radiolysis. To further study of the electron dose, we choose a PVDF thin film as our sample since the chemical formula is well-known, with a formula of $[CH_2-CF_2]_n$. The objective of this chapter is to further explore the beam parameter – degree of damage on soft materials, by studying the effect of electron dose rate. In this study, the ultramicrotomy-prepared PVDF thin films were irradiated under 1 kV beam voltage, with different beam current and exposure time. The irradiated samples were then characterized by the STXM-NEXAFS to acquire C 1s and F 1s spectrum of the samples. The results of this chapter suggested that under same dose conditions, the higher dose rate can lead to more damage.

Experimental setup

The experimental procedure is similar to the one in chapter 4, except for the irradiation conditions. 250 nm PVDF thin films were prepared by ultramicrotomy and laid on the bare Cu

TEM grid. The electron pattern irradiation was done by the FEI Magellan 400 SEM. The chamber of SEM was cleaned by plasma before the irradiation to minimize the chance of carbon contamination. The accelerating voltage was fixed to be 1 kV. Each irradiated pad is about 3μm×2μm under magnification of 10^5 X. A 3×3 pads pattern was created by SEM under the control of Python script. The irradiated dose on the sample thin film is calculated by the equation: $Exposure = \dfrac{Beam\ current \times Exposure\ time}{Scanning\ area}$. Since we know the beam current we used, which can serve as the dose rate indicator, and the scanning area is basically fixed due to the fixed magnification, we can calculate the exposure time. Besides, we originally wanted to drill a hole for I_0 by using high beam current and long exposure time, but it did not succeed, instead creating an area with significant damage near the pads on the PVDF thin film. The irradiation conditions were summarized in the table below. Since the sample was not flat due to the free stand wrinkling, the pads on the wrinkled parts or above Cu grid frame were not studied. The 10ID1 beamline at CLS was used to characterize the irradiated PVDF sample by acquiring the C 1s and F 1s spectra of the sample. The chemical changes can be observed in both spectra.

Table 1 Beam parameters setting for pattern irradiation

	Dose and exposure time		
Beam current	0.1 C/cm^2	0.01 C/cm^2	0.001 C/cm^2
400 pA	Area 3 (22.55s)	Area 6 (2.25s)	N.A.
200 pA	Area 2 (45s)	Area 5 (4.5s)	N.A.
50 pA	Area 1 (200s)	Area 4 (20s)	N.A.

Results and discussion

The irradiated area can be easily identified by optical microscope, as shown in figure 2 (a), indicating the significance of the electron damage on the PVDF thin film. Since we did not drill through the PVDF film, we truncate the severely damaged region during our analysis. During the analysis process, we compensate the sample thickness variation by normalizing the stack. Figure 5.1 (b) shows the color map of the degree of damage with the green color for undamaged part and red color for the damaged one. The damage region near the pad 3 and 6 was caused by the beam spreading of the severely damage zone near pad 6.
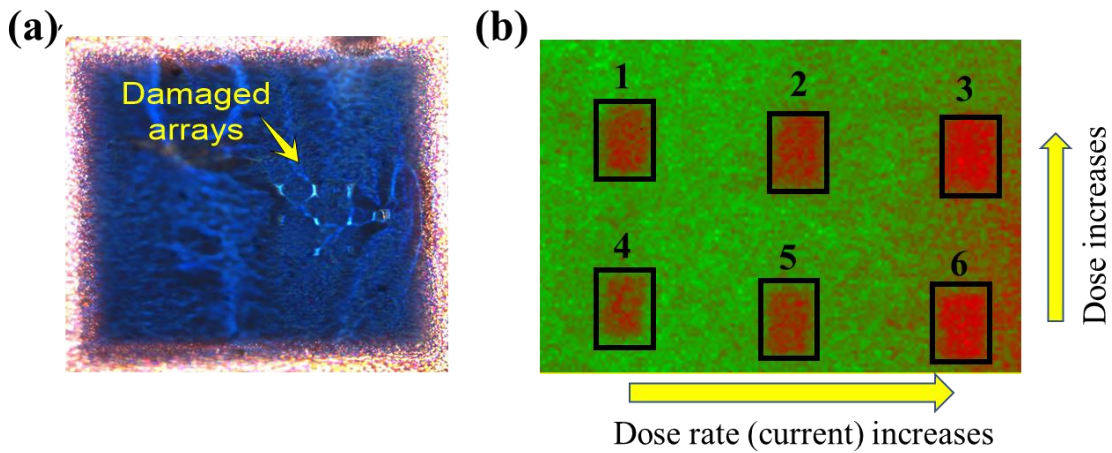

Figure 1 (a) Optical image of electron irradiated arrays on PVDF thin film. (b) Color map of the damage distribution on the 6-pad irradiated region obtained from the C 1s spectrum. The damage distribution color map was obtained by using the fitting function in aXis2000 software.
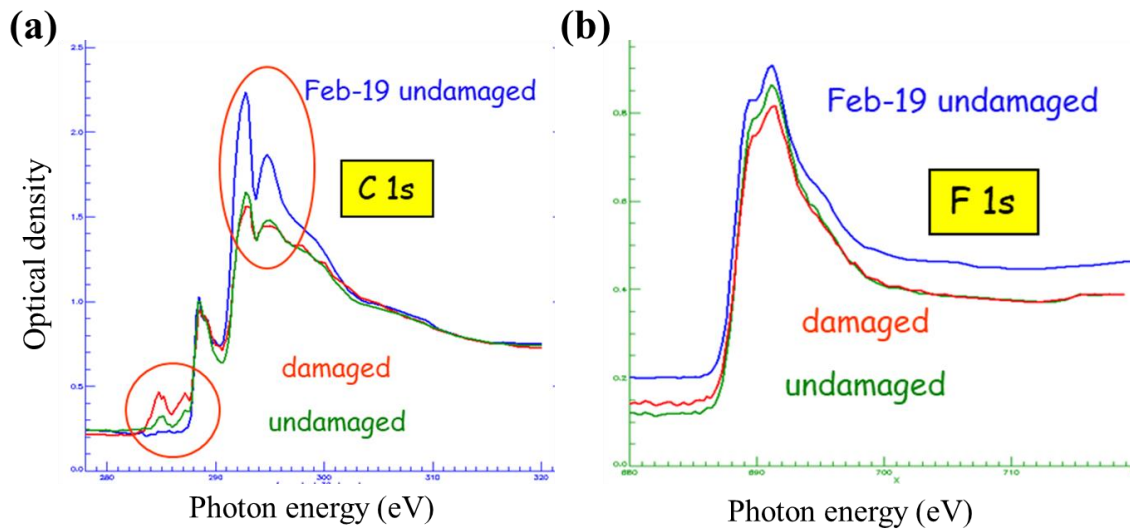
Figure 2 (a) C1s spectrum and (b) F1s spectrum comparisons of damaged (red), undamaged (green) region on Feb-2018 samples and undamaged region on Feb-2019 sample (blue)

Before we used the computer to run the irradiation pattern script, we needed to manually locate and move to the desired region which has been identified by the optical microscope before loading the sample into SEM. This searching process may bring the unwanted electron irradiation, which we denoted as background irradiation. As shown in Figure 5.2, we can found that there are peaks rising at 295 and 297 eV for the 2018 sample, which correspond to the forming of C=C and C=O respectively, indicating the chemical change induced on the PVDF films. The 292 and 296 eV peak drop can be attributed to the carbon signal saturation in the 2018 sample. As we can see in the figure 2(b), F loss is less significant than the rising of C=C and C=O peaks which may be attributed to small interaction volume of low electron energy in thick sample. Therefore, the background irradiation due to the navigation process can introduce negligible damage on PVDF which was avoided in the following studies by using the python script to control the operation of Magellan SEM.
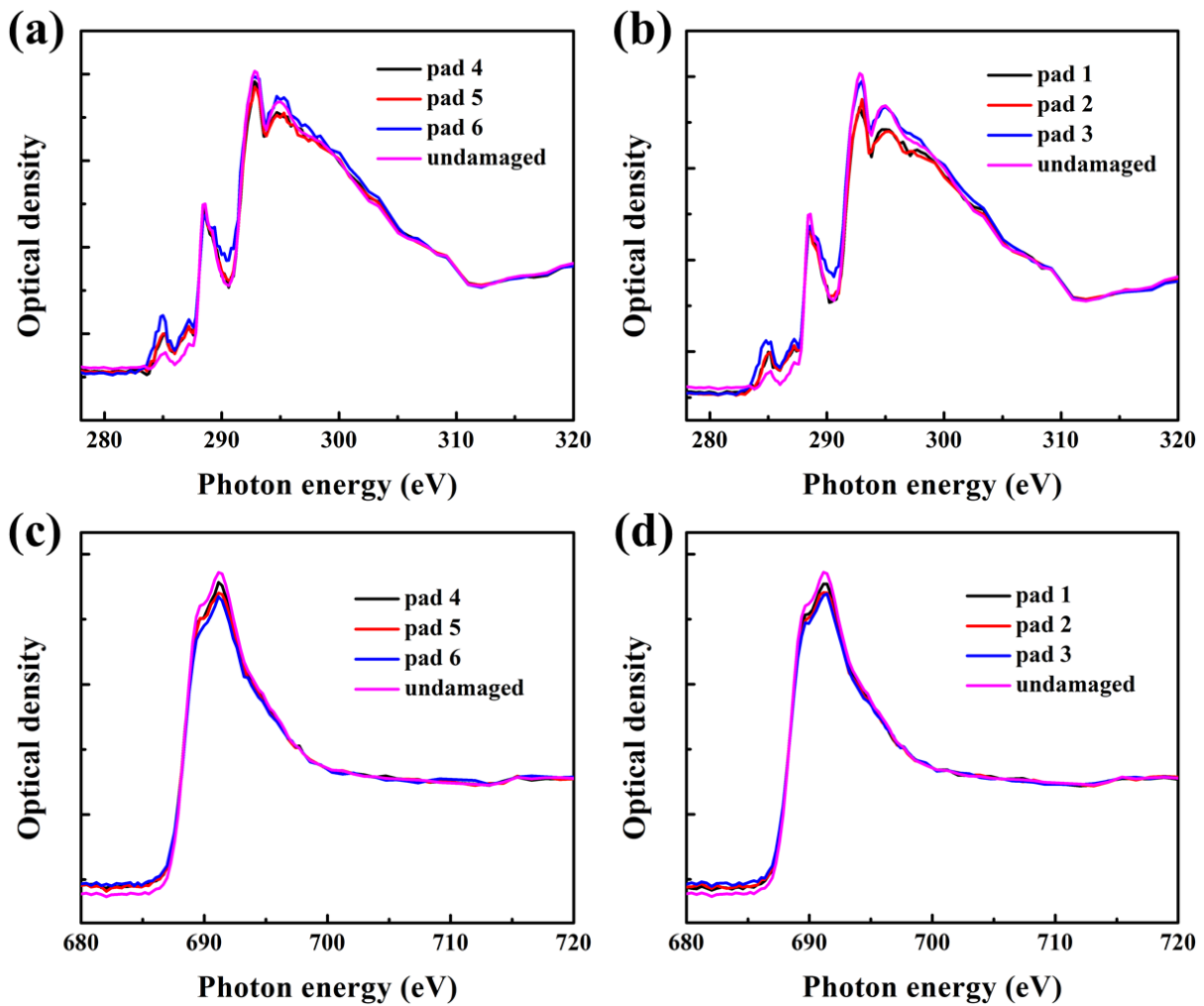
Figure 3 (a) C1s spectrum of the pad 4, 5 and 6 under 0.01 C/cm^2 dose and undamaged region. (b) C1s spectrum of the pad 1, 2 and 3 under 0.1 C/cm^2 dose and undamaged region. (c) F1s spectrum comparison of pad 4, 5 and 6 under 0.01 C/cm^2 dose and undamaged region. (d) F1s spectrum comparison of pad 1, 2 and 3 under 0. 1 C/cm^2 dose and undamaged region.

The C 1s and F 1s of STXM characterization results of the selected irradiated regions are shown in the figure 3. From figure 3 (a) & (b) we can see that, under same irradiation dose, the peak rising of C=C and C=O bonding is more significant with higher dose rate (from 4 to 6, and 1 to 3), indicating that a dose rate dependent property for e-beam damage in PVDF thin film. There is some small dropping at 292 and 296 eV which correspond to the C-F bonds and we did not found very obvious dependency of this dropping with the dose rate effect. The F loss in this

study is less significant than the latest study presented in chapter 5 partly due to the low beam voltage chosen and thick sample, but we still see that the peak height decreases with higher dose rate under same dose condition. Therefore we can expect that under same total irradiation electron dose, the higher beam current can lead to more damage on the polymer. In the real-life SEM imaging practice, the secondary electron yield increases with the beam current and people tend to use large beam current for imaging for acquiring an image with high signal-to-noise ratio (SNR). Based on our results, we suggest that when people deal with beam sensitive materials, they can use the integration of the multiple images taken with low beam current rather than one image taken with high beam current for mitigating the electron beam damage on the sample. As to the effect of electron dose, we did not found conclusive dependency on the dose effect of the beam damage from the results of this experiment because the background irradiation from the navigation process can already pose the damage.

Conclusion

In the study of this chapter, we demonstrate that the STXM is the appropriate tool for characterizing the electron beam damage on thin film polymer sample. We show that even minor electron irradiation during the navigation process can cause the chemical alteration on PVDF thin film. The increasing of C=C and C=O peaks and the loss of fluorine content are the main features for the electron beam damage on the PVDF thin film. From the results of this study, we found that under same dose condition, higher dose rate (beam current) can result in more damage. Due to the background irradiation, low beam energy, and relatively thick sample, we did not find a convincing conclusion about the effect of the electron dose on the beam damage. We can mitigate the beam damage problem on the beam sensitive materials by integrating the multiple images taken under low beam current rather than taking one image with high beam current.

Poster of this chapter is attached in the following page.

Effects of electron dose and dose rate on polyvinylidene fluoride

Weiwei Zhang, Lis Melo, Adam Hitchcock, Nabil Bassim

Introduction

Focused ion beam – scanning electron microscopy (FIB-SEM) is a powerful tool sample preparation, serial sectioning tomography and microfabrication. Though SEM is considered to be a non-destructive characterization method for many materials, the effect of electron irradiation can be significant on soft materials and can alter the chemical structure (damage) the materials. Together with the ion bombardment from FIB, the damage mechanisms in FIB-SEM are complex. Empirically-derived mitigation methods like lower voltage and current or optimized beam rastering, have be proposed previously. In this project, we chose polyvinylidene fluoride (PVDF) to study the beam damage due to its relatively simple chemical structure and potential use in versatile applications. We try to untangle convolved damage mechanisms in FIB-SEM by studying the electron damage mechanisms first. The following research will try to resolve the challenges encountered and extend to the study on poly(methyl methacrylate) (PMMA), the most popular polymer for semiconductor lithography, and Embed 812 epoxy resin for bio-application study.

Experimental procedures

- 100nm (nominal) PVDF ultramicrotomed films
- Electron irradiation experiments were done by FEI Magellan 400 scanning electron microscope (SEM).
- The accelerating voltage for the electron beam is 1kV and each exposing area was set to be $3\mu m \times 2\mu m$ under scanning magnification of 10^5 times.
- An arrayed pattern was created with currents were set to be 50, 200 and 400 pA and electrons dose to be 0.01 and 0.1 C/cm^2 respectfully.
- Damaged area was characterized by Scanning Transmission X-ray Microscopy (STXM) at the Canadian Light Source (CLS) Synchrotron due to its adequate spatial resolution, high spectra resolution and relatively damage-free characterization properties.
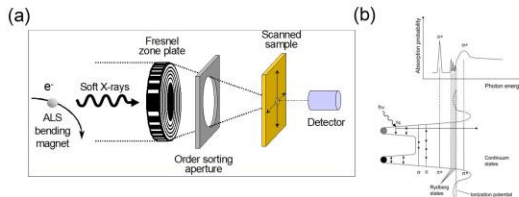

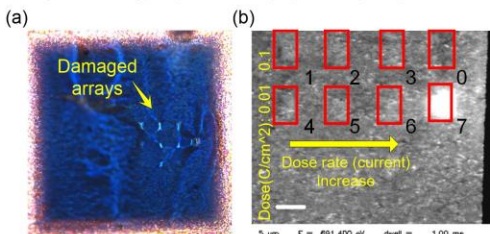Figure 1 Working principle of STXM a) optics and b) absorption mechanism

Figure 2 (a) Optical image of deliberately damaged arrays on PVDF, (b) image of the damaged arrays by STXM

Results and discussion

Effect of minor electron irradiation:

- Visible chemical alteration
- Rise of new peaks at 284.7 and 287.1 eV in C 1s spectrum indicate formation of new chemical bonds related to C=C and C=O π* absorption
- Loss of fluorine

Damage of different irradiation conditions:

- Elemental content changes with irradiation: carbon increases and fluorine decreases
- The heavily damaged area 7 shows extensive modification: significant peaks at 285 and 287.1 eV.
- Hard to directly quantify the degree of chemical change due to the non-uniform thick sample.

Relative quantitative analysis on the spectrum:

- Higher dose rate (current) increases the damage (F/C ration) as the fluorine is knocked off the sample.
- Higher electron dose appear to induce more damage
- Exceptional behavior of area 5 and area 6 can be explained by the effect of the re-deposition and the beam spreading effects
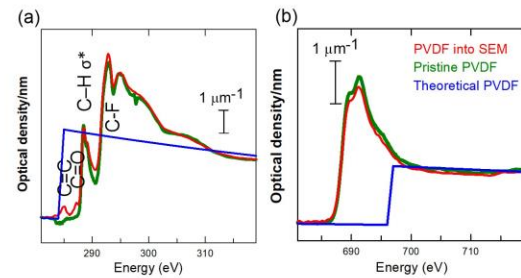

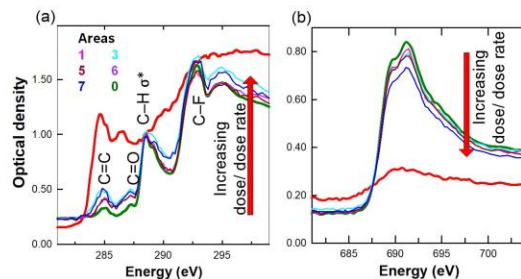Figure 3 (a) C1s spectrum and (b) F1s spectrum of pristine PVDF and PVDF went into SEM chamber

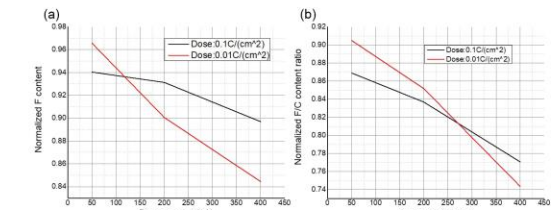Figure 4 (a) C1s spectrum and (b) F1s spectrum of different exposed areas on PVDF film

Figure 5 (a) normalized F content (b) normalized F/C content ratio with beam current under different dose

Conclusion

- Minor electron irradiation can cause chemical alternation on soft materials
- Increase of carbon content and the loss of fluorine are the main features of electron damage.
- Both high electron dose and dose rate (current) can induce noticeable damage.
- Carbon deposition, beam spreading, and slight thickness variations are the main factors which can affect the quantitative analysis in this study.